

Massive star formation in Wolf-Rayet galaxies

II. Optical spectroscopy results^{★,★★}

A. R. López-Sánchez^{1,2} and C. Esteban^{2,3}

¹ CSIRO / Australia Telescope National Facility, PO-BOX 76, Epping, NSW 1710, Australia
e-mail: Angel.Lopez-Sanchez@csiro.au

² Instituto de Astrofísica de Canarias, C/Vía Láctea S/N, 38200 La Laguna, Tenerife, Spain

³ Departamento de Astrofísica de la Universidad de La Laguna, 38071 La Laguna, Tenerife, Spain

Received 12 March 2009 / Accepted 25 September 2009

ABSTRACT

Aims. We have performed a comprehensive multiwavelength analysis of a sample of 20 starburst galaxies that show the presence of a substantial population of very young massive stars, most of them classified as Wolf-Rayet (WR) galaxies. In this paper, the second of the series, we present the results of the analysis of long-slit intermediate-resolution spectroscopy of star-formation bursts for 16 galaxies of our sample.

Methods. We study the spatial localization of the WR stars in each galaxy. We analyze the excitation mechanism and derive the reddening coefficient, physical conditions, and chemical abundances of the ionized gas. We study the kinematics of the ionized gas to check the rotation/turbulence pattern of each system. When possible, tentative estimates of the Keplerian mass of the galaxies are calculated.

Results. Aperture effects and the exact positioning of the slit onto the WR-rich bursts seem to play a fundamental role in their detection. We check that the ages of the last star-forming burst estimated using optical spectra agree with those derived from H α imagery. Our analysis shows that a substantial fraction of the galaxies exhibit evidence of perturbed kinematics. With respect to the results found in individual galaxies, we remark the detection of objects with different metallicity and decoupled kinematics in Haro 15 and Mkn 1199, the detection of tidal streams in IRAS 08208+2816, Tol 9, and perhaps in SBS 1319+579, and the development of a merging process in both SBS 0926+606 A and Tol 1457-262.

Conclusions. All of these results – in combination with those obtained in Paper I – reinforce the hypothesis that interactions with or between dwarf objects is a very important mechanism in triggering massive-star formation in starburst galaxies, especially in dwarf ones. It must be highlighted that only deep and very detailed observations – as presented in this paper – can provide clear evidences that these subtle interaction processes are taking place.

Key words. stars: Wolf-Rayet – galaxies: abundances – galaxies: starburst – galaxies: interactions – galaxies: dwarf – galaxies: kinematics and dynamics

1. Introduction

Wolf-Rayet (WR) stars are the evolved descendants of the most massive, very hot, and very luminous (10^5 to $10^6 L_\odot$) O stars. In the so-called Conti (1976) and Maeder (1990, 1991) scenarios, WR stars are interpreted as central He-burning objects that have lost the main part of their H-rich envelope via strong winds. Hence, their surface chemical composition is dominated by He rather than H, along with elements produced by the nuclear nucleosynthesis. WN and WC stars show the products of the CNO cycle (H-burning) and the triple- α (He-burning) process, respectively. The most massive O stars ($M \geq 25 M_\odot$ for Z_\odot) became WR stars between 2 and 5 Myr after their birth, spending only some few hundreds of thousands of years ($t_{\text{WR}} \leq 5 \times 10^5$ yr)

in this phase (Meynet & Maeder 2005). A review of the physical properties of WR stars was presented by Crowther (2007).

The broad emission features that characterize the spectra of WR stars are often observed in extragalactic H II regions. The so-called Wolf-Rayet galaxies constitute a very inhomogeneous class of star-forming objects: giant H II regions in spiral arms, irregular galaxies, blue compact dwarf galaxies (BCDGs), luminous merging IRAS galaxies, active galactic nuclei (AGNs), Seyfert 2, and low-ionization nuclear emission-line regions (LINERs). All objects have in common ongoing or recent star formation that has produced stars massive enough to evolve onto the WR stage (Shaver et al. 1999). There are two important broad features that are indicative of WR stars in the integrated spectra of an extragalactic H II region:

* Based on observations made with NOT (Nordic Optical Telescope), INT (Isaac Newton Telescope) and WHT (William Herschel Telescope) operated on the island of La Palma jointly by Denmark, Finland, Iceland, Norway and Sweden (NOT) or the Isaac Newton Group (INT, WHT) in the Spanish Observatorio del Roque de Los Muchachos of the Instituto de Astrofísica de Canarias.

** Table 1 and Figs. 1–4, 6–10, 12, 13, 15–30, 32–35 and Appendix are only available in electronic form at <http://www.aanda.org>

1. A blend of He II $\lambda 4686$, C III/C IV $\lambda 4650$, and N III $\lambda 4640$ emission lines that originate in the expanding atmospheres of the most massive stars, the so-called blue WR Bump. This feature is mainly produced by the presence of WN stars. The broad, stellar, He II $\lambda 4686$ is its main feature. Although rarely strong, the narrow, nebular He II $\lambda 4686$ is usually associated with the presence of these massive stars,

- but its origin remains controversial (Garnett et al. 1991; Garnett 2004; Brinchmann et al. 2008).
2. The C III $\lambda 5698$ and C IV $\lambda 5808$ broad emission lines, sometimes called the red or yellow WR Bump. C IV $\lambda 5808$ is the strongest emission line in WC stars but it is barely seen in WN stars. The red WR bump is rarely detected and is always weaker than the blue WR bump (Guseva et al. 2000; Fernandes et al. 2004).

Making use of population synthesis models, it is possible to determine the age of the bursts, the number of O and WR stars, the WN/WC ratio, the initial mass function (IMF), or the mass of the burst. Therefore, the study of WR galaxies helps us to widen our knowledge about both massive star formation and the evolution of starbursts: they allow us to study the early phases of starbursts and are the most direct measure of the upper end of the IMF, a fundamental ingredient in studying unresolved stellar populations (Schaerer et al. 2000; Guseva et al. 2000; Pindao et al. 2002; Fernandes et al. 2004; Buckalew et al. 2005; Zhang et al. 2007), and providing key constraints on stellar evolution models.

On the other hand, the knowledge of the chemical composition of galaxies, in particular of dwarf galaxies, is vital to the understanding of their evolution, star formation history, stellar nucleosynthesis, the importance of gas inflow and outflow, and the enrichment of the intergalactic medium. Indeed, metallicity is a key ingredient in modelling galaxy properties, because it determines the *UV*, optical and *NIR* colours at a given age (i.e., Leitherer et al. 1999), nucleosynthetic yields (e.g., Woosley & Weaver 1995), the dust-to-gas ratio (e.g., Hirashita et al. 2001), the shape of the interstellar extinction curve (e.g., Piovan et al. 2006), or even the WR properties (Crowther 2007).

The most robust means of deriving the metallicity of star-forming and starburst galaxies is by estimating the metal abundances and abundance ratios, e.g., the determination of the gas-phase oxygen and nitrogen abundances and the nitrogen-to-oxygen ratio. The relationships between the current metallicity and other galaxy parameters, such as colours, luminosity, neutral gas content, star formation rate, extinction, or total mass, constrain galaxy evolution models and provide clues about the current stage of a galaxy. For example, it remains debated whether massive star formation causes the instantaneous enrichment of the interstellar medium of a dwarf galaxy, or if the bulk of the newly synthesized heavy elements must cool before becoming part of the ISM that eventually form the next generation of stars. Accurate oxygen abundance measurements of several H II regions within a dwarf galaxy will increase the understanding of its chemical enrichment and mixing of enriched material. The analysis of the kinematics of the ionized gas will also help us to understand the dynamical evolution of galaxies and detect recent interaction features. Furthermore, detailed analysis of starburst galaxies in the nearby Universe are fundamental to interpreting the observations of high- z star-forming galaxies, such as lyman break galaxies (Erb et al. 2003), as well as quantify the importance of interactions in triggering star-formation bursts, which seem to be very common at higher redshifts (i.e., Kauffmann & White 1993; Springer et al. 2005).

We performed a detailed photometric and spectroscopic analysis of a sample of 20 WR galaxies. Our main aim is the study of the formation of massive stars in starburst galaxies, their gas-phase metal abundance, its relationships with other galaxy properties, and the role that the interactions with or between dwarf galaxies and/or low surface brightness objects have in triggering star-formation bursts. In Paper I

(López-Sánchez & Esteban 2008), we outlined the motivation of this work, compiled the list of analyzed WR galaxies (Table 1 of Paper I), and presented the results of optical/*NIR* broad-band and H α photometry. In this second paper, we present the results of our analysis of intermediate-resolution long-slit spectroscopy of 16 objects in our sample of WR galaxies – the results for the other 4 objects have been published separately. In many cases, two or more slit positions were used to analyze the most interesting zones, knots, or morphological structures belonging to each galaxy or even surrounding objects. In particular, these observations have the following aims:

1. Study the number content and spatial location of the WR stars in each galaxy. We examine the spectra for the presence of the He II $\lambda 4686$ emission line and/or the blue-WR bump as well as for the red-WR bump. The characteristics of the WR population can be derived by comparison with theoretical population synthesis models.
2. Determine the physical properties of the ionized gas: excitation mechanism, electron density, high and low ionization electron temperatures, and reddening coefficient.
3. Analyze the ionization structure and the chemistry of the gas (abundances of He, O, N, S, Ne, Ar, Fe, and Cl) associated with different morphological zones in each galaxy, especially in those areas in which WR features are detected. This analysis is especially relevant to the interaction or merging processes because the regions may have different chemical compositions and would also allow us to discern between the *tidal dwarf galaxy* (TDG) or *pre-existing dwarf galaxy* nature of nearby diffuse objects surrounding the main galaxy.
4. Determine the radial velocities of different star-formation bursts, galaxies in the same system, and/or objects in possible interaction. The distance to the main galaxy is also calculated.
5. Study the velocity field by means of analyzing position-velocity diagrams to understand the kinematics of the ionized gas associated with different members in the system to understand their evolution (e.g., rotation, interactions features, evidences of fusion, movements associated with super-winds). The Keplerian mass was estimated in objects showing solid-body rotation.
6. Obtain independent age estimations of the last star-forming burst by comparing with stellar population synthesis models.
7. Study the stellar population underlying the bursts using the analysis of absorption lines (i.e., Ca II H,K, Mg I $\lambda\lambda 5167, 5184$, Na I $\lambda\lambda 5890, 5896$, Ca II triplet).
8. Finally, the spectral energy distribution (SED) is in some cases analyzed to constrain the properties of the underlying stellar population.

This paper mainly presents the analysis of the ionized gas within our WR galaxy sample. In Sect. 2, we describe our observations, some details of the data reduction processes, and describe some useful relations. In Sect. 3, we describe the physical properties (i.e., T_e , n_e , reddening coefficient, excitation mechanism), the chemical abundances and the kinematics of the ionized gas for each galaxy. Finally, the most important results derived from our spectroscopic study, including a comparison with the ages derived from the H α photometry and an estimation of the age of the underlying stellar component using the SED, are summarized in Sect. 4. A detailed analysis of the O and WR populations and the comparison with theoretical models is presented in Paper III (López-Sánchez & Esteban 2010). The global analysis of our optical/*NIR* data will be shown in Paper IV. The final paper of the series (Paper V) will compile the properties derived using data

from other wavelengths (UV, FIR, radio, and X-ray) and complete a global analysis of all available multiwavelength data of our WR galaxy sample. We have produced the most complete and exhaustive data set of this kind of galaxies, so far, involving multiwavelength results and analyzed following the same procedures.

2. Observations and data reduction and analysis

2.1. Spectroscopic observations

We obtained intermediate-resolution long-slit spectroscopy for all our sample of WR galaxies except for NGC 5253, for which high-resolution echelle spectroscopy had been taken (see López-Sánchez et al. 2007 for details). We used three telescopes to carry out these observations: 2.5 m *Isaac Newton Telescope* (INT), 2.56 m *Nordical Optical Telescope* (NOT), and 4.2 m *William Herschel Telescope* (WHT), all located at Roque de los Muchachos Observatory (ORM, La Palma, Spain). The details of these observations are the following:

1. **Observations at the 2.5 m INT.** We used the IDS (*Intermediate Dispersion Spectrograph*) instrument mounted at the Cassegrain focus in December 1999. A EEV CCD 2148×4200 pixel array, with a pixel size of $13.5 \mu\text{m}$, was used, which corresponds to an spatial resolution of $0.40'' \text{ pix}^{-1}$. The slit was $2.8'$ long and $1''$ wide. We used the R400V grating, which has a dispersion of $104.5 \text{ \AA mm}^{-1}$ ($1.40 \text{ \AA pix}^{-1}$) and an effective spectral resolution of 3.5 \AA . The spectra cover the wavelength range from 3200 to 7700 \AA . The absolute flux calibration was achieved by observations of the standard stars Feige 56, Hiltner 600, and Feige 110 (Massey et al. 1988).
2. **Observations at the 4.2 m WHT.** We completed two observation runs in this telescope in December 2000 and December 2002. In both cases, the double-arm ISIS (*Intermediate dispersion Spectrograph and Imaging System*) instrument located at the Cassegrain focus of the telescope was used. The dichroic used to separate the blue and red beams was set to be 5400 \AA . The slit was $3.7'$ long and $1''$ wide. We used different configurations in each observing run:
 - (a) **December 2000:**
 - *Blue arm*: an EEV CCD with a 4096×2048 pixels array and $13 \mu\text{m}$ size was used. The spatial resolution was $0.20'' \text{ pix}^{-1}$. The grating was R600B, giving a dispersion of 33 \AA mm^{-1} ($0.45 \text{ \AA pix}^{-1}$) and an effective spectral resolution of 1.8 \AA . The observed spectral range was 3600 – 5200 \AA .
 - *Red arm*: we used a TEX CCD with a configuration of 1024×1024 pixels of $24 \mu\text{m}$ pixel size, having a spatial resolution of $0.36'' \text{ pix}^{-1}$. The grating R316R, which has a dispersion of 66 \AA mm^{-1} ($0.93 \text{ \AA pix}^{-1}$) and an effective spectral resolution of 2.6 \AA , was used, covering the spectral range 5400 – 6800 \AA .
 - (b) **December 2002:**
 - *Blue arm*: we used the same CCD as previously indicated and the R1200B grating, which gives a dispersion of 17 \AA mm^{-1} ($0.23 \text{ \AA pix}^{-1}$) and an effective spectral resolution of 0.86 \AA . The spectral range was 4450 – 5480 \AA .

- *Red arm*: a Marconi CCD with a 4700×2148 pixel array and $14.5 \mu\text{m}$ pixel size was used. The spatial resolution was $0.20'' \text{ pix}^{-1}$, hence identical to that provided by the blue arm. We used the R316R grating covering the spectral range 5700 – 8600 \AA .

The absolute flux calibration was achieved by observations of the Massey et al. (1988) standard stars G191B2B and Feige 34 (December 2000) and Feige 15, Feige 110, Hiltner 600, and Hz44 (December 2002).

3. **Observations at the 2.56 m NOT.** We completed three observational runs at this telescope, always using the ALFOSC (*Andalucía Faint Object Spectrograph and Camera*) instrument and a Loral/Lesser CCD detector (2048×2048 pixels) with a pixel size of $13.5 \mu\text{m}$ and a spatial resolution of $0.19'' \text{ pixel}^{-1}$. The slit was $6.4'$ long and $1''$ wide. We used several configurations:

- (a) **20 March 2004.** We used grism #7 that has a dispersion of 111 \AA mm^{-1} (1.5 \AA pix^{-1}) and a spectral resolution of 7.5 \AA , covering the spectral range 3200 – 6800 \AA .
- (b) **4 April 2005 and 26–27 April 2006.** We used two different grisms to obtain the blue and the red ranges of the optical spectrum. Grism #14, which has a dispersion of 104 \AA mm^{-1} (1.4 \AA pix^{-1}) and a spectral resolution of 7.0 \AA , was used to cover the spectral range 3300 – 6100 \AA . This grism has a low efficiency for $\lambda \leq 4000 \text{ \AA}$. Spectra in the red range were obtained using the grism #8, which has a dispersion of 96 \AA mm^{-1} (1.3 \AA pix^{-1}), a spectral resolution of 6.5 \AA , and covers the spectral range 5800 – 8300 \AA .

The spectrophotometric standard star Feige 56 (Massey et al. 1988) was used to flux calibrate all the spectra obtained with this telescope.

In all observations, three or four exposures at each slit position were taken to achieve a good signal-to-noise ratio (S/N) ratio and remove cosmic rays. Table 1 compiles all the intermediate-resolution long-slit spectroscopy observations performed for the 16 WR galaxies included in this paper.

2.2. Reduction of the spectra

All the data reduction were completed at the IAC. IRAF¹ software was used to reduce the CCD frames (i.e., perform bias correction, flat-fielding, cosmic-ray rejection, wavelength and flux calibration, and sky subtraction) and extract the one-dimensional spectra. The correction for atmospheric extinction was performed using an average curve for the continuous atmospheric extinction at Roque de los Muchachos Observatory. For each two-dimensional spectra, several apertures were defined along the spatial direction to extract the final one-dimensional spectra of each galaxy or emission knot. The apertures were centered on the brightest point of each aperture and the width was fixed to obtain a good signal-to-noise spectrum. When the optical spectrum was separated into two different wavelength intervals, identical apertures were used for both spectral ranges.

2.3. Analysis of the spectra

IRAF software was also used to analyze the one-dimensional spectra. Line intensities and equivalent widths were measured

¹ IRAF is distributed by NOAO which is operated by AURA Inc., under cooperative agreement with NSF.

by integrating all the flux in the line between two given limits and over a local continuum estimated by eye. In the cases of line blending, a multiple Gaussian profile fitting procedure was applied to obtain the line flux of each individual line. We used the standard assumption, i.e., that $I(\text{H}\beta) = 100$, to compute the line intensity ratios. The identification and adopted laboratory wavelength of the lines, as well as their errors, were obtained following García-Rojas et al. (2004) and Esteban et al. (2004).

2.3.1. Distance to the galaxies

We computed the distance to the galaxies using the brightest emission lines ($\text{H}\alpha$ and $[\text{O III}] \lambda 5007$) in our optical spectra. We assumed a Hubble flow with $H_0 = 75 \text{ km s}^{-1} \text{ Mpc}^{-1}$, $q_0 = 0.5$, and corrected to the Galactic Standard of Rest. The distance we derived for each galaxy is listed in Table 1 in Paper I. All values agree well within the errors with the distances quoted by the NED, except for Tol 9. For this galaxy, we measure a radial velocity of $v_r = 3441 \text{ km s}^{-1}$, while previous observations suggested $v_r = 3190 \text{ km s}^{-1}$ (Lauberts & Valentijn 1989). We consider that our value is more appropriate because the maximum of the H I emission detected in Tol 9 (López-Sánchez et al. 2010) shows the same radial velocity that our optical spectrum provides.

2.3.2. Correction for reddening

The reddening coefficient, $c(\text{H}\beta)$, was derived from the Balmer decrement. However, in extragalactic objects the fluxes of nebular Balmer lines may be affected by absorption produced by the underlying stellar population (mainly B and A stars). We performed an iterative procedure to derive simultaneously the reddening coefficient and the equivalent widths of the absorption in the hydrogen lines, W_{abs} , to correct the observed line intensities for both effects. We assumed that W_{abs} is the same for all the Balmer lines and used the relation given by Mazzarrella & Boronson (1993) to perform the absorption correction,

$$c(\text{H}\beta) = \frac{1}{f(\lambda)} \log \left[\frac{\frac{I(\lambda)}{I(\text{H}\beta)} \times \left(1 + \frac{W_{\text{abs}}}{W_{\text{H}\beta}}\right)}{\frac{F(\lambda)}{F(\text{H}\beta)} \times \left(1 + \frac{W_{\text{abs}}}{W_\lambda}\right)} \right], \quad (1)$$

for each detected hydrogen Balmer line, where $F(\lambda)$ and $I(\lambda)$ are the observed and the theoretical fluxes (unaffected by reddening or absorption), W_{abs} , W_λ , and $W_{\text{H}\beta}$ are the equivalent widths of the underlying stellar absorption, the considered Balmer line and $\text{H}\beta$, respectively, and $f(\lambda)$ is the reddening curve normalized to $\text{H}\beta$ using the Cardelli et al. (1989) law. We always considered the theoretical ratios of these pairs of H I Balmer lines expected for case B recombination given by Storey & Hummer (1995) assuming the electron temperature and density computed independently for each region. Using three different Balmer lines (i.e., $\text{H}\alpha$, $\text{H}\beta$, and $\text{H}\gamma$), a unique value for $c(\text{H}\beta)$ and W_{abs} is computed. However, in the case of the use of four or more Balmer lines, several solutions are derived, so we considered the values that provide the closest match between the corrected and the theoretical Balmer line ratios as representative of the region. An example of this method using 5 Balmer line ratios is shown in Fig. 14 when analyzing UM 420.

Tables A.1, A.3, A.5, A.7, A.9, A.11, A.13, A.15, and A.17 show the dereddened line intensity ratios and their associated errors for all the regions and galaxies, as well as the adopted $f(\lambda)$ of each emission line. In these tables, we also include other

important quantities such as: the size of the extracted aperture, its relative distance to the main region of the galaxy, the observed $\text{H}\beta$ flux (uncorrected for extinction), the adopted values of $c(\text{H}\beta)$ and W_{abs} , and the equivalent widths of $\text{H}\alpha$, $\text{H}\beta$, $\text{H}\gamma$, and $[\text{O III}] \lambda 5007$. Colons indicate the errors of the order or larger than 40%.

2.3.3. Physical conditions of the ionized gas

We studied the physical conditions and chemical abundances of the ionized gas from the 1-D spectra of each galaxy or knot. We used a two-zone approximation to define the temperature structure of the nebulae, assuming the electron temperature, T_e , provided by the $[\text{O III}]$ ion, $T_e(\text{O III})$, as the representative temperature of high ionization potential ions and $T_e(\text{N II})$ or $T_e(\text{O II})$ for the low ionization potential ones. We inferred $T_e(\text{O III})$ from the $[\text{O III}] (\lambda 4959 + \lambda 5507)/\lambda 4363$ ratio, $T_e(\text{N II})$ from $[\text{N II}] (\lambda 6548 + \lambda 6583)/\lambda 5755$, and $T_e(\text{N II})$ from $[\text{O II}] (\lambda 3727 + \lambda 3729)/(\lambda 7319 + \lambda 7330)$. We calculated T_{es} by making use of the five-level program for the analysis of emission-line nebulae included in IRAF NEBULAR task (Shaw & Dufour 1995). We note that we used an updated atomic dataset for O^+ , S^+ , and S^{++} for NEBULAR. The references are indicated in Table 4 of García-Rojas et al. (2004).

When one of the high/low ionization electron temperatures could not be computed, we used the linear relation between $T_e(\text{O III})$ and $T_e(\text{O II})$ provided by Garnett (1992),

$$T_e(\text{O II}) = T_e(\text{N II}) = 0.7 \times T_e(\text{O III}) + 3000, \quad (2)$$

to estimate the unknown electron temperature. When no direct estimate of the electron temperature could be obtained, we considered the $T_e(\text{O III})$ and $T_e(\text{O II})$ pairs that reproduce the total oxygen abundance obtained by applying the Pilyugin (2001a,b) empirical method (see below) and assumed the Garnett (1992) relation, which is the same equation that Pilyugin uses in his empirical calibrations.

The electron density of the ionized gas, n_e , was usually computed via the $[\text{S II}] \lambda\lambda 6716, 6731$ doublet, although sometimes the $[\text{O II}] \lambda\lambda 3726, 3729$ doublet was also used. Regions for which $n_e < 100 \text{ cm}^{-3}$ are below the low-density limit and hence we considered $n_e = 100 \text{ cm}^{-3}$ in those cases.

Veilleux & Osterbrock (1987) proposed diagnostic diagrams plotting two different excitation line ratios, such as $[\text{O III}]/\text{H}\beta$ versus $[\text{S II}]/\text{H}\alpha$, for classifying the excitation mechanism of ionized nebulae. H II regions (or H II or starburst galaxies) lie within a narrow band within these diagrams, but when the gas is ionized by shocks, accretion disks, or cooling flows (in the case of AGNs or LINERs) its position in the diagram is away from the locus of H II regions. We used the analytic relations given by Dopita et al. (2000) and Kewley et al. (2001) between different line ratios to check the nature of the excitation mechanism of the ionized gas within the bursts. Figure 5 shows an example of these diagrams applied to the regions analyzed in the galaxy Mkn 1199.

2.3.4. Chemical abundances

Once the electron density and temperature are estimated, the ionic abundances can be derived for each region. All the ionic abundances except He^+ and Fe^{++} were calculated using the IRAF NEBULAR task (Shaw & Dufour 1995) from the intensity of collisionally excited lines. We assumed a two-zone scheme for deriving the ionic abundances, adopting $T_e(\text{O III})$ for the high ionization potential ions O^{++} , Ne^{++} , S^{++} , Ar^{++} , Ar^{3+} , and Cl^{++} ;

and $T_e(\text{N II})$ or $T_e(\text{O II})$ for the low ionization potential ions O^+ , N^+ , S^+ , and Fe^{++} .

The He^+/H^+ ratio was computed from the He I lines intensities using the predicted line emissivities calculated by [Smith, Shara & Moffat \(1996\)](#) for the $T_e(\text{O III})$ and n_e assumed for each region. We also corrected for collisional contribution following the calculations by [Benjamin, Skillman & Smits \(2002\)](#). Self-absorption effects were not considered.

The Fe^{++} abundances were derived using the $[\text{Fe III}] \lambda 4658$ emission line. We used a 34 level model-atom that includes the collision strengths of [Zhang \(1996\)](#) and the transition probabilities of [Quinet \(1996\)](#).

We computed the total abundances of O, N, S, Ne, Ar, and Fe. We always adopted $\text{O/H} = \text{O}^+/\text{H}^+ + \text{O}^{++}/\text{H}^+$ to determine the total oxygen abundance. We detected the nebular $\text{He II } \lambda 4686$ line in several objects, but the relative contribution of He^{++} to the total amount of helium is negligible, implying that O^{3+} has also a very low abundance in the nebula, thus we did not consider its contribution to the total O/H ratio. To derive the nitrogen abundance we assumed the standard ionization correction factor (ICF) by [Peimbert & Costero \(1969\)](#): $\text{N/O} = \text{N}^+/\text{O}^+$, which is a reasonably good approximation considering the excitation degree of the observed galaxies. We used the ICF provided by [Peimbert & Costero \(1969\)](#) to derive the total neon abundance. We computed the total sulphur abundance when both S^+/H^+ and S^{++}/H^+ ratios were available using the ICF given by the photoionization models by [Stasińska \(1978\)](#). The total argon abundance was calculated by considering the ICFs proposed by Izotov et al. (1994). The total iron abundances were obtained from the $\text{Fe}^{++}/\text{H}^+$ ratio and the ICF given by [Rodríguez & Rubin \(2005\)](#).

As we said before, when direct estimations of the electron temperature were not available, we resorted to empirical calibrations. [Pilyugin \(2001a,b\)](#) performed a detailed analysis of observational data combined with photoionization models to obtain the oxygen abundance from the relative intensities of strong optical lines. [Pilyugin \(2001a\)](#) gives the empirical calibration between the R_{23} and P (an indicator of the hardness of the ionizing radiation) parameters and the oxygen abundance in moderately high-metallicity H II regions, $12+\log(\text{O/H}) \geq 8.3$. [Pilyugin \(2001b\)](#) provides the empirical calibration for the low-metallicity branch. Unless indicated, we always used the Pilyugin empirical calibrations to derive the electron temperatures and the chemical abundances of the ionized gas in regions where no direct determination of T_e was possible. Sometimes, we estimated the total oxygen abundance by using of the Denicoló et al. (2002) or [Pettini & Pagel \(2004\)](#) empirical calibrations, which involve the $[\text{N II}] \lambda 6583/\text{H}\alpha$ ratio.

2.3.5. Estimation of the Keplerian and dynamical masses

The bidimensional spectra were used to perform a position-velocity diagram by analyzing the brightest emission line profiles ($\text{H}\alpha$ and/or $[\text{O III}] \lambda 5007$) for all the objects. Although the main objective is the analysis of the kinematics of the ionized gas, in some cases we estimated the Keplerian mass (M_{Kep}) of the galaxies by assuming that the kinematics are representative of circular rotation. We usually considered half of the maximum velocity difference, Δv , half of the spatial separation corresponding to these maxima, r , and applied the equation

$$M_{\text{Kep}} [M_\odot] \sim 233 \times r [\text{pc}] \left(\frac{\Delta v [\text{km s}^{-1}]}{\sin i} \right)^2, \quad (3)$$

assuming circular orbits and Keplerian dynamics ([López-Sánchez et al. 2004b](#)). We note that the result of this equation is *not* the total dynamical mass of the galaxy but only the total mass contained within a circle of radius r . The inclination angle, i , is defined as that found between the plane of the sky and the plane of the galaxy (hence, $i = 90^\circ$ in an edge-on galaxy and $i = 0^\circ$ in a face-on galaxy). We usually estimated this angle by assuming that the elliptical shape of the galaxy is just a consequence of its orientation.

When 21-cm H I data were available in the literature, we computed both the neutral gas mass, M_{HI} , and the dynamical mass, M_{dyn} , using the typical relations (i.e., Dahlem et al. 2005). We estimated the rotation velocity of the neutral gas considering $\Delta v = \frac{W_{\text{HI}}}{2 \sin i}$ and adopted the maximum radius observed in our deep optical images. Therefore, as the extension of the neutral gas is usually larger than the extension of the stellar component, our estimations of M_{dyn} may be underestimated. The gas depletion timescale defined by [Skillman et al. \(2003\)](#) was computed using M_{HI} and the total star-formation rate (SFR) derived for each galaxy in Paper I. When FIR data were available, we estimated the mass of the warm dust, M_{dust} , using the equations given by [Huchtmeier et al. \(1995\)](#). Although M_{Kep} , M_{dyn} , and M_{dust} should be considered only tentative values, their comparison provides important clues about the galaxy type, its dynamics, and the fate of the neutral gas.

3. Results

3.1. NGC 1741 – HCG 31 AC

The spectroscopic analysis of NGC 1741 (member AC in the galaxy group HCG 31) was presented in detail in [López-Sánchez et al. \(2004a\)](#). Our spectra show a clearly evident broad blue WR bump and the $\text{He II } \lambda 4686$ emission line in this object (Fig. 36). A careful re-analysis of the data reveals an evident and broad red WR bump in the same region (Fig. 37), in agreement with previous observations of the same object ([Guseva et al. 2000](#)). The spectrum of members F1 and F2 (TDGs candidates) show the $\text{He II } \lambda 4686$ emission line; member F2 also seems to exhibit a blue WR bump. The analysis of the kinematics of the group infers that almost simultaneous interaction processes involving several objects are taking place.

3.2. Mkn 1087

Mkn 1087 is a luminous blue compact galaxy and the main galaxy within a group in interaction. Although some authors did observe WR features in this galaxy ([Kunth & Joubert 1985; Vaceli et al. 1997](#)), others did not ([Vacca & Conti 1992](#)), and it was therefore classified as *suspected* WR galaxy by [Schaerer et al. \(1999\)](#). Our analysis of Mkn 1087 was presented in [López-Sánchez et al. \(2004b\)](#); we did not detect any WR feature (Fig. 36) within any important star-forming region inside or surrounding Mkn 1087.

3.3. Haro 15

Haro 15 is a blue compact galaxy that has been well studied at all frequencies, including optical spectroscopy ([Hunter & Gallagher 1985; Mazzarella et al. 1991; Kong et al. 2002; Shi et al. 2005](#)). [Schaerer et al. \(1999\)](#) listed Haro 15 as a WR galaxy because of the detection of the $\text{He II } \lambda 4686$ emission line by [Kovo & Contini \(1999\)](#). Our analysis confirms the presence of WR stars

(nebular and broad He II $\lambda 4686$) in the bright star-forming region A (Fig. 36).

Our long-slit spectroscopy covers the four main regions observed in Haro 15 (see Fig. 3 of Paper I): the center (C), the bright region A at the ESE, the relatively bright H II region D at the WNW (both observed with the slit with PA 117°) and the knot B (at the NE, observed with the slit with PA 41°). Figure 1 shows the spectra of the three brightest objects, whereas Table A.1 compiles the emission line ratios and other properties of the spectra of each region.

The spectrum of the center of Haro 15 shows both nebular emission lines and stellar absorption; this absorption is observed mainly in the H I Balmer lines. However, the spectrum of region A is entirely dominated by nebular emission lines, where we detect [O III] $\lambda 4363$ and He II $\lambda 4686$. Because of the faintness of B and D, few emission lines are observed in these regions.

3.3.1. Physical conditions of the ionized gas

A direct estimation of $T_e(\text{O III})$ was computed in knot A because of the detection of [O III] $\lambda 4363$. We used empirical calibrations to estimate the electron temperatures for the remaining regions; the results are shown in Table A.2. The spectrum of the central region of Haro 15 has a marginal detection of [O III] $\lambda 4363$. Using this value, we derived $T_e[\text{O III}] \sim 9700$ K, which is very similar to that obtained using empirical calibrations. The [S II] $\lambda 6717$ emission line is blended with a skyline in all spectra, and hence we cannot compute n_e . We assumed a value of 100 cm^{-3} for all regions. Comparing the line ratios with diagnostic diagrams, we found that all knots can be classified as typical H II regions.

3.3.2. Chemical abundances

Table A.2 compiles all the chemical abundances computed for each region of Haro 15. We found a significant difference between the oxygen abundance at the center of Haro 15, $12+\log(\text{O/H}) = 8.37$, and that found in the ESE region (knot A), $12+\log(\text{O/H}) = 8.10$, which is larger than the uncertainties. This suggests that, although their projected distance is very small (5.5 kpc), both objects seem to have experienced different types of chemical evolution. The values for the oxygen abundance in knots B and D – at greater distances from the center of the galaxy – are slightly lower than that at the center of Haro 15, perhaps indicating a possible radial abundance gradient in the disk of the galaxy. However, this may not be applicable to knot B because it could be an independent object because of its decoupled kinematics (see below). Regions A, B, and D show a much lower N/O ratio than the center of the galaxy.

Figure 2 shows the relative flux of the [O II] $\lambda 3727$ and [O III] $\lambda 5007$ emission lines along the slit. As we can see, knot A has a much higher ionization degree than to the other regions. This should be a consequence of the extreme youth of the star formation in this zone and its lower metallicity, both characteristics illustrating the unique nature of this object.

3.3.3. Kinematics of the ionized gas

Figure 3 shows the position-velocity diagrams for the two slit positions observed in Haro 15. We analyzed both the H α and the [O III] $\lambda 5007$ profiles, extracting 4 pixel bins (1.6 arcsec) and considering the velocity of the center of the galaxy as a reference. Analysis of both emission lines provide almost identical

results. The diagram of PA 41° shows an apparent rotation pattern, although some divergences are found at the SW. Knot B is clearly decoupled from the rotation of the disk, suggesting that it is an external object. The interaction between knot B and Haro 15 could be responsible for the distortion observed at the SW of the diagram of PA 41° , because the object and this zone of the galaxy disk have similar radial velocities. Another possibility is that knot B is a TDG but, in this case, the material that formed B should come from the external parts of the disk of Haro 15 because its chemical abundances are more similar to those of knot D than to those of the central region.

The diagram with PA 117° shows a clear sinusoidal pattern with differences of around 40 km s^{-1} . This feature is common in processes involving galaxy interactions or merging. Although it is not completely clear, region A seems to be kinematically coupled with the rotation of the galaxy. This finding and the different chemical composition indicate that knot A is probably an external object experiencing a merging process with Haro 15.

Assuming that the position-velocity diagram of PA 41° from -5 to 15 arcsec from the center is a consequence of circular rotation, we can estimate the Keplerian mass of Haro 15. Considering a radial velocity of $\sim 80 \text{ km s}^{-1}$ within a distance of ~ 13 arcsec (5.46 kpc) and assuming $i = 55^\circ$ from our optical images (Gordon & Gottesman (1981) found $i = 57^\circ$), we derive $M_{\text{Kep}} = 1.21 \times 10^{10} M_\odot$ and $M_{\text{Kep}}/L_B = 0.35$. The neutral and dynamical masses of Haro 15 are $M_{\text{HI}} = 5.54 \times 10^9 M_\odot$ and $M_{\text{dyn}} = 3.65 \times 10^{10} M_\odot$ (Gordon & Gottesman 1981). Thus, our Keplerian mass is $\sim 33\%$ of the total mass. The M_{HI}/L_\odot and the M_{dust}/L_\odot ratios (0.16 and 0.6×10^{-4} , respectively) suggest that Haro 15 is a Sb or Sc spiral (Bettoni et al. 2003). The gas depletion timescale is 2.3 Gyr, showing that the system still possesses a huge amount of material that is available to form new stars.

3.4. Mkn 1199

Izotov & Thuan (1998) observed Mkn 1199 but they did not detect the [O III] $\lambda 4363$ emission line. However, they reported the blue and red WR bumps and nebular He II $\lambda 4686$ emission. Hence, Mkn 1199 was classified as a WR galaxy (Schaerer et al. 1999). Guseva et al. (2000) revisited its WR properties finding evidences of WNL, WNE, and WCE stellar populations.

We obtained intermediate resolution long-slit spectroscopy of Mkn 1199 using two different slit positions (see Fig. 5 of Paper I). We analyzed five different regions: the center of Mkn 1199 (C), the companion dwarf object (NE), and knots A, B, and D, all extracted with a slit with PA 36° apart from region A, for which the slit with PA 53° was used. The spectra of the two brightest regions (C and NE) are shown in Fig. 4, while the emission line intensities and other important properties of the spectra are compiled in Table A.3. The spectrum of the center of Mkn 1199 exhibits stellar absorption in both the H I Balmer and the He I lines, as previously noted by Izotov & Thuan (1998). The blue WR bump and a probable He II $\lambda 4686$ are detected in C (Fig. 36). Our spectrum also shows a tentative detection of the red WR bump in this region (Fig. 37). The spectrum of the dwarf companion galaxy at the NE has a lower S/N than that obtained for Mkn 1199, but all relevant emission lines are clearly identified. Stellar absorption is also found in this region but is weaker than that observed in C. The spectra of the remaining knots show only the brightest emission lines.

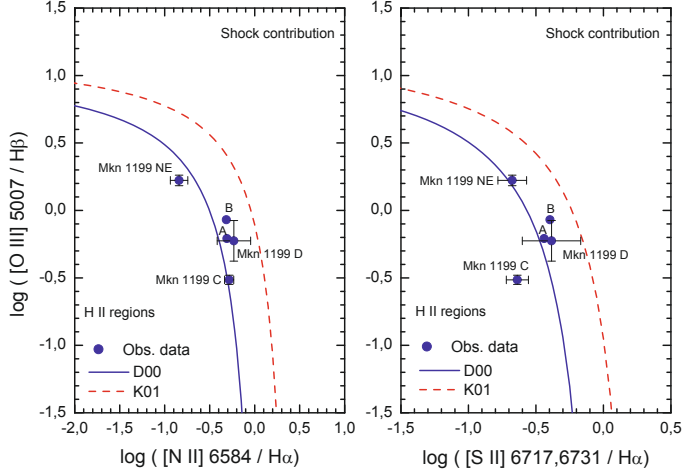


Fig. 5. Comparison of some line intensity ratios in several regions of Mkn 1199 with the diagnostic diagrams proposed by Dopita et al. (2000) and Kewley et al. (2001).

3.4.1. Physical conditions of the ionized gas

The [O III] $\lambda 4363$ line was not detected in any region, hence we computed the electron temperatures and chemical abundances using empirical calibrations (see Table A.4). The electron temperatures found in C are rather low. In this zone, we detected [N II] $\lambda 5755$, which infers a $T_e[\text{N II}] \sim 6740$ K, a value very similar to that estimated using the empirical method. We also detected the [O II] $\lambda\lambda 7319, 7330$ doublet in the spectrum of C, measuring $T_e(\text{O II}) \sim 6910$ K. Hence, we consider that the electron temperature values obtained using the empirical calibrations are completely reliable for this object, assuming that $T_e(\text{low}) = 6800$ K. The high ionization electron temperature was computed using Garnett's relation, $T_e(\text{high}) = 5400$ K. Except for region C, the electron densities derived from the [S II] $\lambda\lambda 6717, 6730$ doublet were in the low-density limit, $n_e \sim 100 \text{ cm}^{-3}$. The values for the reddening coefficient are relatively high for C and B, which is indicative of a significant amount of dust in those regions. The comparison of some line intensity ratios with the diagnostic diagrams proposed by Dopita et al. (2000) and Kewley et al. (2001) indicates that all regions can be classified as H II regions (see Fig. 5).

3.4.2. Chemical abundances

Table A.4 compiles all the chemical abundances computed for the knots analyzed in Mkn 1199. The oxygen abundance found at the center of the system is very high, $12+\log(\text{O/H}) = 8.75 \pm 0.12$ (indeed, it is the highest metallicity region found in this work). However, the oxygen abundance of the dwarf companion galaxy at the NE is almost 0.3 dex lower, $12+\log(\text{O/H}) = 8.46$. The N/O ratios derived for them are also very different. Hence, this result re-enforces the hypothesis that they are independent galaxies in the first stages of minor merging.

Although the line intensities measured by Izotov & Thuan (1998) in Mkn 1199 are quite similar to those compiled in Table A.3, the oxygen abundance derived by these authors is $12+\log(\text{O/H}) = 8.19 \pm 0.18$, which is extremely low compared with our values. However, Guseva et al. (2000) using the same data as Izotov & Thuan (1998) and the empirical calibration based on the [N II] $\lambda 6583/\text{H}\alpha$ ratio proposed by van Zee et al. (1998) obtain $12+\log(\text{O/H}) = 9.13$. We consider that

$12+\log(\text{O/H}) = 8.75$ is a more appropriate value for the oxygen abundance at the center of Mkn 1199, which also agrees with our tentative estimates of electron temperatures.

Knots A, B, and D exhibit oxygen abundances that are slightly lower than C, i.e., between 8.6 and 8.7, but not as low as that reported for the companion galaxy. Interestingly, A, B, and D exhibit a N/O ratio very similar to that observed at the center of the galaxy, but much higher than in the dwarf companion. This confirms the different chemical evolution of the disk of Mkn 1199 and its companion galaxy. We consider that the knots A, B, and D are giant H II regions located in the spiral arms of Mkn 1199 and that this galaxy could have a slight radial metallicity gradient along its disk. Finally, we propose that the triggering mechanism of the intense star-formation activity found in both, Mkn 1199 and its dwarf companion, is a likely consequence of the strong interaction that they are experiencing.

3.4.3. Kinematics of the ionized gas

Figure 6 shows the position-velocity diagrams for the two slit positions in Mkn 1199. They were obtained by extracting 3 pixel bins (1.2 arcsec) across the H α profile and considering the center of Mkn 1199 as a reference. The diagram with PA 36°, which crosses the center of Mkn 1199 and the companion galaxy, may be explained by the rotation of the disk of Mkn 1199, because it shows a velocity gradient between 30 km s^{-1} at SW (knot D) and -30 km s^{-1} at NE (around knot B). However, a sinusoidal pattern is also seen in the brightest region of Mkn 1199, within the central 10''. This feature may be a consequence of an entity kinematically decoupled from the disk, such as a bar or the bulge of the galaxy, that seems to be counter-rotating, although it may also be an interaction feature. On the other hand, although there are only four points in the diagram in that zone, the dwarf galaxy at the NE seems to be rotating. This object, which has an elliptical shape in the optical images, may be observed edge-on, which would explain both its kinematics and morphology. The diagram with PA 53° also seems to show a velocity gradient from the SW to the NE (where knot A is located) but this gradient is broken within the central 10''. The maximum velocity difference is around 80 km s^{-1} .

It is difficult to estimate the Keplerian mass of Mkn 1199 because it is observed almost face-on. However, considering that the velocity difference between its center and the external regions within a radius of 10'' (2.6 kpc) is around 30 km s^{-1} and adopting an inclination angle of 15°, we derive $M_{\text{kep}} \sim 8.2 \times 10^9 M_\odot$. For the companion dwarf object, assuming that it is edge-on ($i = 90^\circ$) and considering a velocity difference of 10 km s^{-1} within a radius of 2.5'' (1.3 kpc), we compute $M_{\text{Kep}} \sim 2.9 \times 10^7 M_\odot$.

Using the H I data given by Davoust & Contini (2004), we compute $M_{\text{HI}} = 1.22 \times 10^9 M_\odot$ and $\Delta v_{\text{HI}} = 85 \text{ km s}^{-1}$. Assuming a radius of 25'' (6.55 kpc) and $i = 15^\circ$, the dynamical mass of Mkn 1199 is $M_{\text{dyn}} = 1.7 \times 10^{11} M_\odot$. The warm dust mass using the FIR data is $M_{\text{dust}} = 3.1 \times 10^6 M_\odot$. Following the classification provided by Bettoni et al. (2003), the $M_{\text{HI}}/L_\odot = 0.042$ and $M_{\text{dust}}/L_\odot = 1.1 \times 10^{-4}$ ratios are not compatible: while the first agrees with the typical values for S0 galaxies, the second ratio indicates that Mkn 1199 should be an Sc or Sd, more similar to the true morphological classification of Sb. Furthermore, fewer than 1% of the total mass of the system is neutral hydrogen and the gas depletion timescale is very short (0.4 Gyr). All of this implies that a substantial fraction of the neutral H I gas has been expelled to the intergalactic medium, perhaps as a

consequence of the interaction with the dwarf companion galaxy. An H I map obtained using a radio-interferometer would be needed to confirm this hypothesis.

3.5. Mkn 5

[Conti \(1991\)](#) included Mkn 5 in his catalogue of WR galaxies because of the detection of the nebular He II $\lambda 4686$ line by [French \(1980\)](#). However, [Izotov & Thuan \(1998\)](#) only observed the blue WR bump, without any trace of nebular He II emission ([Schaerer et al. 1999](#)). [Guseva et al. \(2000\)](#) detected N III $\lambda 4640$, implying the presence of WNL stars within the starburst.

We used three slit positions when acquiring the spectroscopic data of Mkn 5 (see Fig. 7 of Paper I), two of them using the 2.5 m INT and an additional position using 4.2 m WHT. All have a very similar PA, 0° (INT-1), 354° (WHT), and 349° (INT-2). All slit positions cover region A but only two transverse knot B. We analyzed the three spectra extracted for region A independently to check the quality of the results. Figure 7 shows the spectra of the region A obtained with the slit positions with PA 349° and PA 354° . For region B, we only analyzed the spectrum extracted using the slit position with PA 0° (INT-1) because of its higher S/N. Table A.5 compiles all the emission line fluxes and other characteristics of each spectrum. Our spectra confirm the presence of a nebular He II $\lambda 4686$ line on top of a broad emission line in region A (Fig. 36). Although the WHT spectrum is of high S/N and spectral resolution, we do not detect the red WR bump in this region (Fig. 37). All spectra are dominated by nebular emission but some absorption in the H I Balmer lines is also detected; these are more evident in knot B.

3.5.1. Physical conditions of the ionized gas

The three spectra obtained for region A show the [O III] $\lambda 4363$ emission line and hence we computed the electron temperature using the direct method. As can be seen in Table A.6, all T_e values agree within the errors, the average value being $T_e[\text{O III}] \sim 12\,500$ K. The low ionization temperature was derived using Garnett's relation, $T_e[\text{O II}] \sim 11\,700$ K. The spectrum INT-2 shows a tentative detection of [O II] $\lambda\lambda 7318, 7330$, which infers that $T_e[\text{O II}] \sim 11\,950$ K, in agreement with the electron temperature derived using Garnett's relation. We used [Pilyugin \(2001b\)](#) empirical calibration to derive T_e in knot B, but this determination is very uncertain and perhaps overestimated because of the faintness of the spectrum. The electron densities are always below the low-density limit (100 cm^{-3}), except for knot B (although it also has a large error).

The values of the reddening coefficient derived for region A differ somewhat in the different spectra. Perhaps, this apparent inconsistency is a consequence of an irregular distribution of dust within Mkn 5, as suggested by our analysis of the optical/NIR colours (see Sect. 3.5.1 of Paper I). For knot B, we assumed that $W_{\text{abs}} = 1.5 \text{ \AA}$ and the value of $c(\text{H}\beta)$ computed via the $\text{H}\alpha/\text{H}\beta$ ratio. The diagnostic diagrams for knots A and B agree with the loci of typical H II regions.

3.5.2. Chemical abundances

The WHT spectrum does not cover the [O II] $\lambda\lambda 3726, 29$ doublet, hence we used [O II] $\lambda\lambda 7318, 7330$ to compute the O⁺/H⁺ ratio. As we can see in Table A.5, the agreement between the emission line ratios for all the three spectra extracted for region A is very good. Table A.6 compiles the chemical abundances

obtained for Mkn 5; for region A, all values are quite similar and in agreement with previous results found in the literature. Averaging all data and minimizing errors, we derive for A the following chemical abundance ratios: $12+\log(\text{O/H}) = 8.07 \pm 0.04$, $\log(\text{N/O}) = -1.38 \pm 0.07$, $\log(\text{S/O}) = -1.62 \pm 0.11$, $\log(\text{Ne/O}) = -0.80 \pm 0.13$, and $\log(\text{Ar/O}) = -2.31 \pm 0.12$. These values are very similar to the results provided by [Izotov & Thuan \(1999\)](#). On the other hand, the oxygen abundance estimated for knot B, $12+\log(\text{O/H}) = 7.89 \pm 0.17$, is lower than that derived for the main star-forming region but consistent within the errors. If real, this difference may imply that the two regions have experienced different chemical evolution.

3.5.3. Kinematics of the ionized gas

Figure 8 shows the position-velocity diagrams obtained for the three slit positions observed in Mkn 5. For the 4.2 m WHT spectrum, we analyzed the $\text{H}\alpha$ profile considering 6 pixel bins (1.2 arcsec), while we used the [O III] $\lambda 5007$ profile (which is brighter than the $\text{H}\alpha$ profile) to extract 4 pixel bins (1.6 arcsec) from the 2.5 m INT spectra. As we can see, the agreement between the three diagrams is very good. The diagram containing the most reliable results is that provided by the analysis of the 4.2 m WHT spectrum, which has a velocity range of around $\sim 50 \text{ km s}^{-1}$. The velocity of knot B with respect to that found in region A is $\sim 40 \text{ km s}^{-1}$. Although the uncertainties are important, we detect a slight reverse in the velocity of region A, with an amplitude of $\sim 20 \text{ km s}^{-1}$ (which is more evident in the 4.2 m WHT diagram), that seems to show a sinusoidal pattern in that area.

Assuming that the global velocity gradient is mainly a consequence of the rotation of the galaxy, we may estimate the Keplerian mass of the system. We found $M_{\text{Kep}} \sim 2.1 \times 10^9 M_\odot$ assuming that $i = 90^\circ$, $\Delta v \sim 27 \text{ km s}^{-1}$, and $r \sim 21''$ (1.22 kpc). Using H I data ([Paturel et al. 2003](#)), we derive $M_{\text{HI}} = (7.2 \pm 0.9) \times 10^7 M_\odot$ and $M_{\text{dyn}} \sim 3.6 \times 10^9 M_\odot$. Although both M_{Kep} and M_{dyn} are similar, we note that they are low limits because we assume that Mkn 5 is an edge-on galaxy. The mass-to-luminosity ratios are $M_{\text{Kep}}/L_\odot = 7.98$, $M_{\text{Dyn}}/L_\odot = 13.7$, and $M_{\text{HI}}/L_\odot = 0.27$. The H I mass is quite low for a dwarf or irregular galaxy, being only 2% of the total mass. The gas depletion timescale is ~ 1.8 Gyr, which is high for a starburst galaxy. All of this suggests that something has happened to the atomic gas of Mkn 5 that or it has been consumed while forming stars at a high rate up until a few hundred Myr ago (today the rate is lower) or it has been expelled into the intergalactic medium. [Thuan & Martin \(1981\)](#) found indications of H I gas at slightly different radial velocities ($\sim 300 \text{ km s}^{-1}$) using single-dish data. An interferometric H I map will be crucial to understanding the fate of the neutral gas in this blue compact dwarf galaxy.

3.6. IRAS 08208+2816

The first spectroscopic data of IRAS 08208+2816 were obtained by [Huang et al. \(1999\)](#), who reported the detection of both a nebular and broad He II $\lambda 4686$ emission line. They also detected the red WR bump, C IV $\lambda 5808$, suggesting the presence of both WNL and WCE populations in the starburst. [Schaerer et al. \(1999\)](#) included IRAS 08208+2816 in their latest catalogue of WR galaxies.

We used three slit positions with the IDS spectrograph at the 2.5 m INT to cover all bright knots within the galaxy (see Fig. 9 of Paper I). The slit position with PA 345° crosses a bright

star and the center of IRAS 0828+2816, the slit position with PA 355° covers the center and knots #8, #10, and #1 (which is very affected by the light of the bright star) and the slit position with PA 10° crosses #3, #4 (very weak), and #5, although it may also be contaminated by some emission from the center and knot #8. Table A.7 compiles the properties of the five regions that we analyze spectroscopically. The center of the galaxy, C, corresponds to the brightest region extracted using the slit position with PA 345° . This spectrum and that obtained for knot #8 are shown in Fig. 9. Although all spectra are dominated by nebular emission and do not detect any absorption in the H I Balmer lines, we detect a slight decrease in the continuum level within the blue range of the spectra of the faintest objects. This can be explained by both an important extinction in these objects and by an underlying evolved stellar population. The broad He II $\lambda 4686$ line is weakly detected in the central region of the galaxy but the nebular He II $\lambda 4686$ line is not identified in this spectrum (Fig. 36). A faint, red WR bump at around ~ 5800 Å also seems to be observed in this region (Fig. 37). Spectra with higher S/N and spectral resolution are needed to obtain a robust value of the WR bump fluxes.

3.6.1. Physical conditions of the ionized gas

We detect the weak, auroral [O III] $\lambda 4363$ emission line at the center of the galaxy, its flux value was used to estimate the electron temperature following the direct method. For the remaining objects, we used empirical calibrations to compute T_e , all results being compiled in Table A.8. In knots #3 and #5, [O III] $\lambda 4363$ is barely detected but they were not considered in the analysis because of their large errors. All electron temperatures derived using empirical methods, including those found in knot #8, are systematically lower than those computed in the central region following the direct method. All objects can be classified as H II regions following the typical diagnostic diagrams.

The reddening coefficient was computed using all available H I Balmer lines in each spectrum. We obtained very different values: while the central region and knots in the northern tail have a low reddening coefficient, $c(H\beta) \sim 0.12$, knots located in the southern tail show a higher value, $c(H\beta) \sim 0.43$. This seems to indicate an inhomogeneous distribution of the dust within the galaxy, the southern regions being dustier than the remainder of the system. Huang et al. (1999) also derived low extinction values in the center of IRAS 08208+2816, which they explained by considering the presence of a galactic wind in the galaxy, but we do not detect these structures in our deep H α images (see Fig. 10 of Paper I).

3.6.2. Chemical abundances

Table A.8 compiles all chemical abundances computed for the different knots analyzed in IRAS 08208+2816. The oxygen abundance of the central region, derived using the direct method, is $12+\log(O/H) = 8.33 \pm 0.08$, and its nitrogen-to-oxygen ratio is $\log(N/O) = -0.89 \pm 0.11$. This value is higher than the N/O ratio expected for a galaxy with an oxygen abundance of $12+\log(O/H) \sim 8.3$, which should be $\log(N/O) \sim -1.2$. If this effect is real, it may be due to nitrogen pollution by the winds of the WR stars, as we confirm occurs in the case of NGC 5253 (López-Sánchez et al. 2007).

For the rest of the objects, the oxygen abundances were calculated using the empirical calibrations of Pilyugin (2001a,b). Although all estimates are slightly higher than the value found in

the central region, we notice a significant difference in the case of knot #8, which has $12+\log(O/H) \sim 8.64$ (i.e., almost the solar value). Knots #3 and #5 show a tentative detection of [O III] $\lambda 4363$ in their spectra, for which we derive an oxygen abundance ~ 0.12 – 0.15 dex lower than that estimated using empirical calibrations (see Table A.8). This trend is also found in the central region, for which we derive $12+\log(O/H) \sim 8.41$ following the empirical calibrations. Hence, the values obtained using the Pilyugin method may be somewhat overestimated for this galaxy.

In any case, the chemical abundance differences seem to be real in knot #8, first because its oxygen abundance is ~ 0.3 dex higher than that found in the central region, and second because its N/O ratio is also the highest, $\log(N/O) \sim -0.84$, and consistent with the value expected for a galaxy of almost solar metallicity. This result indicates that knot #8 could be an object that has chemically evolved more than the others. Because of this and its position within the system, knot #8 may even correspond to the center of an independent galaxy that is in the process of merging with another galaxy, whose nucleus coincides with knot C of IRAS 08208+2816.

3.6.3. Kinematics of the ionized gas

Figure 10 shows the position-velocity diagrams obtained for the three slit positions. The [O III] $\lambda 5007$ profile was analyzed by considering 3 pixel bins ($1.2''$) and taking the center of IRAS 08208+2816 as a reference. As can clearly be seen in the bidimensional spectra, this object possesses very interesting kinematics, including a probable tidal stream in the northern tail. In these areas, we observe a difference in velocity larger than 300 km s^{-1} within $12''$ (11 kpc) in the slit position crossing the northern region of the system (PA = 355°). This velocity difference of 300 km s^{-1} is the same as that reported by Perryman et al. (1982) between these objects. As we commented before, the spectra crossing the southern tail is affected by contamination from a nearby bright star, but the slit position with PA = 10° is free of this contamination allowing a kinematical analysis to be performed of the southern zone. Again, we found an important velocity gradient towards negative values, which cannot be explained by a rotating disk. Furthermore, this diagram shows an evident sinusoidal pattern with an amplitude larger than 50 km s^{-1} at the center of the galaxy. This is additional evidence that we are observing the process of merging. In general, the agreement between the three diagrams is very good, for example, the velocity found for knot #1 using the slit position with PA 355° is $\sim -250 \text{ km s}^{-1}$, which corresponds well to the velocity observed at the end of the southern tail (knot #3, with $\sim -200 \text{ km s}^{-1}$) using the slit position with PA 10° .

Although the kinematics of the system is not supported by rotation, we estimated a tentative value of the Keplerian mass of the system. Assuming $i = 90^\circ$, $\Delta v \sim 30 \text{ km s}^{-1}$ (using the diagram with PA 345° , that seems to be less affected by the tidal tails) and a radius of $\sim 20''$ (18.4 kpc), we derive $M_{\text{Kep}} \sim 3.9 \times 10^9 M_\odot$. The mass-to-luminosity ratio is quite low, $M_{\text{Kep}}/L_B \sim 0.08$, hence we probably underestimate the mass of the system. No H I data are available for this galaxy in the literature, but it would be interesting to compare the kinematics of the neutral gas with that found here for the ionized gas. The warm dust mass is high, $M_{\text{dust}} = 8.84 \times 10^6 M_\odot$, giving $M_{\text{dust}}/L_B \sim 1.73 \times 10^{-4}$.

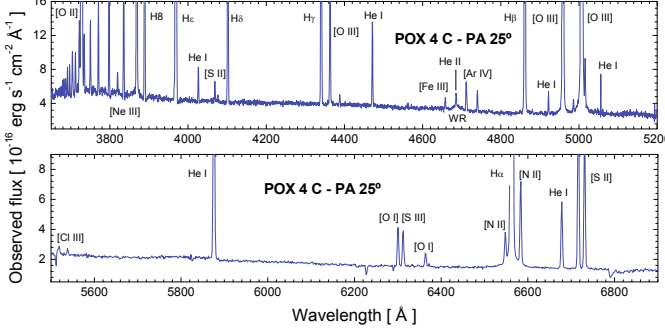


Fig. 11. ISIS 4.2 m WHT spectrum for the center of POX 4. Fluxes are not corrected for reddening. The most important emission lines have been labeled. See Fig. 11 in Paper I for the identification of the regions.

3.7. IRAS 08339+6517

Our complete analysis of the physical properties, chemical abundances, and kinematics of the ionized gas in IRAS 08339+6517 and its companion dwarf galaxy was presented in López-Sánchez et al. (2006). We reported weak spectral features that could be attributed to the blue WR bump at the center of the galaxy. The kinematics of the ionized gas showed an interaction pattern that indicates that the H I tidal tail detected by Cannon et al. (2004) in the direction of the dwarf companion galaxy formed mainly from material stripped from the main galaxy. A star-forming region in the outskirts of the galactic disk may be a TDG candidate.

3.8. POX 4

The first indications of WR features in POX 4 were noted by Kunth & Joubert (1985) and Campbell et al. (1986)², because both detected the broad He II $\lambda 4686$ emission line. Therefore, Conti (1991) included POX 4 in his catalogue of WR galaxies. Masegosa et al. (1991) also suggested the presence of WR stars in one or two regions of the galaxy³. Vacca & Conti (1992) confirmed the presence of a high number of O and WN stars in the brightest region of POX 4 and detected the He II $\lambda 4686$ emission line in other knot (Schaerer et al. 1999). We detect the nebular He II $\lambda 4686$ line with a high S/N in the brightest knot of POX 4. Both the broad He II $\lambda 4686$ and C IV $\lambda 5808$ lines are also clearly identified in this region (Figs. 36 and 37).

We used ISIS at the 4.2 m WHT to obtain the spectroscopic data of POX 4 and its dwarf companion galaxy (knot #18 following Fig. 11 in Paper I). The position angle of the slit was set to be 25°. The spectrum of the center of POX 4 (Fig. 11) is dominated by intense emission lines and does not show any evidence of stellar absorption in the H I or He I lines. As previously noted by Méndez & Esteban (1997), broad low-intensity asymmetric wings are detected in the profiles of the brightest emission lines (H α and [O III]). The clear detection of the nebular He II $\lambda 4686$ emission on top of a broad feature indicates the presence of WR stars at the center of the galaxy. However, we do not see the red WR bump despite the high S/N and spectral resolution of our spectrum.

² These authors named POX 4 C 1148-2020 in their Table 1 and Tol 1148-202 in their Table 2. Following NED, the appropriate name of this galaxy is IRAS 11485-2018 = POX 4.

³ These authors named POX 4 as C 1148-2020 in their Table 1 and as Tol 1148-202 in their Table 2. Following the NED, the appropriate name of this galaxy is IRAS 11485-2018 = POX 4.

The spectrum of the dwarf companion object is of rather low S/N and only the brightest emission lines are detected. However, it shows clear absorption features in the H I Balmer lines, indicating the presence of evolved stellar populations underlying the starburst. Table A.9 compiles all emission lines detected at the center of POX 4 and in the dwarf companion object, as well as other important properties of their spectra.

3.8.1. Physical conditions of the ionized gas

The physical conditions and chemical abundances of the ionized gas in POX 4 are compiled in Table A.10. The electron temperature calculated for the center of POX 4 using [O III] $\lambda 4363$ is $T_e(\text{O III}) = 14\,000 \pm 600$ K, suggesting that it is a low metallicity object. Although [N II] $\lambda 5755$ is barely detected, we preferred to use Garnett's relation to determine $T_e(\text{O II})$ from $T_e(\text{O III})$. The electron density was computed using the [S II] $\lambda 6717/\lambda 6731$ ratio, yielding $n_e \sim 250$ cm $^{-3}$. We note that the estimation of n_e using the [Ar IV] $\lambda 4711/\lambda 4740$ ratio provides a very similar value, ~ 270 cm $^{-3}$, although it has a higher uncertainty. For the dwarf companion object, we used empirical calibrations to estimate T_e . Its electron density is the low-density limit. The comparison of the observed [O III] $\lambda 5007/\text{H}\beta$ and [N II] $\lambda 6584/\text{H}\alpha$ ratios with the diagnostic diagrams allowed us to classify all regions as starbursts.

The reddening coefficient at the center of POX 4 was determined using 7 H I Balmer lines, obtaining $c(\text{H}\beta) = 0.08 \pm 0.01$. A similar low value of the reddening was found for the companion object.

3.8.2. Chemical abundances

The oxygen abundance derived for the center of POX 4, $12+\log(\text{O/H})=8.03 \pm 0.04$, agrees with that found in the literature (e.g., Kobulnicky & Skillmann 1996 reported 7.97 ± 0.02). The nebular He II $\lambda 4686$ emission line is clearly detected and, therefore, some O $^{+3}$ contribution is expected in the nebular gas, although this contribution is found to be marginal, $\sim 0.01\text{--}0.02$ dex. The oxygen abundance derived for the companion object using empirical calibrations, $12+\log(\text{O/H}) = 8.03 \pm 0.14$, is the same as that found for POX 4. The values of the N/O ratio are also similar, $\log(\text{N/O}) = -1.54 \pm 0.06$ and -1.60 . Despite the uncertainties, the resemblance of the chemical abundances may suggest that the dwarf companion is not an independent object, as Méndez & Esteban (1999) concluded, but a TDG candidate.

3.8.3. Kinematics of the ionized gas

The position-velocity diagram obtained for the slit-position taken for POX 4 is shown in Fig. 12. Because of its higher intensity, we used the [O III] $\lambda 5007$ profile instead of the H α profile, extracting 4 pixel bins (0.8 arcsec) and taking as reference the velocity found in the center of the galaxy (knot #9, see Fig. 11 in Paper I). The diagram shows a clear irregular pattern without any rotation evidence, indicating that the movement of the ionized gas of the system is rather chaotic but of small amplitude. Méndez & Esteban (1999) proposed that the companion (#18) has travelled through POX 4, producing the peculiar ring-morphology of the galaxy and the strong star-forming bursts observed throughout all the system. The diffuse dwarf companion, which possesses a radial velocity similar to that observed at the center of POX 4, also shows peculiar kinematics, which appears

to be coupled with the movement of the ionized gas in the main galaxy. Our optical data do not suggest that the dwarf companion object is a TDG because we do not detect any other dwarf galaxy that may have interacted with POX 4 and stripped some material from it. Méndez & Esteban (1999) indicated a velocity difference of $\sim 130 \text{ km s}^{-1}$ between POX 4 and the companion galaxy, but this is not confirmed in our deeper spectroscopic data.

Taking into account the complex kinematic structure shown in Fig. 12, it is clear that we cannot obtain a confident estimate of the Keplerian mass of POX 4. However, assuming a ratio of $M_{\text{Kep}}/L_B \sim 0.1$, it would be of the order of $M_{\text{Kep}} \sim 5 \times 10^8 M_\odot$. The *H I Parkes All-Sky Survey* (HIPASS; Barnes et al. 2001) shows a tentative detection of *H I* emission. Our group performed 21-cm observations of POX 4 using the interferometer *Australia Telescope Compact Array* (ATCA). Although a detailed description and analysis of these observations will be presented elsewhere (López-Sánchez et al. 2010), the very preliminary analysis suggests that the system possesses a lot of neutral gas. The *H I* kinematics are perturbed at the position of the dwarf companion object but it has the same radial velocity we found using optical spectroscopy. An independent *H I* cloud, which has the same radial velocity as POX 4, is found at $\sim 4.5'$ ($\sim 60 \text{ kpc}$) to the south. It shows a clear alignment with both the bright center of POX 4 and the dwarf companion object, suggesting a very probable interaction in the past. A detailed analysis of the *H I* observations will confirm or discard the TDG nature of the dwarf companion object surrounding POX 4.

3.9. UM 420

Izotov & Thuan (1998) reported the detection of the broad *He II* $\lambda 4686$ emission line in UM 420, which was therefore included in the latest catalogue of WR galaxies (Schaerer et al. 1999). The reanalysis of their spectra performed by Guseva et al. (2001) detects *C IV* $\lambda 4658$ and *C IV* $\lambda 5808$ emission lines, indicative of WCE stars in the starburst.

Figure 13 shows the spectra of UM 420 and UGC 1809 for our slit position (see Fig. 13 of Paper I). Note the huge difference between the spectra: while the spectrum of UM 420 is dominated by emission lines, the spectrum of UGC 1809 only shows stellar absorption lines such as *Ca II H, K, G-band*, and *Mg I* $\lambda 5167$. Hence, we classify this object as a S0 spiral galaxy with redshift of $z = 0.0243$. The radial velocity of UGC 1809 is $v_r = 7290 \text{ km s}^{-1}$, in excellent agreement with the value given by the NED ($v_r = 7306 \text{ km s}^{-1}$) but much lower than the radial velocity of UM 420 ($v_r = 17507 \text{ km s}^{-1}$). This confirms that both galaxies are not physically related.

The spectra of UM 420 do not show absorption features. We observe, although with large error, the nebular *He II* $\lambda 4686$ line on top of a very faint broad feature (Fig. 36). We do not detect the red WR bump despite the high S/N and the clear detection of the weak *[N II]* $\lambda 5755$ auroral line (Fig. 37). The list of the emission lines observed in UM 420 is compiled in Table A.9.

3.9.1. Physical conditions of the ionized gas

Using the *[O III]* $\lambda 4363$ line intensity, we compute $T_e(\text{O III}) = 13200 \pm 600 \text{ K}$ in UM 420. Although it has a large error, the detection of the auroral *[N II]* $\lambda 5755$ emission line indicates $T_e(\text{N II}) \sim 11800 \text{ K}$, that is similar to the low ionization temperature given by Garnett's relation between $T_e(\text{O III})$ and $T_e(\text{O II})$. The electron density computed using the *[S II]* $\lambda\lambda 6716, 6731$ doublet is in the low-density limit,

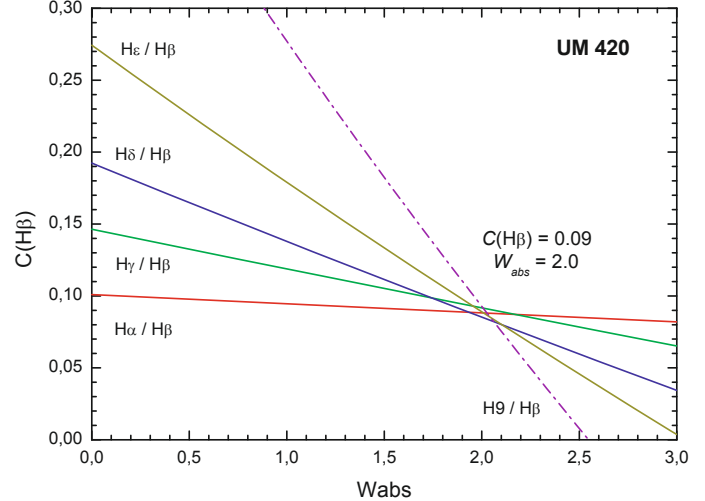


Fig. 14. Interactive estimation of $c(\text{H}\beta)$ and W_{abs} using the six brightest *H I* Balmer lines detected in the spectrum of UM 420. Note the excellent agreement in the behaviour of all lines.

but that estimated using the *[O II]* $\lambda\lambda 3726, 3729$ lines gives $n_e \sim 140 \text{ cm}^{-3}$. The reddening coefficient and the underlying stellar absorption in the *H I* Balmer lines were computed using 5 ratios between the *H I* Balmer lines, which provide consistent results of mean values $c(\text{H}\beta) = 0.09 \pm 0.01$ and $W_{\text{abs}} = 2.0 \pm 0.1$ (see Fig. 14). The comparison of the observed line flux ratios with the diagnostic diagrams clearly identify UM 420 as a starburst galaxy.

3.9.2. Chemical abundances

Table A.10 lists all the chemical abundances computed for UM 420. The derived oxygen abundance is $12 + \log(\text{O/H}) = 7.95 \pm 0.05$, in excellent agreement with the value given by Izotov & Thuan (1998). Our estimation does not consider the small contribution of O^{+3} (which should exist because of the detection of *He II*) but this is smaller than 0.01 dex. The N/O ratio, $\log(\text{N/O}) = -1.11 \pm 0.08$, is also similar to the value reported by these authors. It is interesting to notice that its N/O ratio is higher than that expected for its oxygen abundance, which should be around 0.4 dex lower. This was previously reported by Pustilnik et al. (2004), who suggested that the overabundance of nitrogen may be produced by pollution by the large amount of WR stars present in the violent starburst triggered by galaxy merging. The value of the neon abundance in UM 420, $\log(\text{Ne/O}) = -0.71 \pm 0.13$, is also similar to that given by Izotov & Thuan (1998). We derive $\log(\text{S/O}) = -1.66 \pm 0.15$, which is typical of BCDGs with the same oxygen abundance (Izotov & Thuan 1999).

3.9.3. Kinematics of the ionized gas

Figure 15 shows the position-velocity diagram obtained for the slit position with PA 90° observed in UM 420. Both the *Hα* and *Hβ* profiles were analyzed by extracting 3-pixel bins ($1.08''$) for *Hα* and 4-pixel bins ($0.8''$) for *Hβ*. The diagram is identical in both cases. Although the number of points is small, we notice a velocity gradient of around 30 km s^{-1} from the eastern region to the center of the galaxy, but this tendency is reversed in the western areas of UM 420. Indeed, in this region a negative change

of velocity of $\sim 70 \text{ km s}^{-1}$ is found only within $4''$ ($\sim 4.6 \text{ kpc}$). The diagram does not allow us to determine the Keplerian mass. There are no available H I data of the galaxy to derive its neutral or dynamical masses.

3.10. SBS 0926+606

SBS 0926+606 is a pair of compact nearby objects (see Fig. 15 of Paper I). SBS 0926+606 A was studied spectroscopically by Izotov and collaborators to determine the primordial helium abundance (Izotov et al. 1997; Izotov & Thuan 1998) and the chemical abundances of heavy elements in BCDGs (Izotov & Thuan 1999). Subsequent spectroscopic studies were performed by Pérez-Montero & Díaz (2003) and Kniazev et al. (2004). Izotov et al. (1997) indicated the presence of broad low-intensity components in both the H α and [O III] $\lambda\lambda 5007$ profiles. These authors also detected the blue WR bump, which is strongly contaminated by nebular emission, observing both the nebular and broad He II $\lambda 4686$ emission lines. Hence, Schaefer et al. (1999) included SBS 0926+606 A in their catalogue of WR galaxies. Guseva et al. (2000) revisited the properties of the massive stars in this galaxy. Until now, no spectroscopic data has existed for SBS 0926+606 B.

Figure 16 shows our ISIS 4.2 m WHT spectrum obtained for SBS 0926+606 A using a long-slit at a PA of 14° . It crosses mainly the subregion A2 defined using our optical data (see Fig. 15 in Paper I). As we see in Fig. 16, the spectrum is of high spectral resolution, but only covers between 4200 and 5000 Å in the blue range and between 5600 and 7400 Å in the red range. Therefore, we did not observe the [O II] $\lambda\lambda 3726, 3729$ doublet and the bright [O III] $\lambda 5007$ emission line. The spectrum obtained for the galaxy B is very noisy and only shows the brightest emission lines.

Table A.9 compiles all the emission line fluxes and the main properties of each spectrum. The nebular He II $\lambda 4686$ emission line is clearly detected in SBS 0926+606 A (Fig. 36). Both the blue and red (Fig. 37) WR bumps are not observed, despite the high S/N and spectral resolution. There is not significant stellar absorption in the spectrum of SBS 0926+606 A, but we detect broad low-intensity asymmetric wings in the H α profile.

3.10.1. Physical conditions of the ionized gas

Table A.10 compiles the values found for the electron temperatures of the ionized gas within these objects. For member A, $T_e(\text{O II})$ was computed using the direct method because of the detection of [O III] $\lambda 4363$ line. Temperature $T_e(\text{O II})$ was estimated using Garnett's relation. The spectrum obtained for member B does not allow us to calculate R_{23} , so we used the N_2 ratio and the empirical calibrations given by Denicoló et al. (2002) and Pettini & Pagel (2004) to estimate T_e . Since empirical calibrations involving the N_2 ratio appear to overestimate the true abundance (we discuss this in Paper III), the electron temperatures derived for galaxy B may be underestimated.

The electron density, computed using the [S II] $\lambda\lambda 6717, 31$ doublet, was always at the low-density limit. For both galaxies, the reddening coefficient was derived using the 3 brightest H I Balmer lines. The comparison of the emission-line ratios with the diagnostic diagrams indicates that both galaxies are starbursts.

3.10.2. Chemical abundances

Table A.10 compiles the chemical abundances derived in this galaxy pair. Because of the lack of the [O II] $\lambda\lambda 3726, 29$ data, we used [O II] $\lambda\lambda 7318, 7330$ fluxes to compute the O $^+$ /H $^+$ ratio. The chemical abundances derived for SBS 0926+606 A are $12+\log(\text{O/H}) = 7.94 \pm 0.08$, $\log(\text{N/O}) = -1.45 \pm 0.09$, $\log(\text{S/O}) = -1.60 \pm 0.13$, and $\log(\text{Ar/O}) = -2.34 \pm 0.13$, which are very similar to those obtained by Izotov & Thuan (1999). The oxygen abundance found for member B using the N_2 empirical calibrations is $12+\log(\text{O/H}) \sim 8.15$, somewhat higher than that found for galaxy A, but as we commented above, it may be overestimated. The N/O ratios of both galaxies are rather similar, so both object should have experienced similar chemical evolution. They are indeed dwarf galaxies of very similar M_B (see Paper I).

3.10.3. Kinematics of the ionized gas

Figure 17 shows the position-velocity diagram derived from the slit position observed in SBS 0926+606. We extracted 4-pixel bins (0.8 arcsec) across the H α profile. SBS 0926+606 A shows a clear sinusoidal pattern with an amplitude of around 50 km s^{-1} , suggesting that the double nucleus we found in this galaxy (see Figs. 15 and 16 of Paper I) may be a consequence of an advanced merging process between two objects. The northern outskirts of SBS 0926+606 A seems to be partially decoupled from the sinusoidal pattern (there is a difference of around 60 km s^{-1} with respect to the central velocity). On the other hand, SBS 0926+606 B also exhibits a perturbed kinematics, because both its northern and southern edges have similar radial velocities. The elongated shape of SBS 0926+606 B, the two tails towards the west detected in our deep images, and the disturbed kinematics imply that the interaction that this galaxy is experiencing –most probably with SBS 0926+606 A– is very close to the plane perpendicular to the line of sight, and therefore SBS 0926+606 B is observed almost edge-on. In any case, we do not detect any morphological features, such as the debris of a tidal tail or a diffuse non-stellar object, between both galaxies thus their possible interaction is nowadays not very strong.

Finally, the complexity of the position-velocity diagram shown in Fig. 17 does not allow us to determine the Keplerian mass of the galaxy. Using the H I data given by Pustilnik et al. (2002), we derive $M_{\text{HI}} = (9.6 \pm 3.6) \times 10^8 M_\odot$ and $M_{\text{HI}} = (8.1 \pm 3.6) \times 10^8 M_\odot$ for A and B, respectively, which are indicative of mass-to-luminosity ratios of $M_{\text{HI}}/L_B = 0.75$ and 0.59. The gas depletion timescales are 1.7 Gyr for A and 5.5 Gyr for B. Assuming half of the amplitude of the H I velocity ($\sim 60 \text{ km s}^{-1}$ for both galaxies) and effective radii of $\sim 10''$ (2.71 kpc) for A and $\sim 20''$ (5.42 kpc) for B, we estimate dynamical masses of $M_{\text{Dyn}} \sim 2.3 \times 10^9 M_\odot$ and $M_{\text{Dyn}} \sim 4.5 \times 10^9 M_\odot$ for A and B, respectively. The mass-to-luminosity ratios, $M_{\text{Dyn}}/L_B = 1.8$ and 3.3 for A and B, respectively, which are values typical of BCDGs (Huchtmeier, Krishna & Petrosian 2005). However, the $M_{\text{HI}}/M_{\text{Dyn}}$ ratios are high, 0.42 and 0.18 for A and B, respectively, indicating that a considerable amount of the total mass of the galaxies ($\sim 42\%$ for A) is neutral hydrogen. All these values indicate that the system still contains a huge amount of unenriched material from which new stars may be born. Indeed, the H I profile obtained by Thuan et al. (1999b) exhibits two peaks, which coincide with the optical velocities of the galaxies, embedded in an common H I envelope. This strongly suggests that a lot of neutral gas should be found between both galaxies. An HI map obtained using a radio-interferometer would be

necessary to study the distribution and kinematics of the neutral gas, providing key clues about the evolution of the system.

3.11. SBS 0948+532

SBS 0948+532 was studied by Izotov and collaborators (Izotov et al. 1994; Thuan et al. 1995; Izotov & Thuan 1998; Guseva et al. 2000; Izotov & Thuan 2004). Schaefer et al. (1999) included this BCDG in their catalogue of WR galaxies because of the detection of both the broad and nebular He II $\lambda 4686$ emission lines in the spectra presented by Izotov et al. (1994). The reanalysis performed by Guseva et al. (2000) indicated the presence of WNL stars and a rather noisy red WR bump.

Figure 18 shows our ISIS 4.2 m WHT spectrum of SBS 0948+532 using a slit position with PA 114°. The emission-line fluxes of the detected lines and other properties of the spectrum are compiled in Table A.11. No stellar absorption was observed in this spectrum. We detect the broad and nebular He II $\lambda 4686$ emission lines (Fig. 36), but the red WR bump (Fig. 37) is not observed despite the high S/N of our spectrum.

3.11.1. Physical conditions of the ionized gas

The intensity of [O III] $\lambda 4363$ was used to compute the high ionization electron temperature; the low ionization electron temperature was estimated using Garnett's relation. These values are compiled in Table A.12. The electron density, $n_e \sim 250 \text{ cm}^{-3}$, was derived using the [O II] $\lambda\lambda 3726, 3729$ doublet. Despite its high error, the value of the n_e estimated from the [Ar IV] $\lambda 4711/\lambda 4740$ ratio is similar, $\sim 260 \text{ cm}^{-3}$. The reddening coefficient was estimated to high precision because of the detection of so many H I Balmer lines. The equivalent width of the H I Balmer stellar absorption lines, W_{abs} , is very small, suggesting that the underlying population of evolved stars is not important. The comparison of the observed emission-line fluxes with the diagnostic diagrams confirms that the gas is ionized by the strong UV emission of the massive stars.

3.11.2. Chemical abundances

Table A.12 lists all the chemical abundances computed for SBS 0948+532. The value of the oxygen abundance is $12+\log(\text{O/H}) = 8.03 \pm 0.05$. The N/O ratio is $\log(\text{N/O}) = -1.42 \pm 0.08$, the typical value found for objects with the metallicity of this galaxy. In general, all our chemical abundances for this BCDG agree with those estimated by Izotov & Thuan (1999) within the errors.

3.11.3. Kinematics of the ionized gas

Figure 19 shows the position-velocity diagram obtained for the slit position observed in SBS 0948+532 (see Fig. 17 in Paper I). We analyzed the [O III] $\lambda 5007$ profile by extracting 4-pixel bins (0.8 arcsec). Although the diagram only shows 11 points because of the compact size of this BCDG, a kind of rotation pattern with a velocity difference of around 100 km s^{-1} is observed. This feature seems to be disturbed in the SE areas, which is precisely the region where the faint arc is seen in our optical images (see Fig. 17 of Paper I). Assuming that the kinematics of the galaxy is produced by rotation, $i = 90^\circ$ and $\Delta v \sim 50 \text{ km s}^{-1}$ within a radius of $\sim 4''$ (3.63 kpc), we derive a Keplerian mass of $M_{\text{Kep}} \sim 2.1 \times 10^9 M_\odot$ and $M_{\text{Kep}}/L_\odot \sim 0.57$. Unfortunately, no additional H I or FIR data are available for this galaxy.

3.12. SBS 1054+365

The first spectroscopic study of SBS 1054+365 was performed by Izotov et al. (1997), who detected the broad He II $\lambda 4686$ emission line. Guseva et al. (2000), Izotov & Thuan (2004), and Buckalew et al. (2005) confirmed the WR feature of this low-metallicity galaxy. This BCDG is included in the latest WR galaxy catalogue (Schaefer et al. 1999).

We used the IDS spectrograph mounted on the 2.5 m INT to acquire the spectroscopy of SBS 1054+365. The slit position was set to be 55° , crossing the main body of the galaxy along its major axis (see Fig. 19 of Paper I). Hence, we observed knot *b*, the central bright region C and part of the star-forming semi-ring located at the west (knot *a*). We only analyzed the physical conditions and the chemical abundances of the ionized gas in region C and knot *b*. Figure 20 shows the spectrum of the center of SBS 1054+365. Table A.11 compiles the dereddened line intensity ratios and other properties of the spectrum. As we can see, the spectrum is dominated by nebular emission without any evidence of stellar absorption. We detect the nebular He II $\lambda 4686$ emission line onto a broad stellar He II line (Fig. 36). The red WR bump is not detected (Fig. 37) perhaps because of the S/N of our spectrum being too low.

3.12.1. Physical conditions of the ionized gas

The electron temperatures in the central region were computed using the [O III] $\lambda 4363$ emission line intensity and Garnett's relation between $T_e(\text{O III})$ and $T_e(\text{O II})$. For knot *b*, we used the Pilyugin (2001a,b) empirical calibrations. The electron density was estimated using the [S II] $\lambda\lambda 6716, 6731$ doublet, which in the central region is at the low-density limit. The values of the reddening coefficient are rather low. The comparison of the [O III] $\lambda 5007/\text{H}\beta$, [N II] $\lambda 6584/\text{H}\alpha$, and [S II] $\lambda\lambda 6716, 6730/\text{H}\alpha$ ratios with the diagnostic diagrams allows us to classify all knots as typical H II regions.

3.12.2. Chemical abundances

Table A.12 compiles the chemical abundances derived for SBS 1054+364. The oxygen abundance computed for the center of the galaxy is $12+\log(\text{O/H}) = 8.00 \pm 0.07$, and its N/O ratio is $\log(\text{N/O}) = -1.41 \pm 0.09$, in excellent agreement with the values obtained by Izotov & Thuan (1999). Despite its large error, the oxygen abundance and N/O ratio estimated for knot *b* are very similar to those found at the center of the galaxy.

3.12.3. Kinematics of the ionized gas

We used our bidimensional spectrum for the slit position with PA 55° to compile the position-velocity diagram shown in Fig. 21. We extracted 3-pixel bins (1.2 arcsec) across the H α profile and considered as reference the brightest region of the galaxy. The diagram does not exhibit a clear rotation pattern but several changes in the velocity distribution. The central region seems to show a velocity gradient of around 40 km s^{-1} between $-5''$ and $10''$. This feature was previously noted by Zasov et al. (2000) but their lower spatial resolution did not allow them to identify the small amplitude velocity variations (see their Fig. 3b). These authors suggested that this velocity gradient is a consequence of the rotation of the galaxy. Our diagram also indicates that the SW region, the partial ring where knot *a* is located, does not follow the kinematics of the center of the galaxy, showing a velocity variation of 40 km s^{-1} in $7.2''$. On the other hand, the kinematics

of the region *b*, which has an inverted velocity gradient of around 40 km s^{-1} , also seem to be decoupled from the movement of the gas in the central region, which shows a positive velocity gradient of $\sim 25 \text{ km s}^{-1}$ in its NE area. However, the amplitude of all the velocity variations seen in Fig. 21 are rather small and cover spatial extensions of the order of several hundred pc. Therefore, it is possible that they could be produced by local movements of the bulk of the ionized gas in turn caused by the combined action of winds or supernova explosions.

In any case, assuming that rotation is present at the center of the galaxy and considering that $\Delta v \sim 20 \text{ km s}^{-1}$ within a radius of $\sim 16''$ (624 pc) and an inclination of $i \sim 60^\circ$ (determined using its optical sizes), we computed a tentative value for the Keplerian mass of $M_{\text{Kep}} \sim 7.8 \times 10^7 M_\odot$, which indicates that $M_{\text{Kep}}/L_\odot \sim 1.19$. Using the H I data provided by Zasov et al. (2000), we estimated that $M_{\text{HI}} = (6.08 \pm 0.59) \times 10^7 M_\odot$ and $M_{\text{HI}}/L_B \sim 0.93$. Assuming a radius of $35''$ (1.37 kpc) and the same inclination angle, we estimated a dynamical mass of $M_{\text{dyn}} \sim 1.5 \times 10^9 M_\odot$. The neutral gas to total mass ratio, $M_{\text{HI}}/M_{\text{dyn}} \sim 0.04$, is typical of BCDGs but its total mass-to-light ratio, $M_{\text{dyn}}/L_B \sim 22.9$, is quite high (Salzer et al. 2002; Huchtmeyer et al. 2005). This may suggest that the dynamics of the system are perturbed, but only an interferometric H I map can confirm this issue. The gas depletion timescale is longer than 2.6 Gyr, indicating that the galaxy still contains a huge amount of material to create future generations of stars.

3.13. SBS 1211+540

SBS 1211+540 was included in the study of chemical abundances in BCDGs performed by Izotov and collaborators (Izotov et al. 1991; Thuan et al. 1995; Izotov & Thuan 1998; Guseva et al. 2000; Izotov & Thuan 2004). WR features were firstly reported by Izotov et al. (1994), who detected the nebular He II $\lambda\lambda 4686$ emission line (Schaerer et al. 1999). However, the reanalysis performed by Guseva et al. (2000) only detects the broad emission line.

Figure 22 shows our ISIS 4.2 m WHT spectrum of the center of SBS 1211+540; Table A.11 compiles all its derived properties. The spectrum is dominated by the nebular emission and shows no trace of stellar absorption. We do not detect the blue WR bump or the nebular He II $\lambda\lambda 4686$ emission, although the spectrum is of low S/N (Fig. 36). The spectral range where the red WR bump is located was not observed, but this feature should not be expected because of the very low metallicity of SBS 1211+540.

3.13.1. Physical conditions of the ionized gas

We derive a very high electron temperature, $T(\text{O III}) = 17\,100 \pm 600 \text{ K}$, using the direct method (see Table A.12). The low ionization temperature was estimated by considering Garnett's relation. Both the [O II] $\lambda\lambda 3726, 3729$ and [S II] $\lambda\lambda 6717, 6731$ doublets were used to compute the electron density, which is $n_e = 320 \pm 50 \text{ cm}^{-3}$. The reddening coefficient was determined using all available H I Balmer lines with errors lower than 20%. The comparison of the emission-line ratios with the diagnostic diagrams confirms the starbursting nature of this BCDG.

3.13.2. Chemical abundances

Table A.12 compiles all the chemical abundances derived for SBS 1211+540. The oxygen abundance, $12 + \log(\text{O/H}) = 7.65 \pm 0.04$, and the N/O ratio, $\log(\text{N/O}) = -1.62 \pm 0.10$, are in

excellent agreement with the values given by Izotov & Thuan (1999). Hence, it is the lowest metallicity object analyzed in this work. The remaining chemical abundances, $\log(\text{S/O}) \sim -1.47$ and $\log(\text{Ne/O}) \sim -0.75$, are also similar to those determined by these authors.

3.13.3. Kinematics of the ionized gas

Figure 23 shows the position-velocity diagram obtained using the bidimensional spectrum of SBS 1211+540. The slit position we used, with a PA of 138° , crosses the center of the galaxy but not knot *a*, which, as explained in Sect. 3.13.2 of Paper I, also shows nebular emission. We extracted 4 pixel bins (0.8 arcsec) across the [O III] $\lambda\lambda 5007$ profile (the brightest line) and considered the velocity of the center as reference. The position-velocity diagram does not show a clear rotation pattern, only a change in the sense of the velocity gradient at the center of the galaxy. In any case, the amplitude of the velocity variations are very small. If we do not consider the four lowest points at the SE of Fig. 23, where we detected two faint plumes (see Fig. 21 of Paper I), we may assume that the kinematics is explained by rotation with a velocity gradient of $\sim 20\text{--}30 \text{ km s}^{-1}$.

Considering that the gas is rotating with the parameters described above, we may derive the Keplerian mass of the galaxy. Assuming $\Delta v \sim 30 \text{ km s}^{-1}$ within a radius of $\sim 5''$ (315 pc) and an inclination angle of $i \sim 50^\circ$ (value derived from the optical shape of the galaxy), we find $M_{\text{Kep}} \sim 1.13 \times 10^8 M_\odot$ and $M_{\text{Kep}}/L_B \sim 3.6$. Using the H I data provided by Huchtmeyer et al. (2005), we derive $M_{\text{HI}} = (2.4 \pm 0.4) \times 10^7 M_\odot$ and $M_{\text{dyn}} \sim 1.14 \times 10^8 M_\odot$, and hence $M_{\text{HI}}/M_{\text{dyn}} \sim 0.21$, $M_{\text{HI}}/L_B \sim 0.76$ and $M_{\text{dyn}}/L_B \sim 3.6$. That the dynamical mass (determined using radio data) and the Keplerian mass (estimated using our optical data) completely agree indicates that we have probably overestimated the rotation velocity of the ionized gas and/or the true extension of the neutral gas is much larger than the optical extent. If the first assumption is true, it would indicate that, besides rotation, there is an additional velocity component, which may be connected to the detection of a very faint plume at the NW in our deep optical images. In any case, the high proportion of neutral mass estimated for this BCDG (21%) and the high value for the gas depletion timescale, 2.5 Gyr, indicate that SBS 1211+540 contains a huge amount of fresh material available for the birth of new stars.

3.14. SBS 1319+579

The only bibliographic references of SBS 1319+579 are from Izotov and collaborators (Izotov et al. 1997; Izotov & Thuan 1998, 1999; Guseva et al. 2000; Izotov & Thuan 2004). Schaerer et al. (1999) included SBS 1319+579 in their WR galaxy catalogue because Izotov et al. (1997) reported the detection of the broad and nebular He II $\lambda\lambda 4686$ emission lines. Guseva et al. (2000) detected WNL and WCE populations in the galaxy.

We used the ISIS spectrograph at the 4.2 m WHT with a slit position of PA 39° to analyze the ionized gas along the main axis of the galaxy (see Fig. 23 of Paper I). We acquired spectroscopic data of regions A, B, C, *d*, and *e*, but we only analyzed those of A, B, and C because of their higher S/N. The spectra of the two brightest regions A and C are shown in Fig. 24, and Table A.13 compiles the dereddened flux ratios for all knots. Region B is the only one that exhibits stellar absorption in its spectra. We do not have a clear detection of the blue WR bump or the nebular He II

$\lambda 4686$ in any region (Fig. 36). A careful analysis of the spectrum indicates a tentative detection of both the broad and the nebular He II in knot A (see Paper III). We do not detect the red WR bump in that region (Fig. 37).

3.14.1. Physical conditions of the ionized gas

The [O III] $\lambda 4363$ line is measured in all regions and we could therefore determine $T_e(\text{O III})$ using the direct method. The low ionization electron temperatures were estimated using Garnett's relation. We found a significant difference in the electron temperatures found for the brightest regions A and C, $T_e(\text{O III}) \sim 13\,400$ and $11\,500$ K, respectively. The electron density, computed using the [S II] $\lambda\lambda 6317, 31$ doublet, was always at the low-density limit. The reddening coefficient derived for regions A and C is low and similar to the Galactic reddening. All regions can be classified as starbursts following the results given by the analysis of the diagnostic diagrams.

3.14.2. Chemical abundances

Because of a lack of [O II] $\lambda\lambda 3726, 29$ flux values, we used [O II] $\lambda\lambda 7318, 30$ to compute the O⁺ abundance. All the results for the chemical abundances derived in SBS 1319+579 are compiled in Table A.14. The oxygen abundance found in all regions are similar within the errors, $12+\log(\text{O/H}) \sim 8.10$, although that computed in region A, $12+\log(\text{O/H}) = 8.05 \pm 0.06$, is slightly lower than that found in region C, $12+\log(\text{O/H}) = 8.15 \pm 0.07$. Knot A shows a high excitation degree, $\log(\text{O}^{++}/\text{O}^+) = 0.77$, something that is not observed in the other regions. The N/O ratios are very similar in A and B [$\log(\text{N/O}) = -1.53 \pm 0.10$ in A] but also slightly different than in region C, which has $\log(\text{N/O}) = -1.38 \pm 0.10$. All the chemical abundances are consistent with those reported by Izotov & Thuan (1999).

3.14.3. Kinematics of the ionized gas

Figure 25 shows the position-velocity diagram obtained from our bidimensional spectrum using a slit position with PA 39°. We extracted 4 pixel bins (0.8 arcsec) across the H α profile. The relative intensity of the H α emission along the spatial direction is also shown in this figure. Although the velocity continuously decreases from the eastern regions ($v \sim -105 \text{ km s}^{-1}$) to the western areas ($v \sim 65 \text{ km s}^{-1}$) of the galaxy, the velocity gradient is not the same across the system. We observe two trends: between region C and region B (velocity difference of $\sim 40 \text{ km s}^{-1}$ in $30''$) and from region B to region A (velocity difference of $\sim 130 \text{ km s}^{-1}$ in $28''$). This behavior may suggest that there is a tidal stream moving from B to A in the direction away from the observer, but our deep images do not show any such tail or morphological feature that supports this hypothesis. Another explanation to this feature may be the assumption that they are two systems, as suggested by the morphology of the H α images and the chemical abundances that they may indicate with different kinematics and in interaction. If this idea is correct, we should expect to observe distortions in the kinematics of the gas with higher amplitudes than those we see. However, because of the high inclination angle that the galaxy seems to have, $i \sim 70^\circ$, we cannot discard either hypothesis.

Considering that the kinematic pattern is a consequence of the rotation of the galaxy and assuming that $i \sim 70^\circ$ and $\Delta v \sim 88 \text{ km s}^{-1}$ within a radius of $\sim 30''$ (4.2 kpc), we derive a Keplerian mass of $M_{\text{Kep}} \sim 8.6 \times 10^9 M_\odot$. The corresponding

mass-to-luminosity ratio, $M_{\text{Kep}}/L_B \sim 2.14$, is higher than that expected for a dwarf galaxy with the properties observed in SBS 1319+579. However, if we consider that only the NE region (from C to B) rotates with a $\Delta v \sim 45 \text{ km s}^{-1}$, we now find $M_{\text{Kep}} \sim 1.7 \times 10^9 M_\odot$ and $M_{\text{Kep}}/L_B \sim 0.42$, similar to the values found in other BCDGs (Huchtmeier et al. 2005). This seems to confirm that the kinematics surrounding region A are disturbed and not produced by rotation. Using the H I data provided by Huchtmeier et al. (2007), we derive $M_{\text{HI}} = 1.64 \times 10^9 M_\odot$ and $M_{\text{dyn}} \sim 1.4 \times 10^{10} M_\odot$, assuming a rotation velocity of 109 km s^{-1} within 4.5 kpc and the same inclination angle. The neutral gas accounts for only 12% of all the mass of the system. Its M_{dyn}/L_B value, ~ 3.5 , is as expected for BCDGs. However, the gas depletion timescale is extremely long for a starburst galaxy, $\tau \sim 10.8$ Gyr. This may suggest that the star formation is not very efficient in the system, perhaps because the H I gas has been expelled from the galaxy. An H I map obtained using a radio-interferometer that includes both SBS 1319+579 and the nearby spiral NGC 5113 would be fundamental to understanding the dynamics and evolution of this system.

3.15. SBS 1415+437

The first spectroscopic data of SBS 1415+437 were presented by Thuan et al. (1995), who determined an oxygen abundance of $12+\log(\text{O/H}) = 7.51$, making it then one of the lowest metallicity galaxies known. A later reanalysis of the same spectrum raised this value to 7.59 (Izotov & Thuan 1998, 1999; Thuan et al. 1999a). The spectra acquired exhibited broad and nebular He II emission lines, and SBS 1415+437 was therefore included in the latest WR galaxy catalogue (Schaerer et al. 1999). Subsequent spectroscopic analyses were published by Melbourne & Salzer (2002), Melbourne et al. (2004), Guseva et al. (2003), Izotov & Thuan (2004), and Lee et al. (2004).

Figure 26 shows the spectra of regions A and C obtained using the instrument ISIS at the 4.2 m WHT and a slit places at a PA 20° across the main body of the galaxy (see Fig. 25 of Paper I). Although we detected some emission lines in knot B, we have not analyzed its properties because of the low S/N of its spectrum. All spectra are dominated by nebular emission; no stellar absorption is detected. Table A.13 compiles all the line intensities ratios and other properties of the spectra. Although we do not see the broad blue WR bump, the nebular He II $\lambda 4686$ emission line is clearly detected in the spectrum of region C (Fig. 36). We do not observe the red WR bump (Fig. 37) despite the high S/N and spectral resolution.

3.15.1. Physical conditions of the ionized gas

The electron temperatures were computed using the direct method and are very high, $T(\text{O III}) = 16\,400$ and $15\,500$ K for C and A, respectively. The electron temperature of the low ionization potential ions, $T_e(\text{O II})$, was estimated using Garnett's relation. The electron density was derived using the [S II] $\lambda 6716, 31$ doublet and was below the low density limit. The reddening coefficient found in region C is extremely low, $c(\text{H}\beta) \sim 0.01$, and identical to that determined by Guseva et al. (2003). However, the higher value of $c(\text{H}\beta)$ in region A, $c(\text{H}\beta)=0.16$, suggests an inhomogeneous distribution of dust in the galaxy. The comparison of the observed [O III] $\lambda 5007/\text{H}\beta$ and [N II] $\lambda 6584/\text{H}\alpha$ ratios with the predictions given by the diagnostic diagrams confirm their starbursting nature.

3.15.2. Chemical abundances

Table A.14 compiles our results for the chemical abundances derived in SBS 1415+437. These data confirm the very low metallicity of the galaxy, the oxygen abundances being $12+\log(\text{O/H}) = 7.58 \pm 0.05$ (for C) and 7.61 ± 0.06 (for A). The N/O ratio for both objects, $\log(\text{N/O}) = -1.57 \pm 0.08$, is as expected for these low metallicities. Our results are in very good agreement with the abundances obtained by Guseva et al. (2003).

3.15.3. Kinematics of the ionized gas

The position-velocity diagram shown in Fig. 27 was obtained by extracting 4-pixel bins ($0.8''$) along the $\text{H}\alpha$ profile of our bidimensional spectrum. We took the velocity of the brightest object C as a reference. We observe that the velocity continuously decreases from the SW regions ($v \sim 30 \text{ km s}^{-1}$, where region A is located) to the NE areas ($v \sim -30 \text{ km s}^{-1}$, where region B is found), which may be attributed to the rotation of the galaxy. Some kinematic divergences are detected between regions A and C. However, because of the low amplitude of these variations (less than 15 km s^{-1}), they may just be a consequence of local movements in the ionized gas. Our position-velocity diagram is similar in both shape and values to that obtained by Thuan et al. (1999a) using a slit with a PA of 22° (see their Fig. 10). They also reported the peculiar kinematical behavior that we observe between A and C.

The Keplerian mass that we estimate for this galaxy, assuming a rotation velocity of $\sim 30 \text{ km s}^{-1}$ within a radius of $\sim 25''$ (1.13 kpc) and an inclination angle of $i \sim 75^\circ$ (determined using the shape of the galaxy we see in our optical images), is $M_{\text{Kep}} \sim 2.5 \times 10^8 M_\odot$, and its mass-to-luminosity ratio $M_{\text{Kep}}/L_B = 2.5$. The H I mass estimated by Huchtmeier, Krishna & Petrosian (2005) is $M_{\text{HI}} = (9.64 \pm 0.65) \times 10^7 M_\odot$. Using their data of W_{HI} and considering a radius of $40''$ (1.8 kpc), we estimate a dynamical mass of $M_{\text{dyn}} = 4.9 \times 10^8 M_\odot$. With these data, we derive $M_{\text{HI}}/L_B = 0.96$, $M_{\text{dyn}}/L_B = 4.9$, and $M_{\text{HI}}/M_{\text{dyn}} = 0.20$, which are the typical values found for BCDGs (Salzer et al. 2002; Huchtmeier et al. 2005). These estimations are more reliable than those given by Thuan et al. (1999a) because we use recent data of high sensitivity. Both the gas depletion timescale (~ 3.2 Gyr) and that 1/5 of the mass of the system is neutral gas indicate that SBS 1415+437 contains a huge reservoir of fresh material available for new star-forming phenomena.

3.16. III Zw 107

III Zw 107 was analyzed using spectroscopy by Sargent (1970), Gallego et al. (1997), and Kunth & Joubert (1985). The last set of authors detected a continuum excess in the spectral region of the blue WR bump in the southern object, and hence Schaerer et al. (1999) included this BCDG in their catalogue of WR galaxies.

A slit with a PA of 0° was used in the IDS spectrograph at the 2.5 m INT to observe III Zw 107 (see Fig. 27 of Paper I). Three different regions, A, B, and C, were studied. The optical spectra of regions A and B are shown in Fig. 28. Region A exhibits important underlying stellar absorption features. The faint region C is not clearly evident in our optical images, but is clearly identified at the north of region B in our bidimensional spectrum. Table A.15 compiles all the emission intensity ratios and other properties of the spectra of III Zw 107. We clearly detect the broad He II $\lambda 4686$ feature in the spectrum of knot A (Fig. 36), the same region that Kunth & Joubert (1985) classified as WR-rich. However, we do not see the red WR bump (Fig. 37)

perhaps because of the relatively low spectral resolution of these 2.5 m INT spectra. The [O III] $\lambda\lambda 4959, 5007$ and $\text{H}\alpha$ emission lines have broad wings in their profiles, which is more evident in the spectrum of region A.

3.16.1. Physical conditions of the ionized gas

In region A, we computed both $T_e(\text{O III})$ and $T_e(\text{O II})$ using the direct method because of the detection of [O III] $\lambda 4363$ and the [O II] $\lambda\lambda 7319, 7330$ doublet. The values are $T_e(\text{O III}) = 10\,900 \pm 900 \text{ K}$ and $T_e(\text{O II}) = 10\,500 \pm 800 \text{ K}$. The electron temperatures of knots B and C were estimated using empirical calibrations. All results are compiled in Table A.16. The electron density was computed using the [S II] $\lambda\lambda 6716, 6731$ doublet at the low-density limit for regions B and C.

The comparison of the spectra shown in Fig. 28 indicates that the spectral energy distribution of the continuum in region A is shallower than that observed in region B. This effect may be explained by the contribution of a more evolved stellar population in A. However, the analysis of the reddening coefficient using the H I Balmer lines of this regions infers a much higher value in region A, $c(\text{H}\beta) \sim 0.68$, than in region B, $c(\text{H}\beta) \sim 0.15$, and hence it seems that a difference in extinction is the correct explanation of the different slope of the continuum. The diagnostic diagrams for all regions agree with the loci of typical H II regions.

3.16.2. Chemical abundances

Table A.16 lists all the chemical abundances computed for the bursts analyzed in III Zw 107. The oxygen abundance of the region A, derived using the direct method, is $12+\log(\text{O/H}) = 8.23 \pm 0.09$. This value is similar to that reported by Kunth & Joubert (1985), but more than 0.3 dex higher than that reported by Gallego et al. (1997). The oxygen abundances of regions B and C were estimated using the Pilyugin (2001a,b) empirical calibrations, yielding values of $12+\log(\text{O/H}) \sim 8.31$, similar to the abundance of region A within the errors. The rest of the chemical abundances are also similar in all regions, just being slightly lower in A. The results of the chemical abundances found between B and C are essentially identical apart from all the uncertainties involved in their determination.

3.16.3. Kinematics of the ionized gas

The position-velocity diagram obtained using our bidimensional spectrum is shown in Fig. 29. We extracted 3-pixel bins (1.2 arcsec) along the $\text{H}\alpha$ profile, taking as reference the velocity of region A, the brightest knot. We observe a negative velocity gradient between the southern regions of the galaxy ($\sim 30 \text{ km s}^{-1}$) and region A ($\sim -20 \text{ km s}^{-1}$), but between this knot and region B a reversal of the velocity of $\sim 40 \text{ km s}^{-1}$ is observed within $4''$. The velocity difference between region B and C is $\sim -40 \text{ km s}^{-1}$. Hence, although the velocity amplitudes are not large and the spatial resolution is not very high, the position-velocity diagram seems to exhibit a sinusoidal pattern. This feature is indicative of interaction or merging phenomena between the two brightest knots seen in III Zw 107. This hypothesis would explain the existence of the tail found in the deep optical images (see Fig. 27 of Paper I). It is also possible that the velocity gradient observed in the south of the galaxy is a consequence of the movement of the ionized gas within/towards that tail.

We estimated a tentative value of the Keplerian mass of III Zw 107 using the position-velocity diagram shown in Fig. 29. Considering that we observe the galaxy edge-on ($i \sim 90^\circ$) and assuming that $\Delta v \sim 30 \text{ km s}^{-1}$ within a radius of $\sim 10''$ (3.9 kpc), we estimate that $M_{\text{Kep}} \sim 8.2 \times 10^8 M_\odot$ and $M_{\text{Kep}}/L_B \sim 0.05$. These values are very low compared to the neutral gas mass and the dynamical mass derived using the radio data (Paturel et al. 2003), i.e., $M_{\text{HI}} = (6.7 \pm 1.2) \times 10^9 M_\odot$, and $M_{\text{dyn}} \sim 1.8 \times 10^{10} M_\odot$ (dynamical mass being estimated using a radius of $20'' = 7.8 \text{ kpc}$ and half of the H I width, $\sim 100 \text{ km s}^{-1}$), and the mass-to-luminosity ratios derived from them, $M_{\text{HI}}/L_B = 0.38$ and $M_{\text{dyn}}/L_B \sim 1$. If all these values are precise, around 37% of the mass of the system is neutral gas. We consider that, because of the detection of an important population of old stars within the galaxy and its relatively high metallicity, the dynamical mass of III Zw 107 has probably been underestimated. Hence, the H I distribution should be several times larger than the optical extent. The comparison of the velocity amplitudes in the optical ($\sim 30 \text{ km s}^{-1}$) and the radio ($\sim 100 \text{ km s}^{-1}$) data strongly supports this idea. Perhaps, the neutral gas has been expelled and/or dispersed as a consequence of the possible interaction or merging between the two main objects observed in III Zw 107. An interferometric H I map of this galaxy is needed to answer all of these issues. In any case, the gas depletion timescale is high, $\tau \sim 3.5 \text{ Gyr}$, indicating that there is still a lot of neutral gas available to form new stars.

3.17. Tol 9

The WR nature of Tol 9 remains a controversial topic. Penston et al. (1977) tentatively detected a faint emission line around $\lambda 4686$. Kunth & Schild (1986) did not find the blue WR bump or the He II emission line, but suggested the detection of the red WR bump. Both Conti (1991) and Schaerer et al. (1999) included Tol 9 in their lists of candidate WR galaxies.

We observed two slit positions of Tol 9 (see Fig. 29 of Paper I). For the first one, we used the IDS instrument at the 2.5 m INT, using a slit with a PA of 49° that crosses the center of Tol 9 and the dwarf companion galaxy located at the SW. The second slit position was observed with the ALFOSC instrument at the 2.56 m NOT, by selecting a slit position almost perpendicular to that used at the 2.5 m INT. This final slit position was centered on the SW of the center of the galaxy and the PA was set to be 109° , our main objective was to analyze the kinematics and properties of the filamentary structure of ionized gas found in our deep H α images (see Fig. 30 of Paper I). The list of all the emission lines observed using both slits, as well as other important properties of the spectra, are shown in Table A.15. As we can see, both spectra show very similar line intensities. We note that the radial velocity obtained for Tol 9 using our optical spectra is $\sim 200 \text{ km s}^{-1}$ more positive than the value previously reported and listed in the NED (Lauberts & Valentijn 1989).

The spectra obtained for Tol 9 show nebular emission and a continuum dominated by stellar absorption in the H I Balmer lines. We also observe an important decrement in the continuum in the blue range of the spectra. This feature can be explained by both the contribution of the older stars and high extinction. We detect both the blue WR bump and the nebular He II $\lambda 4686$ emission line in the 2.5 m INT spectrum (Fig. 36), which are indicative of WNL stars at the center of Tol 9. However, we do not have a clear detection of the red WR bump (Fig. 37), although there is some evidence that there are there. If WNL stars are seen in Tol 9, WCE stars should also exist because of the high

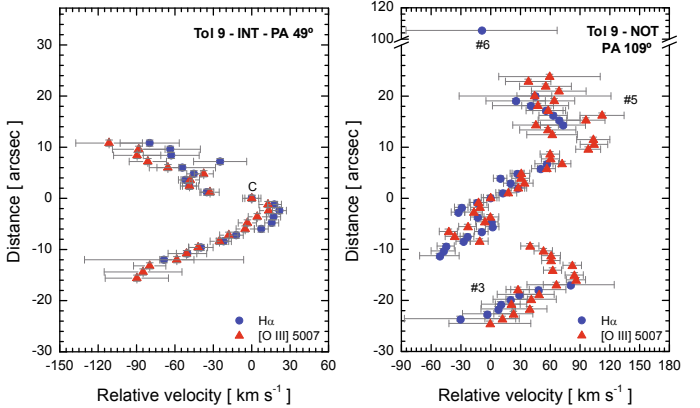


Fig. 31. Position-velocity diagrams for the slit positions observed in Tol 9: PA 49° (left, using 2.5 m INT data) and PA 109° (right, using 2.56 m NOT data). Both the H α (circles) and the [O III] $\lambda 5007$ (triangles) profiles were analyzed. We note that the y -axis is broken into two parts in the right diagram. NE is up in the left diagram and NW is up in the right diagram. See Figs. 29 and 30 in Paper I for identification of the regions.

metallicity of the ionized gas. Deep spectroscopy of higher S/N and spectral resolution is therefore needed to confirm the reality of this feature.

3.17.1. Physical conditions of the ionized gas

The 2.5 m INT spectrum of Tol 9 shows [O III] $\lambda 4363$, [N II] $\lambda 5755$, and the [O II] $\lambda\lambda 7319, 7330$ doublet, and hence we derived the electron temperatures using the direct method. The results (which are compiled in Table A.16) are $T_e(\text{O III}) \sim 7600 \text{ K}$ and $T_e(\text{low}) \sim 8300 \text{ K}$. For the spectrum obtained using the 2.56 m NOT data, we computed $T_e(\text{O II})$ using the [O II] lines and estimated the $T_e(\text{O III})$ using Garnett's relation. In all cases, the electron densities were in the low-density limit. As we said, the values for the reddening coefficients are high, about $c(\text{H}\beta) \sim 0.45$. The absorption equivalent widths of the H I Balmer lines, computed interactively with $c(\text{H}\beta)$, are large and infer values of $W_{\text{abs}} \sim 6-8 \text{ \AA}$. The comparison of the data with the diagnostic diagrams classifies all regions as starbursts, but it seems that there is a small shock contribution to the ionization of the gas in the region analyzed with the 2.56 m NOT spectrum.

3.17.2. Chemical abundances

Table A.16 compiles all the chemical abundances computed in Tol 9, showing almost identical results for both spectra. The average value of the oxygen abundance derived using the direct method is $12 + \log(\text{O/H}) = 8.57 \pm 0.10$. This value is around 0.8 dex higher than that provided by Kunth & Schild (1986). The average N/O ratio, $\log(\text{N/O}) = -0.81 \pm 0.11$, is as the expected for a galaxy of the oxygen abundance found in Tol 9. The rest of the chemical abundances computed for this galaxy averaging both set of data are $\log(\text{S/O}) = -1.62 \pm 0.12$, $\log(\text{Ne/O}) = -0.72 \pm 0.14$, and $\log(\text{Ar/O}) = -2.45 \pm 0.15$.

3.17.3. Kinematics of the ionized gas

The kinematics of the ionized gas in Tol 9 were analyzed using our bidimensional spectra. We extracted 3-pixel bins ($1.2''$) and 5-pixel bins ($0.95''$) along the H α and the [O III] $\lambda 5007$ profiles for the 2.5 m INT and the 2.56 m NOT spectra, respectively.

The reference velocity was always chosen in the brightest region. The position-velocity diagrams are shown in Fig. 31. Although the diagrams show excellent agreement between the H α and the [O III] $\lambda 5007$ results, their interpretation is not easy.

First, the diagram with AP 49°, which crosses the center of Tol 9, does not show a rotation pattern. Indeed, we observe two velocity gradients: while the velocity changes $\sim 120 \text{ km s}^{-1}$ from the NE regions to the center, this trend is completely reversed in the SW region, which shows a velocity variation of $\sim -120 \text{ km s}^{-1}$. We note that the center of Tol 9 is not located at the (0, 0) position in this diagram because the maximum of the H α emission is displaced $\sim 10''$ towards the SW of the center. Perhaps the velocity pattern that we observed at this PA is a combination of rotation in the center and NE areas and the velocity gradient produced by the optical tail that we detected in our deep optical images that connects Tol 9 with a dwarf companion galaxy located at the SW (see Fig. 29 of Paper I). Assuming $\Delta v \sim 70 \text{ km s}^{-1}$ within a radius of $\sim 12''$ (2.5 kpc) and an inclination angle of $i \sim 50^\circ$, we estimate a Keplerian mass of $\sim 1.2 \times 10^9 M_\odot$ and a mass-to-luminosity ratio of $M_{\text{Kep}}/L_B \sim 0.16$. This last value is very low compared with that found in similar objects, and we therefore propose that the galaxy mass has been underestimated. Interferometric H I measurements would be required needed to reliably estimate the dynamical mass of this galaxy because single-dish observations (such as those provided by HIPASS) would blend the H I gas in Tol 9 and the nearby spiral ESO 436-46. This analysis will be performed using new H I ATCA data for the galaxy group in which Tol 9 resides obtained by our group (López-Sánchez et al. 2010). Using the FIR fluxes, the warm dust mass is $M_{\text{dust}} \sim 2.41 \times 10^6 M_\odot$. Following the analysis performed by Bettoni et al. (2003), the derived mass-to-luminosity ratio, $M_{\text{dust}}/L_B \sim 3.1 \times 10^{-4}$, agrees with the typical value found in spiral galaxies ($M_{\text{dust}}/L_B \sim 2 \times 10^{-4}$).

On the other hand, the position-velocity diagram obtained using the slit at a PA 109°, shows several reversals in the sense of the velocity of the ionized gas. Regions #3 and #5, which are identified as two filamentary structures using our deep H α map (see Fig. 30 of Paper I), are labeled in this diagram. They exhibit a similar kinematic behavior, i.e., a variation of $\sim -90 \text{ km s}^{-1}$ in their velocities within the same distance, $\sim 12''$ (2.5 kpc), with respect to the center of the system. This kinematic structure, which is not spatially coincident with any recognizable stellar distribution, resembles an expanding bipolar bubble, reinforcing the hypothesis that the H α envelope surrounding Tol 9 is a consequence of some kind of galactic wind. Knot #6 is barely detected at around 100'' (21 kpc) from the maximum of H α emission, but seems to show a radial velocity similar to that observed at the end of the filament #5. This suggests that knot #6 has been kinematically coupled to the main filamentary structure. Maybe, knot #6 was expelled from the expanding bubble. We would require 3D optical spectroscopy to clarify these issues, as well as to compare the kinematics of the stellar and ionized gas components.

3.18. Tol 1457-262

Tol 1457-262 was studied using spectroscopy by Winkler (1988), Terlevich et al. (1991), Kewley et al. (2001), Westera et al. (2004), and Buckalew et al. (2005). Schaerer et al. (1999) included Tol 1457-262 in their WR galaxy catalogue because Contini (1996) detected the broad He II $\lambda 4686$ emission line in the brightest region of the western object. This feature was also reported by Pindao (1999). Both authors also detected WR features in another region of the same object, although while

Contini (1996) observed the nebular He II $\lambda 4686$ emission line, Pindao (1999) only reported the detection of the blue WR bump.

Figure 32 shows the spectra extracted for regions A, B, and C of the western object in Tol 1457-262 (*Object 1*, see Fig. 31 of Paper I) using the instrument ALFOSC at the 2.56 m NOT and a slit with a PA of 155°. Table A.17 compiles all the line intensity ratios and other properties of all the spectra analyzed in this galaxy. Stellar absorption is barely detected, indicating that the nebular emission strongly dominates their spectra. Broad low-intensity wings are detected in the H α profile in region A. We observe the nebular He II $\lambda 4686$ emission line in the spectrum of region A; this feature is also observed in the spectrum of region B (Fig. 36). We do not see either the blue or the red (Fig. 37) WR bumps in any region in spite of the high S/N of the spectra.

3.18.1. Physical conditions of the ionized gas

The electron temperatures were computed using the direct method because of the detection of [O III] $\lambda 4363$ and [O II] $\lambda\lambda 7318, 7330$ lines in all spectra. The derived values, which are compiled in Table A.18, agree well with the empirical relation between $T_e(\text{O II})$ and $T_e(\text{O III})$ provided by Garnett (1992). Despite the similarity in their ionization degree, region B has an electron temperature, $T_e(\text{O III}) \sim 15\,200 \text{ K}$, which is higher than that found in regions A and C, $T_e(\text{O III}) \sim 14\,000 \text{ K}$. The electron densities found in regions A and C are similar, $n_e \sim 200 \text{ cm}^{-3}$, but in region B, n_e is at the low density limit. The determination of the reddening coefficient for region A was completed using 5 H I Balmer ratios, yielding consistently a very high value, $c(\text{H}\beta) = 0.83 \pm 0.03$. However, the $c(\text{H}\beta)$ found in region B inferred a negative value. This result cannot be attributed to poor flux calibration because the adjacent regions A and C do not have this problem. Hence, we assumed $c(\text{H}\beta) \sim 0$ in region B⁴ and scaled the blue and red spectra by considering the theoretical ratio between the H α and H β fluxes for the electron temperature estimated for this region. The comparison of the emission line ratios with the diagnostic diagrams indicates that all regions can be classified as starbursts.

3.18.2. Chemical abundances

The chemical abundances computed for the regions analyzed in Tol 1457-262 are listed in Table A.18. The oxygen abundance derived for the brightest knot (region A) is $12+\log(\text{O/H}) = 8.05 \pm 0.07$, similar to that found in the adjacent region C, $12+\log(\text{O/H}) = 8.06 \pm 0.11$, but higher than the oxygen abundance computed in region B, $12+\log(\text{O/H}) = 7.88 \pm 0.07$. This would suggest that regions A and B have experienced different chemical evolution. However, the remaining chemical abundances are relatively similar in all regions and only slightly higher in A and C. The [N II] emission lines are remarkably weak, inferring $\log(\text{N/O}) = -1.57 \pm 0.11$ and -1.61 ± 0.12 for A and B, respectively. Our results do not agree with those reported by Masegosa et al. (1994) for region A, for which they computed $12+\log(\text{O/H}) = 8.23$. These are the first abundance determinations for the remaining objects.

3.18.3. Kinematics of the ionized gas

Figure 33 shows the position-velocity diagram of the slit position with PA 155° analyzed in *Object 1* in Tol 1457-262. We

⁴ However, the Galactic value using Schlegel, Finkbeiner & Davis (1998) is $c(\text{H}\beta) = 0.23 \pm 0.02$.

extracted 5-pixel bins ($0.95''$) along the $\text{H}\alpha$ profile and took as reference the center of region A (the maximum of the $\text{H}\alpha$ emission). Figure 33 includes the relative intensity of the $\text{H}\alpha$ emission along the spatial direction. Although a velocity gradient between the northern regions ($v \sim -120 \text{ km s}^{-1}$) and the southern areas ($v \sim 190 \text{ km s}^{-1}$) is seen, we notice several reversals in the direction of the velocity across the system, the most important being that found between regions A and C, which has an amplitude larger than 100 km s^{-1} . These features indicate that the kinematics of the different star-forming regions found within *Object 1* of Tol 1457-262 are decoupled. Indeed, the observed sinusoidal pattern suggests that the system is experiencing a merging process. The rapid increase in the velocity between knot B and the southernmost regions may be related to the movement of the material within the faint tail that we detected in our deep optical images (see Fig. 31 of Paper I). We consider knot C to be a TDG candidate because its kinematics and chemical abundances are similar to those derived in bright region A.

Assuming that the general kinematical pattern is a consequence of rotation, we derived a tentative Keplerian mass of $M_{\text{Kep}} \sim 6.2 \times 10^9 M_\odot$ and a mass-to-luminosity ratio of $M_{\text{Kep}}/L_B \sim 0.34$ for *Object 1* in Tol 1457-262. We considered $\Delta v \sim 60 \text{ km s}^{-1}$ within a radius of $r \sim 15''$ (4.95 kpc) and an inclination angle of $i \sim 55^\circ$ (from our optical images). HIPASS provides a detection of the HI gas in this galaxy, for which we derive $M_{\text{HI}} = 4.7 \times 10^9 M_\odot$. However, this estimation for the neutral gas mass is for all objects within Tol 1457-262 and therefore an interferometric HI map is needed to quantify the amount of HI and the dynamical mass of each member. The total luminosity of the system, computed from our optical data, is $L_B = 1.82 \times 10^{10} L_\odot$, and hence the neutral hydrogen mass-to-luminosity ratio of Tol 1457-262 is $M_{\text{HI}}/L_B \sim 0.26$. This value is higher than the typical M_{HI}/L_B found in similar galaxies, indicating the large amount of neutral gas in Tol 1457-262.

3.19. Arp 252

Arp 252 is a pair of interacting galaxies referred to as ESO 566-8 (galaxy A) and ESO 566-7 (galaxy B). Their spectroscopic properties were analyzed by Peña et al. (1991) and Masegosa et al. (1991). These authors detected the blue WR bump in ESO 566-7⁵. The WR feature was confirmed by Pindao (1999), and hence ESO 566-7 was included in the latest catalogue of WR galaxies (Schaerer et al. 1999). Contini (1996) reported a tentative detection of the nebular $\text{He II } \lambda 4686$ emission line in ESO 566-8, and therefore listed it as a suspected WR galaxy (Schaerer et al. 1999).

Figure 34 shows the optical spectra of ESO 566-8 and ESO 566-7 obtained using the instrument ALFOSC at the 2.56 m NOT using a slit with PA 342° (see Fig. 34⁶ in Paper I). The spectrum of ESO 566-8 contains many emission lines, but the spectrum of ESO 566-7 shows only a few. All line intensity ratios are listed in Table A.17. Although the spectra are dominated by the emission of the ionized gas, they also exhibit stellar absorption, which is more evident in the weakest HI Balmer lines observed in ESO 566-7. We detect the nebular $\text{He II } \lambda 4686$ emission line within a faint broader feature in the spectrum of ESO 566-8 (Fig. 36). The red WR bump is also observed in this object (Fig. 37), confirming the presence of both WNL and WCE

stars in this galaxy. Although both Masegosa et al. (1991) and Pindao (1999) detected the blue WR bump in ESO 566-7, our spectrum does not show this feature. This may be because of the slit position chosen to acquire the spectrum of this galaxy, which does not cross the major body of ESO 566-7 but is almost perpendicular to it (see Fig. 34 in Paper I).

3.19.1. Physical conditions of the ionized gas

The detection of the $[\text{O II}] \lambda\lambda 7318,7329$ doublet and the $[\text{N II}] \lambda 5755$ emission line in the spectrum of ESO 566-8 allowed the direct determination of the low ionization electron temperature, inferring values of $T_e(\text{O II}) \sim 9300 \text{ K}$ and $T_e(\text{N II}) \sim 9000 \text{ K}$. Averaging these numbers, we estimate that $T_e(\text{low}) = 9100 \pm 800 \text{ K}$. The high ionization electron temperature was computed using Garnett's relation. The electron temperatures in ESO 566-7 were estimated with empirical calibrations. The electron densities were derived using the $[\text{S II}] \lambda\lambda 6617,6730$ doublet. All results are tabulated in Table A.18. The reddening coefficients are $c(\text{H}\beta) \sim 0.49$ in ESO 566-8 and $c(\text{H}\beta) \sim 0.27$ in ESO 566-7. The comparison of the observed emission line ratios with the diagnostic diagrams indicates that the nature of the ionization of the gas in ESO 566-7 is photoionized, but some shock contribution seems to be present in ESO 566-8.

3.19.2. Chemical abundances

Table A.18 compiles all the chemical abundances derived for the galaxy members of Arp 252. The oxygen abundance in ESO 566-8 (galaxy A) is $12+\log(\text{O/H})=8.46 \pm 0.11$ and was computed using the direct method. The empirical calibration provided by Pilyugin (2001a) suggests that the oxygen abundance in ESO 566-7 (galaxy B) is $12+\log(\text{O/H}) = 8.50 \pm 0.16$, similar to that found in ESO 566-8. The N/O ratio is also similar in both galaxies, $\log(\text{N/O}) = -0.76 \pm 0.12$ in ESO 566-8. The value of the oxygen abundance in ESO 566-7 reported by Masegosa et al. (1991), $12+\log(\text{O/H}) = 8.54$, agrees with our estimate.

3.19.3. Kinematics of the ionized gas

Figure 35 shows the position-velocity diagram obtained for Arp 252 analyzing the bidimensional spectrum using a slit of PA 342° . The $\text{H}\alpha$ profile was analyzed by extracting 5-pixel bins ($0.95''$) and taking as reference the maximum of the emission in ESO 566-8. As we can see, both galaxies have a slight velocity difference of 50 km s^{-1} between their centers. However, we observe important differences in the kinematics of the galaxies: while A seems to be rotating in its central regions (there is a velocity change from -130 km s^{-1} in the north to 100 km s^{-1} in the south), B shows a distorted kinematical pattern. The velocity gradients observed in the upper and lower regions of galaxy A may correspond to the tidal streams induced in the long tails that we observe in the optical images (see Fig. 34 of Paper I).

We performed a tentative determination of the Keplerian mass of the galaxies. We assumed a velocity of $\Delta v \sim 100 \text{ km s}^{-1}$ within a radius of $r \sim 5''$ (3.15 kpc) in ESO 566-8 and a velocity of $\Delta v \sim 30 \text{ km s}^{-1}$ within a radius of $r \sim 3''$ (1.89 kpc) in ESO 566-7. For both we considered an inclination angle of $i = 90^\circ$, hence our Keplerian mass determinations are low limits to the true values. We consider, however, that this assumption is accurate because in ESO 566-8 the northern tidal tail has a high inclination angle with respect to the plane of the sky and

⁵ Masegosa et al. (1991) named this object C 0942-1929A, but it is incorrect following Schaerer et al. (1999).

⁶ Notice that the true slit position in Fig. 34 of Paper I is $342^\circ = -18^\circ$ and not 18° .

ESO 566-7 has a long southern tail almost in the plane of the sky and its disk seems to be edge-on. We estimated Keplerian masses of $M_{\text{Kep}} \sim 7.3 \times 10^9 M_{\odot}$ for ESO 566-8 and $M_{\text{Kep}} \sim 4.0 \times 10^8 M_{\odot}$ for ESO 566-7, which indicate mass-to-luminosity ratios of $M_{\text{Kep}}/L_B \sim 0.21$ and 0.05 for ESO 566-8 and ESO 566-7, respectively. We consider that the Keplerian mass in ESO 566-7 has been highly underestimated. The warm dust mass of Arp 252, computed using the *FIR* fluxes, is $M_{\text{dust}} \sim 6.3 \times 10^6 M_{\odot}$.

Arp 252 is not detected in HIPASS, and hence we cannot derive the neutral gas mass and the dynamical mass. However, considering the absolute magnitude of the main galaxy, $M_B = -20.9$, and despite the distance to the system ($D \sim 130$ Mpc) we should expect to detect some H I emission. Hence, either Arp 252 does not have much neutral gas or it has been lost in the intergalactic medium because of tidal effects. Finally, it would be very interesting to analyze the kinematics of knots *c* and *d* to check their probable TDG nature (see Fig. 34 of Paper I).

3.20. NGC 5253

The echelle spectrophotometric analysis of the BCDG NGC 5253 was presented in López-Sánchez et al. (2007). We measured the intensities of a large number of permitted and forbidden emission lines in four zones of the central part of the galaxy. The physical conditions of the ionized gas were derived using a large number of different line intensity ratios. Chemical abundances of He, N, O, Ne, S, Cl, Ar, and Fe were determined following the standard methods. We detected, for the first time in a dwarf starburst galaxy, faint C II and O II recombination lines. We confirmed the presence of a localized N enrichment in certain zones of the center of the galaxy and suggested a possible slight He overabundance in the same areas. We demonstrated that the enrichment pattern agrees with that expected for the pollution by the ejecta of WR stars. The amount of enriched material needed to produce the observed overabundance is consistent with the mass lost by the number of WR stars estimated in the starbursts.

The analysis of the H I data provided by the *Local Volume H I Survey* project (Koribalski 2008) shows that the neutral gas kinematics within NGC 5253 has a velocity gradient along the optical minor axis of the galaxy; it does not show any sign of regular rotation (López-Sánchez et al. 2008). Some authors suggested that this feature is an outflow, but its origin is most likely the disruption/accretion of a dwarf gas-rich companion (Kobulnicky & Skillman 2008) or the interaction with another galaxy in the M 83 subgroup. The finding of a distorted H I morphology in the external parts of the galaxy supports this hypothesis. A comprehensive analysis of the neutral gas within NGC 5253 will be presented elsewhere (López-Sánchez et al. 2010).

4. Summary

We have presented a detailed analysis of the ionized gas within 16 Wolf-Rayet galaxies using long-slit intermediate-resolution optical spectroscopy. In many cases, more than two star-forming regions have been studied per galaxy. We have analyzed the physical properties of the ionized gas, deriving their electron temperatures, electron density, reddening coefficient, and stellar absorption from their H I Balmer lines. We have confirmed that the excitation mechanism of the ionized gas in all bursts is mainly photoionization and not due to shock excitation as it occurs in AGNs and LINERs. In the majority of cases, we have computed the chemical abundances of O, N, S, Ne, Ar, and Fe using the direct determination of the electron temperature (see

Table 2. Comparison between the oxygen abundance of the regions analyzed here and their previous estimations compiled from the literature.

Galaxy	T_e	12+log(O/H)		
		This work	Previous W.	Ref.
HCG 31 AC	D	8.22 ± 0.05	8.31 8.3 ± 0.2	VC92 R03
HCG 31 A1	EC	8.22 ± 0.10
HCG 31 B	D	8.14 ± 0.08	8.34 ± 0.20	R03
HCG 31 E	D	8.13 ± 0.09
HCG 31 F1	D	8.07 ± 0.06	8.1 ± 0.2	R03
HCG 31 F2	D	8.03 ± 0.10
HCG 31 G	D	8.15 ± 0.07
HCG 31 H	EC	8.3 ± 0.2
Mkn 1087	EC	8.57 ± 0.10	8.55	VC92
Mkn 1087 N	EC	8.23 ± 0.10
Mkn 1087 #7	EC	8.54 ± 0.10
Haro 15 C	EC	8.37 ± 0.10	8.33	S05
Haro 15 A	D	8.10 ± 0.06
Haro 15 B	EC	8.21 ± 0.14
Mkn 1199	D	8.75 ± 0.12	8.19 ± 0.18 9.13	IT98 GIT00
Mkn 1199 NE	EC	8.46 ± 0.13
Mkn 5 A	D	8.07 ± 0.04	8.04 ± 0.04	IT99
Mkn 5 B	EC	7.89 ± 0.17
IRAS 08208+2816 C	D	8.33 ± 0.08
IRAS 08208+2816 #8	EC	8.64 ± 0.15
IRAS 08339+6517	EC	8.45 ± 0.10
IRAS 08339+6517 c.	EC	8.38 ± 0.10
POX 4	D	8.03 ± 0.04	7.97 ± 0.02	KS96
POX 4 comp.	EC	8.03 ± 0.14
UM 420	D	7.95 ± 0.05	7.93 ± 0.05	IT98
SBS 0926+606 A	D	7.94 ± 0.08	7.95 ± 0.01	IT98
SBS 0926+606 B	EC	8.15 ± 0.16
SBS 0948+532	D	8.03 ± 0.05	8.00 ± 0.01	IT98
SBS 1054+365	D	8.00 ± 0.07	7.97 ± 0.02	IT98
SBS 1054+365 b	EC	8.13 ± 0.16
SBS 1211+540	D	7.65 ± 0.04	7.64 ± 0.01	IT98
SBS 1319+579 A ^a	D	8.05 ± 0.06	8.13 ± 0.01 8.09 ± 0.03	ITL97 IT99
SBS 1319+579 B ^a	D	8.12 ± 0.10	7.95 ± 0.10	ITL97
SBS 1319+579 C ^a	D	8.15 ± 0.07	8.15 ± 0.03 8.11 ± 0.01	ITL97 IT99
SBS 1415+437 C	D	7.58 ± 0.05	7.61 ± 0.01	G03
SBS 1415+437 A	D	7.61 ± 0.06	7.62 ± 0.03	G03
III Zw 107 A	D	8.23 ± 0.09	8.20 7.90	KJ85 G97
III Zw 107 B,C	EC	8.31 ± 0.12
Tol 9	D	8.57 ± 0.10	7.73	KS86
Tol 1457-262 A	D	8.05 ± 0.07	8.23	M94
Tol 1457-262 B	D	7.88 ± 0.07
Tol 1457-262 C	D	8.06 ± 0.11
ESO 566-8	D	8.46 ± 0.11
ESO 566-7	EC	8.50 ± 0.16	8.54	M91
NGC 5253 A	D	8.18 ± 0.04	8.12 ± 0.06	K97
NGC 5253 B	D	8.19 ± 0.04	8.19 ± 0.07	K97
NGC 5253 C	D	8.28 ± 0.04	8.16 ± 0.12	K97
NGC 5253 D	D	8.31 ± 0.07

The second column indicates if T_e was computed using the direct method (D) or via empirical calibrations (EC) in this work.^a We follow ITL97 names in SBS 1319+579. Notice, however, than IT99 named region A to SBS 1319+579 C and region B to SBS 1319+579 A; they did not consider SBS 1319+579 B because of its higher uncertainties. References: G97: Gallego et al. (1997); GIT00: Guseva et al. (2000); G03: Guseva et al. (2003); IT98: Izotov & Thuan (1998); IT99: Izotov & Thuan (1999); KS96: Kobulnicky & Skillman (1996); K97: Kobulnicky et al. (1997); KJ85: Kunth & Joubert (1985); KS86: Kunth & Schild (1986); M91: Masegosa et al. (1991); M94: Masegosa et al. (1994); R03: Richer et al. (2003); S05: Shi et al. (2005); VC92: Vacca & Conti (1992).

second column in Table 2). When these data were not available, we used the empirical calibration of Pilyugin (2001a,b) to

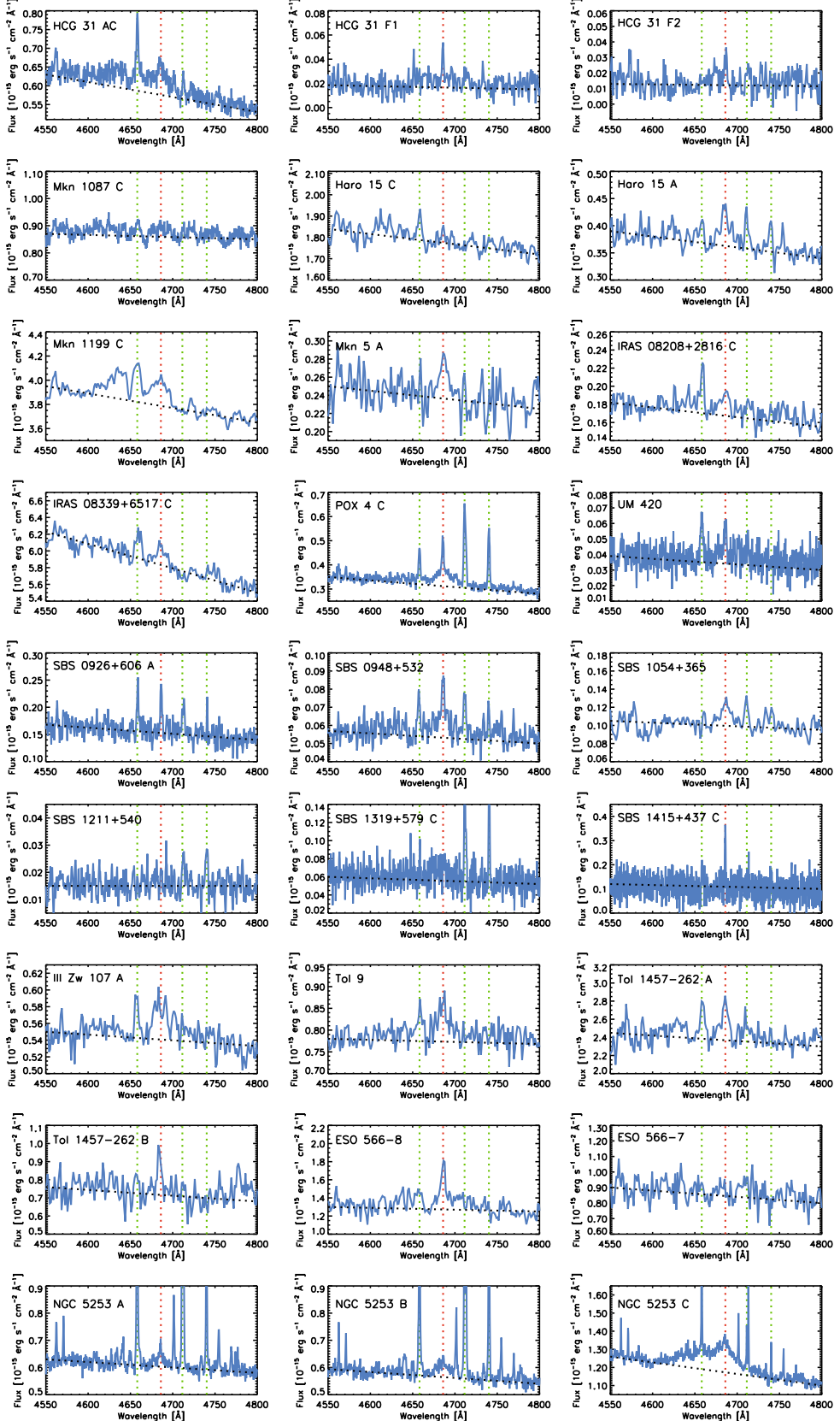


Fig. 36. Detail of the spectra of the main regions within our galaxy sample showing the zones around the blue WR bump. The red dotted line represents the position of the He II $\lambda 4686$ emission line, the blue dotted lines indicate the position of [Fe III] $\lambda 4658$ and [Ar IV] $\lambda\lambda 4711, 4740$ emission lines. The black dotted line represents the continuum level fitted by eye.

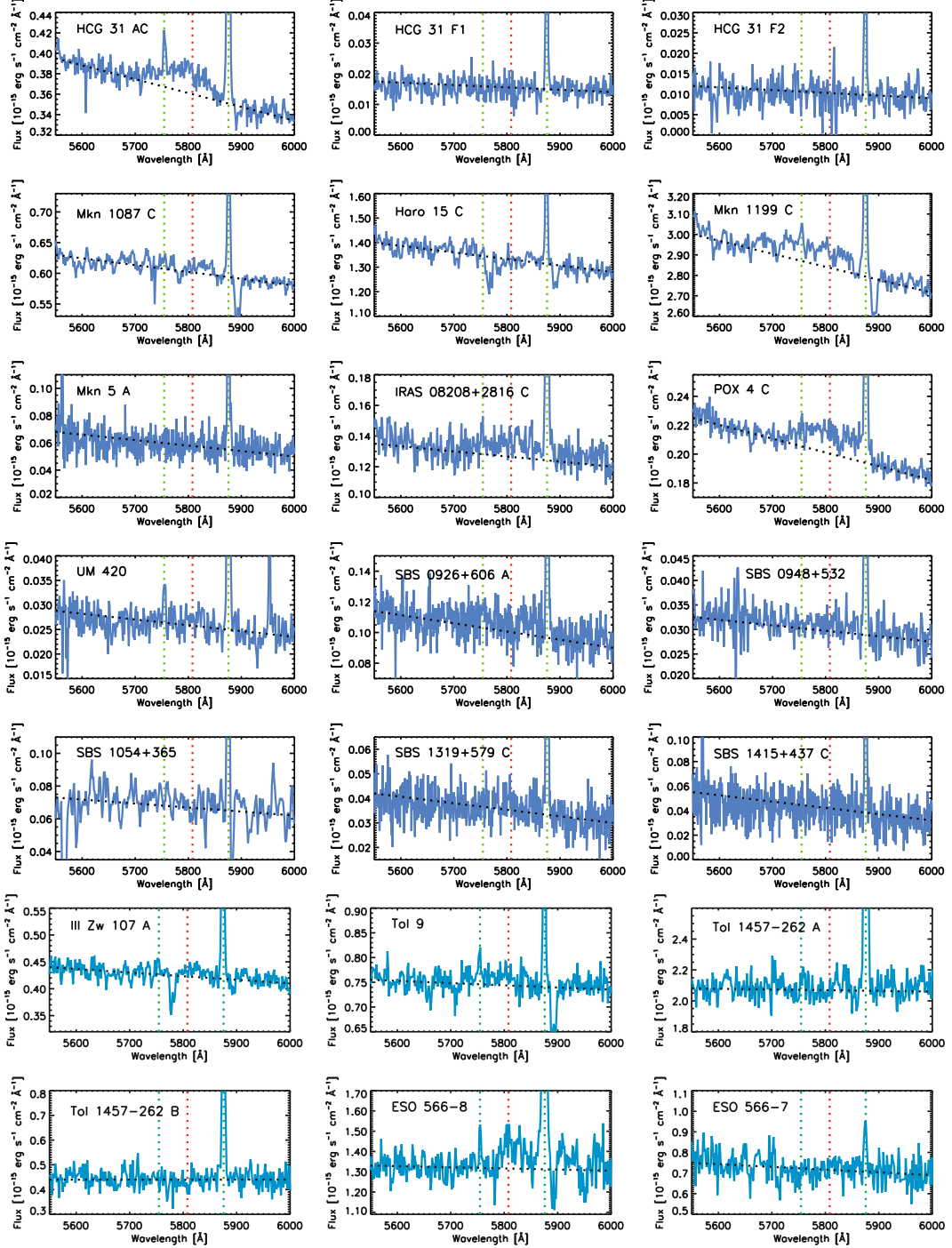


Fig. 37. Detail of the spectra of the main regions within our galaxy sample showing the zones around the red WR bump. The red dotted line represents the position of the C IV $\lambda 5808$ emission line, the blue dotted lines indicate the position of [N II] $\lambda 5755$ and He I $\lambda 5875$ emission lines. The black dotted line represents the continuum level fitted by eye. The red WR bump is clearly identified in HCG 31 AC and POX 4, detected Mkn 1199 and ESO 566-8 and it also seems to be observed in IRAS 08208+2816 and Tol 9. We do not have data for SBS 1211+540 and NGC 5253 in this spectral range.

estimate the metallicity of the ionized gas. We have estimated the oxygen abundance of many new regions within the galaxy sample and refined the chemical properties of some of them, outlining regions in HCG 31, Mkn 1087, Mkn 1199, III Zw 107, Tol 9, Tol 1457-262, and NGC 5253.

The derived physical and chemical properties were usually in agreement with previous observations reported in the literature. Table 2 compares our oxygen abundance determinations with

those previously reported in the literature. As we can see, the majority of the results agree well with previous estimations, but there are important differences in Mkn 1199, III Zw 107, Tol 9, and Tol 1457-262.

Including the data of the four systems analyzed in previous papers, a very useful database of objects with oxygen abundances between 7.58 and 8.75 in units of $12+\log(\text{O/H})$ is provided. In Papers IV and V, we will explore this database

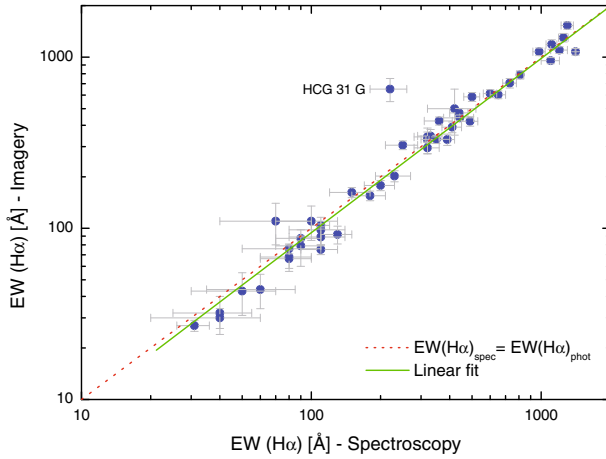


Fig. 38. Comparison between the H α equivalent widths derived from our H α images and those obtained from the analysis of the optical spectrum for every particular star-forming region analyzed in this work.

comparing their properties with other data derived from both our deep optical/NIR images and other multiwavelength observations available in the literature.

We have confirmed the detection of Wolf-Rayet features in the majority of the galaxies, as we should expect because our sample was extracted from the latest WR galaxy catalogue (Schaefer et al. 1999). We have reported the detection of broad WR features in 20 regions within 16 systems. Figure 36 shows the optical spectrum in the 4600–4750 Å range (blue WR bump) of all important objects; faint regions with very low S/N have been excluded. We have indicated the spatial localization of the massive stars in each system. WR features are sometimes found in different knots within the same galaxy (HCG 31, Haro 15, Tol 1457-262, NGC 5253). The He II $\lambda 4686$ emission line is unambiguously detected in 14 regions (HCG 31 AC and F1, Haro 15 A, Mkn 5, POX 4, UM 420, SBS 0926+606 A, SBS 0948+532, SBS 1415+437 C, Tol 1457-262 A and B, ESO 566-8 and NGC 5253 A and D), being particularly strong in POX 4. In only three objects previously listed as WR galaxies (Mkn 1087, SBS 1211+540 and ESO 566-7) do we not detect any feature that can be attributed to the presence of this sort of massive stars. We consider aperture effects and the exact positioning of the slit onto the WR-rich bursts to play a fundamental role in the detection of the WR features.

As expected, the red WR bump (the broad C III $\lambda 5696$ and C IV $\lambda 5808$ emission lines) is far more difficult to observe. Figure 37 shows the optical spectrum in the 5550–6000 Å range (red WR bump) of all important objects for which data in this spectral range is available. The broad C IV $\lambda 5808$ emission line is clearly identified in 2 galaxies (HCG 31 AC and POX 4), detected in 2 galaxies (Mkn 1199 and ESO 566-8), and it also seems to be observed in other 2 galaxies (IRAS 08208+2816 and Tol 9). However, we do not detect this feature in galaxies for which previous detections have been reported [Mkn 5, UM 420, SBS 0926+606, SBS 0948+532, SBS 1054+365 and SBS 1319+579A, Guseva et al. (2000)]. We will discuss this result in Paper III. A detailed quantitative analysis of the WR/(WR+O) and WC/WN ratios and a comparison with theoretical evolution models will also be performed in Paper III.

As we commented in Paper I, one of the most accurate methods for determining the age of the most recent star-forming burst is by means of the H α equivalent width since it decreases with time. Our spectroscopic observations provide an independent

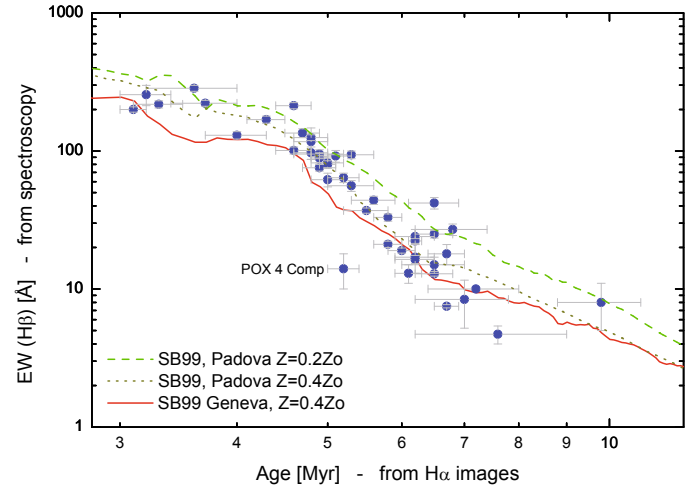


Fig. 39. H β equivalent width vs. age of the most recent star-forming burst diagram comparing the predictions given by the evolutionary synthesis models provided by STARBURST 99 (Leitherer et al. 1999). We include the $Z/Z_{\odot} = 0.4$ model originally included in STARBURST 99 using Geneva tracks and two new models with $Z/Z_{\odot} = 0.2$ and 0.4 than consider Padova tracks (Vázquez & Leitherer 2005). The age was computed from the $W(H\alpha)$ given by our images; $W(H\beta)$ was determined from our optical spectra.

estimation of $W(H\alpha)$ within each knot. We have checked the correspondence between the values that we obtained in our deep H α images (see Table 7 in Paper I) with those derived from the spectroscopic data. Figure 38 plots this correlation, showing excellent agreement between both kinds of data in almost all objects. Indeed, the linear fit to the data practically coincides with a $x = y$ function. Small divergences are found in very few objects, but they can be explained by the considerable differences in the relative sizes for which the photometric/spectroscopic values were extracted. The most evident case is member G in HCG 31, for which we only extracted the spectrum of a small knot at its NW, but the $W(H\alpha)$ value derived from the images considers the flux over all the galaxy, which has a global star-formation activity lower than that observed in the NW knot.

Figure 39 shows the comparison of our data with the theoretical predictions provided by the most recent release of the STARBURST 99 (Leitherer et al. 1999) models, which uses Padova tracks (Vázquez & Leitherer 2005). We assumed an instantaneous burst with a Salpeter IMF, a total mass of $10^6 M_{\odot}$, and a metallicity of $Z/Z_{\odot} = 0.2$ and 0.4 , the most common values according to the oxygen abundance of the majority of the knots. For comparison, we have also included the predictions of the original STARBURST 99 models, which use Geneva tracks, for $Z/Z_{\odot} = 0.4$. The ages of the last star-formation event are those estimated from the $W(H\alpha)$ determined from our deep images, while the H β equivalent widths are those directly measured from our spectra. Thus, both sets of data come from independent observations. As we can see, the agreement is excellent, and we are therefore quite confident in the determination of the age of the star-forming regions. As expected, the predictions given by the new models are more robust than those obtained from the old models. The only data point that does not follow the models is the dwarf companion object surrounding POX 4. However, as we explained in Paper I, the values of the $W(H\alpha)$ have been taken from images obtained by Méndez & Esteban (1999) and seem to be somewhat overestimated.

Although absorption features have only been detected in some objects, all of them contain an old stellar population in

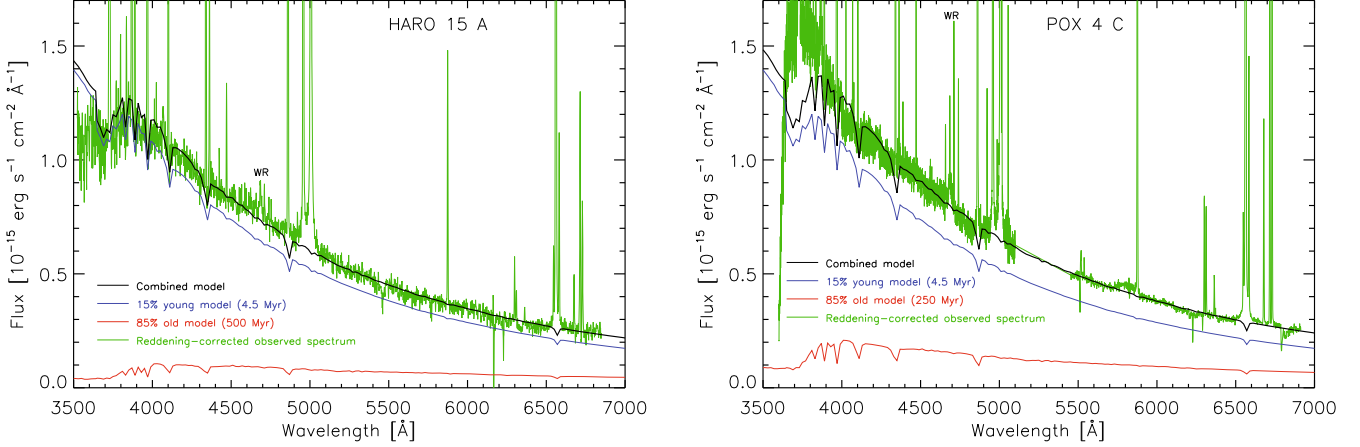


Fig. 40. Spectra of region A in Haro 15 (left) and the center of POX 4 (right) compared with synthetic continuum spectral energy distributions obtained using the PEGASE.2 (Fioc & Rocca-Volmerange 1997) code. The gray/green continuous line is the extinction-corrected spectrum, the upper continuous line corresponds to a model with an age of 4.5 Myr (young population model), whereas the lower continuous line is a 500 Myr (for Haro 15 A) or a 250 Myr (for POX 4 C) model (old population model). The shape of our observed dereddened spectra fit in both cases with a model with a contribution of 15% for the young population and 85% for the old population (continuous black line over the galaxy spectrum).

addition to the stars being formed within the bursts, as we commented in the analysis of the optical/NIR colours in Paper I. This is evident from the values of the W_{abs} derived from our spectra using the H I Balmer lines, which seems to increase with increasing metallicity. A very powerful way of constraining the ages of the stellar populations within a starburst galaxy is by analyzing its spectral energy distributions (SED), although we have a degeneracy problem between the interstellar extinction and the age of the old stellar population. In some objects, we have checked the results given by this method by considering our estimation of the reddening contribution derived from the Balmer decrement, as we did previously in our analysis of the stellar populations in IRAS 08339+6517 (López-Sánchez et al. 2006). We have used the PEGASE.2 code (Fioc & Rocca-Volmerange 1997) to produce a grid of theoretical SEDs of an instantaneous burst of star formation and ages between 0 and 10 Gyr, assuming a solar metallicity and a Salpeter IMF with lower and upper mass limits of $0.1 M_{\odot}$ and $120 M_{\odot}$. Although the grid include ionized gas emission, we have neglected this because its contribution to the continuum is almost irrelevant. In Fig. 40, we show the extinction-corrected spectra of the region A in Haro 15 (left) and the center of POX 4 (right) and two synthetic continuum spectral energy distributions assuming young (blue line) and old (red line) populations. We considered the ages derived from $W(\text{H}\alpha)$, which are representative of the young population ages (4.5 Myr in both cases) and the ages of the underlying component estimated from the optical/NIR colours (500 Myr in Haro 15, 250 Myr in POX 4). As expected, none of the individual synthetic spectra were a suitable fit to our observed SED. We then constructed a model that combines both young and old models. In both cases, the best-fit solutions are found when 15% of the 4.5 Myr model and 85% of the old model are considered. As we can see, this combined model is in very good agreement with the shape of our dereddened spectrum. We conclude that, although the star formation activity is very intense in these starbursts, an important underlying old stellar population is usually found in the galaxies, indicating that previous star-forming episodes have occurred and excluding the hypothesis that some of them are pristine dwarf galaxies.

Our study of the kinematics of the ionized gas and the morphology and environment included in this and previous

papers of our group has shown that 14 out of 20 of the analyzed galaxies show rather clear kinematical and/or morphological evidence of interactions or merging. The morphological evidence was presented and discussed in Paper I. The kinematical evidence presented here is diverse: presence of objects with velocities decoupled from the main rotation pattern (Mkn 1087, Haro 15), sinusoidal velocity patterns that suggest a merging process (HCG 31 AC, Mkn 1199, IRAS 08208+2816, SBS 0926+606 A, III Zw 107, Object 1 in Tol 1457-262), reversals in the velocity distribution (Tol 9, Arp 252), indications of tidal streaming (HCG 31, IRAS 08208+2816, SBS 1319+579, Tol 9), or the presence of TDG candidates (HCG 31 F1 and F2, Mkn 1087, IRAS 08339+6517, POX 4, Tol 1457-262). The interaction could be between a spiral – or, in general, a non-dwarf – galaxy (HCG 31, IRAS 08208+2816, Tol 1457-262, III Zw 107 and Arp 252), between spiral or non-dwarf galaxy and a dwarf one (Mkn 1087, Haro 15, Mkn 1199, IRAS 08339+6517, Tol 9), or between two dwarf galaxies (POX 4, SBS 0926+606, SBS 1319+579). In the case of NGC 5253, we observe a dwarf starburst galaxy that has experienced a possible interaction with a galaxy in the M 83 subgroup or with the spiral galaxy M 83 itself (López-Sánchez et al. 2008). These results reinforce the hypothesis that interaction with or between dwarf objects is an important mechanism for triggering the massive star formation in this kind of starburst galaxies. These neighboring interacting dwarf or low-luminosity objects are only detected when a systematic and detailed analysis of the morphology, environment, chemical composition, and kinematics of the objects are carried out.

Finally, our detailed spectroscopical analysis has provided us with clear evidence of chemical differences within the objects or of interacting objects of different metallicities. For example, Mkn 1087, Haro 15, and Mkn 1199 are clearly interacting with dwarf galaxies with lower O/H and N/O ratios. NGC 5253, IRAS 08208+2816, and Tol 1457-262 contain zones of different chemical composition. In the case of NGC 5253, this is produced by localized pollution of massive stars, but in the cases of IRAS 08208+2816 and Tol 1457-262 the different chemical compositions seem to be caused by the regions corresponding to different galaxies in interaction. Apart from NGC 5253, two more galaxies, IRAS 08208+2816 and UM 420, show a

localized high N/O, which could be a signature of contamination by WR winds.

Acknowledgements. Á.R. L.-S. thanks C. E. (his formal PhD supervisor) for all the help and very valuable explanations, talks and discussions along these years. He also acknowledges Jorge García-Rojas, Sergio Simón-Díaz and José Caballero for their help and friendship during his PhD, extending this acknowledgement to all people at Instituto de Astrofísica de Canarias (Spain). The authors thank Bärbel Koribalski (CSIRO/ATNF) for her help analyzing HIPASS data. Á.R. L.-S. deeply thanks to Universidad de La Laguna (Tenerife, Spain) for force him to translate his Ph.D. Thesis from English to Spanish; he had to translate it from Spanish to English to complete this publication. This was the main reason of the delay of the publication of this research, such as the majority of the results shown here were already included in the PhD dissertation (in Spanish) that the first author finished in 2006. Since then, only some minor changes have been done to complete this manuscript. Á.R. L.-S. also thanks to all the people at the CSIRO/Australia Telescope National Facility, especially to Bärbel Koribalski, for their support and friendship while translating his PhD. The authors are very grateful to A&A language editor, Claire Halliday, for her kind revision of the manuscript. This work has been partially funded by the Spanish Ministerio de Ciencia y Tecnología (MCyT) under project AYA2004-07466. This research has made use of the NASA/IPAC Extragalactic Database (NED) which is operated by the Jet Propulsion Laboratory, California Institute of Technology, under contract with the National Aeronautics and Space Administration. This research has made extensive use of the SAO/NASA Astrophysics Data System Bibliographic Services (ADS).

References

- Asplund, M., Grevesse, N., & Sauval, A. J. 2005, in Cosmic Abundances as Records of Stellar Evolution and Nucleosynthesis, ed. F. N. Bash, & T. G. Barnes (San Francisco: ASP), ASP Conf. Ser., 335, 25
- Barnes, D. G., Staveley-Smith, L., de Blok, W. J. G., et al. 2001, MNRAS, 322, 486
- Benjamin, R. A., Skillman, E. D., & Smits, D. P. 2002, ApJ, 569, 288
- Bettioni, D., Galletta, G., & García-Murillo, S. 2003, A&A, 405, 5
- Brinchmann, J., Kunth, D., & Durret, F. 2008, A&A, 485, 657
- Buckalew, B. A., Kobulnicky, H. A., & Dufour, R. J. 2005, ApJS, 157, 30
- Campbell, A. W., Terlevich, R., & Melnick, J. 1986, MNRAS, 223, 811
- Cannon, J. M., Skillman, E. D., Kunth, D., et al. 2004, ApJ, 608, 768
- Cardelli, J. A., Clayton, G. C., & Mathis J. S. 1989, ApJ, 345, 245
- Conti, P. S. 1976, MSRSL, 9, 193
- Conti, P. S. 1991, ApJ, 377, 115
- Contini, T. 1996, Liege International Astrophysical Colloquia 33: Wolf-Rayet stars in the framework of stellar evolution, Liege: Université de Liège, Institut d'Astrophysique, ed. J. M. Vreux, A. Detal, D. Fraipont-Caro, E. Gosset, & G. Rauw, 619
- Crowther, P. A. 2007, ARA&A, 45, 177
- Dahlem, M., Ehle, M., Ryder, S. D., Vlajić, M., & Haynes, R. F. 2005, A&A, 432, 475
- Davoust, E., & Contini, T. 2004, A&A, 416, 515
- Denicoló, G., Terlevich, R., & Terlevich, E. 2002, MNRAS, 330, 69
- Dopita, M. A., Kewley, L. J., Heisler, C. A., et al. 2000, ApJ, 542, 224
- Erb, D. K., Shapley, A. E., Steidel, C. C., et al. 2003, ApJ, 591, 101
- Esteban, C., Peimbert, M., García-Rojas, J., et al. 2004, MNRAS, 355, 229
- Fernandes, I. F. de Carvalho, R., Contini, T., et al. 2004, MNRAS, 355, 728
- Fioc, M., & Rocca-Volmerange, B. 1997, A&A, 326, 950
- French, H. B. 1980, ApJ, 240, 41
- Gallego, J., Zamorano, J., Rego, M., et al. 1997, ApJ, 475, 502
- García-Rojas, J., Esteban, C., Peimbert, M., et al. 2004, ApJS, 153, 501
- Garnett, D. R. 1992, AJ, 103, 1330
- Garnett, D. R. 2003, lectures on Cosmochemistry: The melting pot of the elements. XIII Canary Islands Winter School of Astrophysics, Puerto de la Cruz, Tenerife, Spain, November 19–30, 2001, ed. C. Esteban, R. J. García López, A. Herrero, & F. Sánchez, Cambridge contemporary astrophysics (Cambridge, UK: Cambridge University Press), 171
- Garnett, D. R., Kennicutt, R. C. Jr., Chu, Y.-H., et al. 1991, ApJ, 373, 458
- Gordon, D., & Gottesman, S. T. 1981, AJ, 86, 161
- Guseva, N., Izotov, Y. I., & Thuan, T. X. 2000, ApJ, 531, 776
- Guseva, N. G., Izotov, Y. I., Papaderos, P., et al. 2001, A&A, 378, 756
- Guseva, N. G., Papaderos, P., Izotov, Y. I., et al. 2003, A&A, 407, 105
- Hirashita, H., Inoue, A. K., Kamaya, H., et al. 2001, A&A, 366, 83
- Huang, J. H., Gu, Q. S., Ji, L., et al. 1999, ApJ, 513, 215
- Huchtmeier, W. K., Sage, L. J., & Henkel, C. 1995, A&A, 300, 675
- Huchtmeier, W. K., Krishna, G., & Petrosian, A. 2005, A&A, 434, 887
- Huchtmeier, W. K., Petrosian, A., Krishna, G., et al. 2007, A&A, 462, 919
- Hunter, D. A., & Gallagher, J. S. 1985, AJ, 90, 1457
- Izotov, Y. I., & Thuan, T. X. 1998, ApJ, 500, 188
- Izotov, Y. I., & Thuan, T. X. 1999, ApJ, 511, 639
- Izotov, Y. I., & Thuan, T. X. 2004, ApJ, 616, 768
- Izotov, Y. I., Guseva, N. G., Lipovetskii, V. A., Kniazev, A. Y., & Stepanian, J. A. 1991, A&A, 247, 303
- Izotov, Y. I., Thuan, T. X., & Lipovetski 1994, ApJ, 435, 647
- Izotov, Y. I., Thuan, T. X., & Lipovetski, V. A. 1997, ApJS, 108, 1
- Kauffmann, G., & White, S. D. M. 1993, MNRAS, 261, 921
- Kewley, L. J., Dopita, M. A., Sutherland, R. S., Heisler, C. A., & Trevena, J. 2001, ApJS, 556, 121
- Kobulnicky, H. A., & Skillman, E. D. 1996, ApJ, 471, 211
- Kobulnicky, H. A., & Skillman, E. D. 2008, AJ, 135, 527
- Kobulnicky, H. A., Skillman, E. D., Roy, J.-R., Walsh, J. R., & Rosa, M. R. 1997, ApJ, 277, 679
- Kong, X., Cheng, F. Z., Weiss, A., et al. 2002, A&A, 396, 503
- Koribalski, B. S. 2008, proceedings of Galaxies in the Local Volume conference (Springer), 41
- Kovo, O., & Contini, T. 1999, in Wolf-Rayet Phenomena in Massive Stars and Starburst Galaxies. Proceedings of the 193rd symposium of the International Astronomical Union held in Puerto Vallarta, Mexico, 3–7 November 1998, ed. Karel, A. van der Hucht, G. Koenigsberger, & Philippe, R. J. Eenens, San Francisco, Calif.: ASP, 604
- Kniazev, A. Y., Pustilnik, S. A., Grebel, E. K., Lee, H., & Pramsku, A. G. 2004, ApJS, 153, 429
- Kunth, D., & Joubert, M. 1985, A&A, 142, 411
- Kunth, D., & Schild, H. 1986, A&A, 169, 71
- Lauberts, A., & Valentijn, E. A. 1989, The surface photometry catalogue of the ESO-Uppsala galaxies, Garching: European Southern Observatory (ESO)
- Lee, J. C., Salzer, J. J., & Melbourne, J. 2004, ApJ, 616, 752
- Leitherer, C., Schaerer, D., Goldader, J. D., et al. 1999, ApJS, 123, 3 (STARBURST 99)
- López-Sánchez, Á. R. 2006, Ph.D. Thesis, Universidad de La Laguna (Tenerife, Spain)
- López-Sánchez, Á. R., Esteban, C., & Rodríguez, M. 2004a, ApJS, 153, 243
- López-Sánchez, Á. R., Esteban, C., & Rodríguez, M. 2004b, A&A 428, 445
- López-Sánchez, Á. R., Esteban, C., & García-Rojas, J. 2006, A&A, 449, 997
- López-Sánchez, Á. R., Esteban, C., García-Rojas, J., Peimbert, M., & Rodríguez, M. 2007, ApJ, 656, 168
- López-Sánchez, Á. R., Koribalski, B., Esteban, C., & García-Rojas, J. 2008, proceedings of Galaxies in the Local Volume (Springer), 53
- López-Sánchez, Á. R., & Esteban, C. 2008, A&A, 491, 131 (Paper I)
- López-Sánchez, Á. R., & Esteban, C. 2010, A&A, submitted (Paper III)
- López-Sánchez, Á. R., Koribalski, B. S., et al. 2010, MNRAS, submitted
- Maeder, A. 1990, A&AS, 84, 139
- Maeder, A. 1991, A&A, 242, 93
- Masegosa, M., Moles, M., & del Olmo, A. 1991, A&A, 244, 273
- Masegosa, M., Moles, M., & Campos-Aguilar, A. 1994, ApJ, 420, 576
- Massey, P., Strobel, K., Barnes, J. V., et al. 1988, ApJ, 328, 315
- Mazzarrella, J. M., & Boronson, T. A. 1993, ApJS, 85, 27
- Mazzarella, J. M., Bothun, G. D., & Boronson, T. A. 1991, AJ, 101, 2034
- Melbourne, J., & Salzer, J. J. 2002, AJ, 123, 2302
- Melbourne, J., Phillips, A., Salzer, J. J., Gronwall, C., & Sarajedini, V. L. 2004, AJ, 127, 686
- Méndez, D. I., & Esteban, C. 1997, ApJ, 488, 652
- Méndez, D. I., & Esteban, C. 1999, AJ 118, 2733
- Meynet, G., & Maeder, A. 2005, A&A, 429, 581
- Paturel, G., Theureau, G., Bottinelli, L., et al. 2003, A&A, 412, 57
- Peimbert, M., & Costero, R. 1969, Bol. Obs. Tonantzintla y Tacubaya, 5, 3
- Penston, M. V., Fosbury, R. A. E., Ward, M. J., et al. 1977, MNRAS, 180, 19
- Peña, M., Ruiz, M. T., & Maza, J. 1991, A&A, 251, 417
- Pérez-Montero, E., & Díaz, A. I. 2003, MNRAS, 346, 105
- Perryman, M. A. C., Longair, M. S., Allington-Smith, J. R., et al. 1982, MNRAS, 201, 957
- Pettini, M., & Pagel, B. E. J. 2004, MNRAS, 348, 59
- Pilyugin, L. S. 2001a, A&A, 369, 594
- Pilyugin, L. S. 2001b, A&A, 374, 412
- Pindao, M. 1999, in Wolf-Rayet Phenomena in Massive Stars and Starburst Galaxies, IAU Symp., 193, 614
- Pindao, M., Schaerer, D., González-Delgado, R. M., et al. 2002, A&A, 394, 443
- Piovan, L., Tantalo, R., & Chiosi, C. 2006, MNRAS, 366, 923
- Pustilnik, S. A., Martin, J.-M., Huchtmeier, W. K., et al. 2002, A&A, 389, 405
- Pustilnik, S., Kniazev, A., Pramskij, A., et al. 2004, A&A, 419, 469
- Quinet, P. 1996, A&AS, 116, 573
- Richer, M. G., Georgiev, L., Rosado, M., et al. 2003, A&A, 397, 99
- Rodríguez, M., & Rubin, R. H. 2005, ApJ, 626, 900
- Salzer, J. J., Rosenberg, J. L., Weisstein, E. W., Mazzarella, J. M., & Bothun, G. D. 2002, AJ, 124, 191
- Sargent, W. L. W. 1970, ApJ, 160, 405

- Schaerer, D., Contini, T., & Pindao, M. 1999, A&AS, 136, 35
 Schaerer, D., Guseva, N. G., Izotov, Yu. I., et al. 2000, A&A, 362, 53
 Schlegel, D. J., Finkbeiner, D. P., & Davis, M. 1998, ApJ, 500, 525
 Shaw, R. A., & Dufour, R. J. 1995, PASP, 107, 896
 Shi, F., Kong, X., Li, C., et al. 2005, A&A, 437, 849
 Skillman, E. D., Côté, S., & Miller, B. W. 2003, AJ, 125, 593
 Smith, L. F., Shara, M. M., & Moffat, A. F. J. 1996, MNRAS, 281, 163
 Springel, V., White, S. D. M., Jenkins, A., et al. 2005, Nature, 435, 629
 Stasińska, G. 1978, A&A, 66, 257
 Storey, P. J., & Hummer, D. G. 1995, MNRAS, 272, 41
 Terlevich, R., Melnick, J., Masegosa, J., Moles, M., & Copetti, M. V. F. 1991, A&AS, 91, 285
 Thuan, T. X., & Martin, G. E. 1981, ApJ, 247, 823
 Thuan, T. X., Izotov, Y. I., & Lipovetsky, V. A. 1995, ApJ, 445, 108
 Thuan, T. X., Izotov Y. I., & Foltz, C. B. 1999a, ApJ, 525, 105
 Thuan, T. X., Lipovetski, V. A., Martin, J.-M., et al. 1999b, A&ASS, 139, 1
 Vacca, W. D., & Conti, P. S. 1992, ApJ, 401, 543
 Vaceli, M. S., Viegas, S. M., Gruenwald, R., et al. 1997, AJ, 114, 1345
 van Zee, L., Salzer, J. J., & Haynes, M. P. 1998, ApJ, 497, 1
 Vázquez, G. A., & Leitherer, C. 2005, ApJ, 621, 695
 Veilleux, S., & Osterbrock, D. E. 1987, ApJS, 63 295
 Westera, P., Cuisinier, F., Telles, E., et al. 2004, A&A, 423, 133
 Winkler, H. 1988, MNRAS, 234, 703
 Woosley S. E., & Weaver, T. A. 1995, ApJS, 101, 181
 Woosley, S. E., & Bloom, J. S. 2006, ARA&A, 44, 507
 Zasov, A. V., Kniazev, A. Y., Pustilnik, S. A., et al. 2000, A&AS, 144, 429
 Zhang, H. L. 1996, A&AS, 119, 523
 Zhang, W., Kong, X., Li, C., Zhou, H.-Y., & Cheng, F.-Z. 2007, ApJ, 655, 851

Table 1. Journal of the intermediate-resolution long-slit spectroscopy observations, carried out using the 2.5 m INT, 2.56 m NOT and 4.2 m WHT telescopes and with the instrumentation as explained in text.

Galaxy	Tel.	Date	Exp. time [s]	Spatial R. ["/pix]	Grism	PA [°]	Spectral R. [Å]	$\Delta\lambda$ [Å]	sec z (a)
Haro 15	INT	99/12/27	3 × 1200	0.40	R400V	41	3.5	3500–7700	1.67
	INT	99/12/27	3 × 1200	0.40	R400V	117	3.5	3500–7700	1.40
Mkn 1199	INT	99/12/28	3 × 1200	0.40	R400V	32	3.5	3500–7700	1.02
	INT	99/12/28	3 × 1200	0.40	R400V	53	3.5	3500–7700	1.00
Mkn 5	WHT	02/12/27	3 × 700	0.20	R1200	90	0.86	4300–5100	1.90
	WHT	02/12/27	3 × 700	0.20	R136R	90	2.6	5700–7800	1.90
	INT	99/12/29	3 × 1200	0.40	R400V	0	3.5	3500–7700	1.54
	INT	99/12/29	3 × 1200	0.40	R400V	349	3.5	3500–7700	1.47
POX 4	WHT	00/12/30	3 × 1800	0.20	R600B	25	1.8	3650–5100	1.60
	WHT	00/12/30	3 × 1800	0.36	R136R	25	2.6	5300–6650	1.60
UM 420	WHT	00/12/30	4 × 1800	0.20	R600B	90	1.8	3650–5100	1.14
	WHT	00/12/30	4 × 1800	0.36	R136R	90	2.6	5300–6650	1.14
	INT	99/12/28	3 × 1200	0.40	R400V	90	3.5	3500–7700	1.23
IRAS 08208+2816	INT	99/12/28	3 × 1200	0.40	R400V	10	3.5	3500–7700	1.11
	INT	99/12/28	3 × 1200	0.40	R400V	345	3.5	3500–7700	1.01
	INT	99/12/28	3 × 1200	0.40	R400V	355	3.5	3500–7700	1.32
SBS 0926+606A	WHT	02/12/27	3 × 600	0.20	R1200	27	0.86	4300–5100	1.18
	WHT	02/12/27	3 × 600	0.20	R136R	27	2.6	5700–7800	1.18
SBS 0948+532	WHT	00/12/31	3 × 1800	0.20	R600B	114	0.86	3650–5100	1.10
	WHT	00/12/31	3 × 1800	0.36	R136R	114	2.6	5300–6650	1.10
SBS 1054+365	INT	99/12/29	3 × 1200	0.40	R400V	55	3.5	3500–7700	1.15
SBS 1211+540	WHT	00/12/31	3 × 1800	0.20	R600B	138	1.8	3650–5100	1.12
	WHT	00/12/31	3 × 1800	0.36	R136R	138	2.6	5300–6650	1.12
SBS 1319+579	WHT	02/12/27	3 × 600	0.20	R1200	39	0.86	4300–5100	1.48
	WHT	02/12/27	3 × 600	0.20	R136R	39	2.6	5700–7800	1.48
SBS 1415+437	WHT	02/12/27	3 × 600	0.20	R1200	20	0.86	4300–5100	1.54
	WHT	02/12/27	3 × 600	0.20	R136R	20	2.6	5300–6650	1.54
III Zw 107	INT	99/12/28	3 × 1200	0.40	R400V	0	3.5	3500–7700	1.18
Tol 9	INT	99/12/27	4 × 1200	0.40	R400V	49	3.5	3500–7700	1.90
	NOT	06/04/28	4 × 1200	0.19	g14	109	7.0	3300–6100	1.85
	NOT	06/04/27	3 × 900	0.19	g8	109	6.5	5800–8300	1.92
Tol 1457-262a	NOT	05/04/04	3 × 900	0.19	g14	155	7.0	3300–6100	1.92
	NOT	05/04/04	3 × 900	0.19	g8	155	6.5	5800–8300	1.75
Arp 252	NOT	05/04/04	3 × 900	0.19	g14	342	7.0	3300–6100	1.67
	NOT	05/04/04	3 × 900	0.19	g8	342	6.5	5800–8300	1.56

^a Sec z represents the average airmass in which the observations were made.

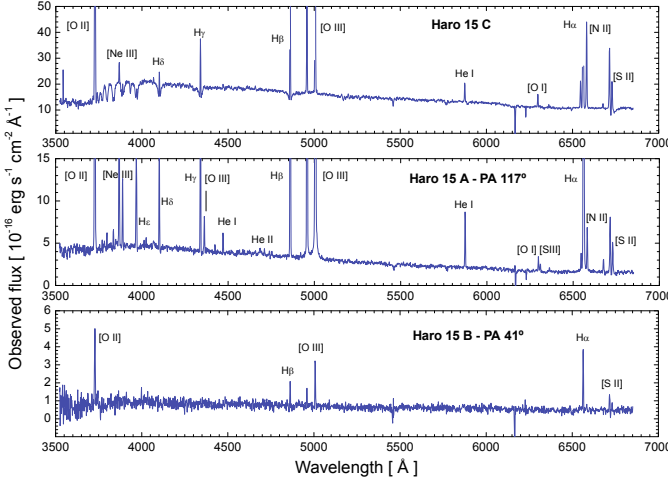


Fig. 1. IDS INT spectra for regions C, A, and B of Haro 15. Fluxes are not corrected for reddening. The most important emission lines have been labeled. See Fig. 3 in Paper I for the identification of the regions.

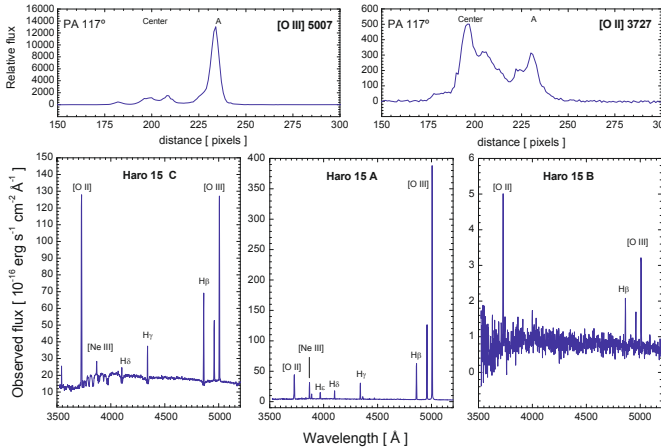


Fig. 2. Lower panels: zoom of the spectra of regions C (center), A, and B of Haro 15 (bottom). Fluxes are not corrected for reddening. Upper panels: spatial distribution of the relative flux of [O II] $\lambda 3727$ (upper, right) and [O III] $\lambda 5007$ (upper, left) emission lines along the slit of PA 117° .

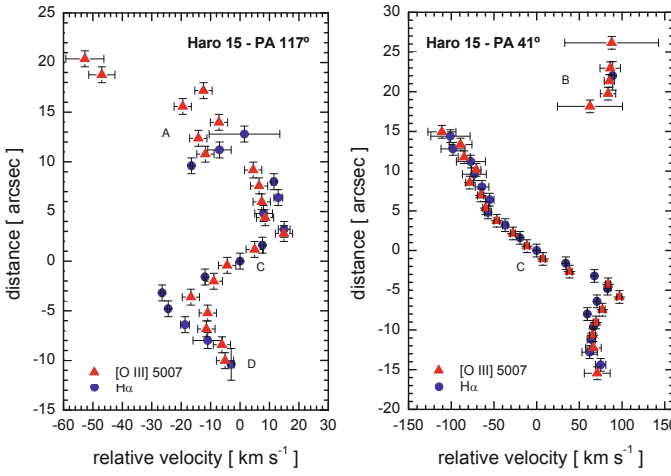


Fig. 3. Position-velocity diagrams for the two slit positions observed in Haro 15. Both the H α and the [O III] $\lambda 5007$ profiles have been analyzed. East is at the top in both diagrams. See Fig. 3 in Paper I for the identification of the regions.

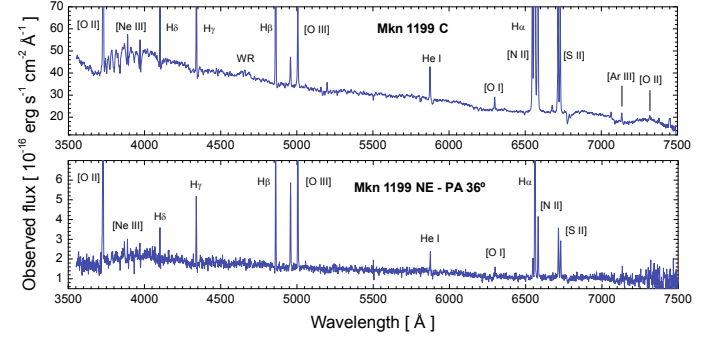


Fig. 4. IDS INT spectra for the center of Mkn 1199 and the dwarf companion galaxy at its NE. Fluxes are not corrected for reddening. The most important emission lines have been labeled. See Fig. 5 in Paper I for the identification of the regions.

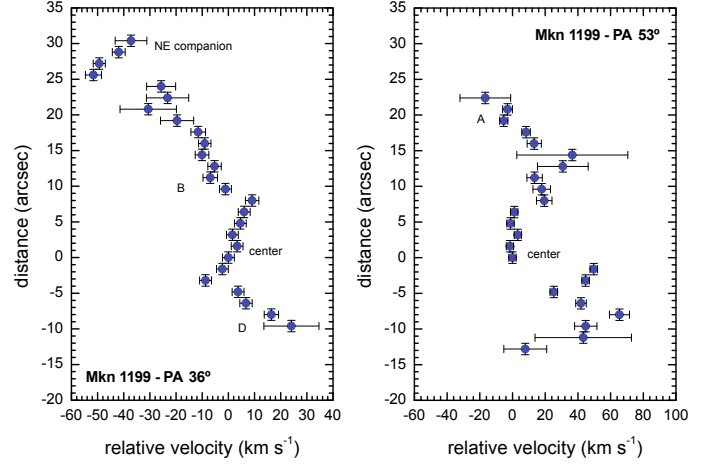


Fig. 6. Position-velocity diagrams for the two slit positions observed in Mkn 1199 using the H α profiles. NE is up in both diagrams. See Fig. 5 in Paper I for the identification of the regions.

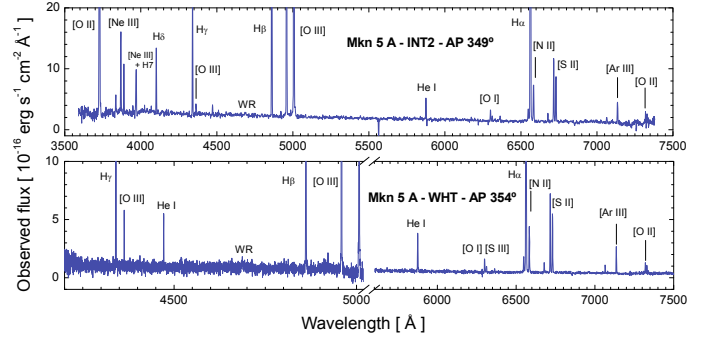


Fig. 7. Spectra for the region A of Mkn 5 obtained using IDS at the INT (PA 349°) and ISIS at the WHT (PA 354°). Fluxes are not corrected for reddening. The most important emission lines have been labeled. See Fig. 7 in Paper I for the identification of the regions.

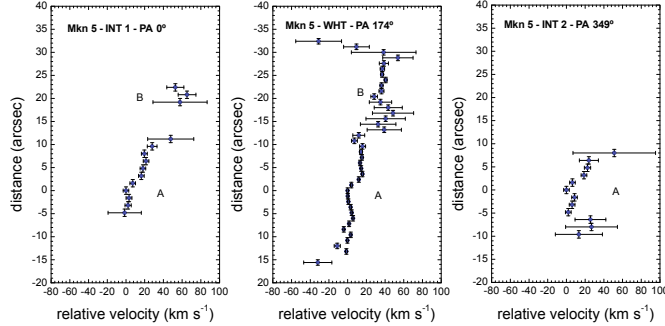


Fig. 8. Position-velocity diagrams for the slit positions observed in Mkn 5 using the $[\text{O III}] \lambda 5007$ profile. N is up in all diagrams. See Fig. 7 in Paper I for the identification of the regions.

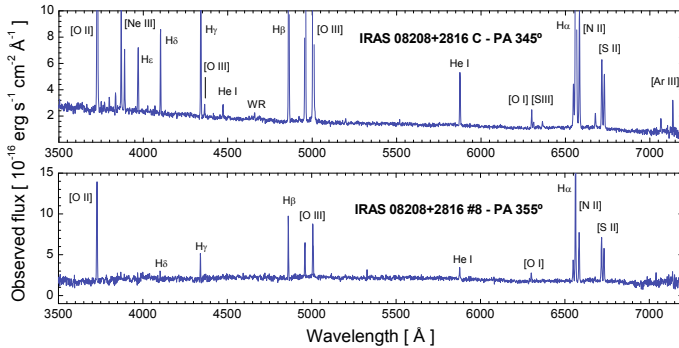


Fig. 9. IDS INT spectra for the center of IRAS 08208+2816 and knot #8. Fluxes are not corrected for reddening. The most important emission lines have been labeled. See Fig. 9 in Paper I for the identification of the regions.

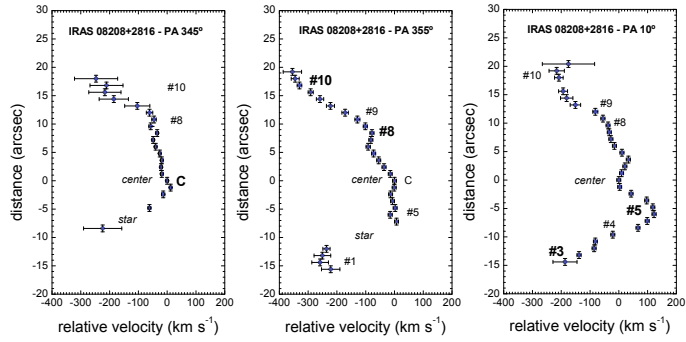


Fig. 10. Position-velocity diagrams for the three slit positions observed of IRAS 08208+2816 using the $[\text{O III}] \lambda 5007$ profile. N is up in all diagrams. We have included the position of the regions (see Fig. 9 in Paper I for their identification), emphasizing those analyzed by spectroscopy. Notice that the lacking of data at the southern edge of the southern tail in the diagrams with PA 345° and 355° is because of the contamination by a bright star.

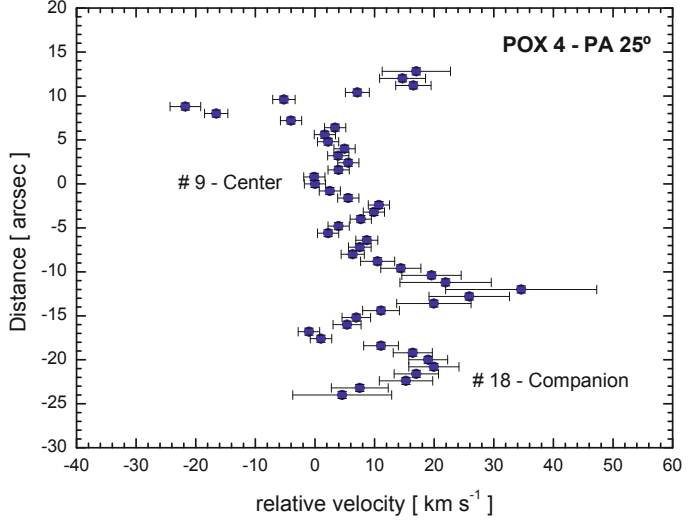


Fig. 12. Position-velocity diagram for the slit position observed in POX 4 using the $[\text{O III}] \lambda 5007$ profile. NE is up. See Fig. 11 in Paper I for the identification of the regions.

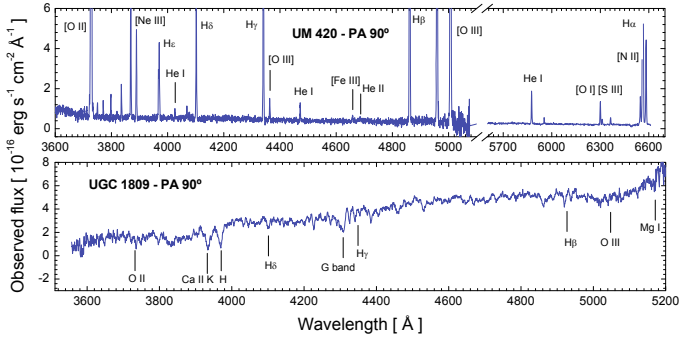


Fig. 13. ISIS 4.2 m WHT spectrum for the center of UM 420 (top) and the galaxy UGC 1809 (bottom). Fluxes are not corrected for reddening. The most important emission lines have been labeled.

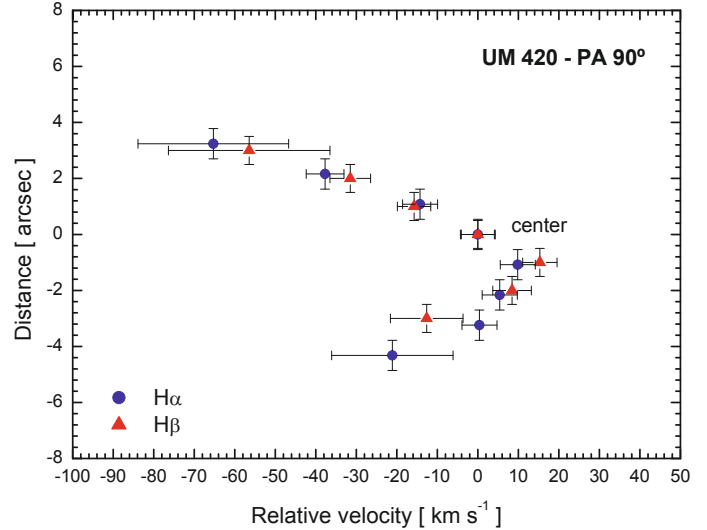


Fig. 15. Position-velocity diagram for the slit position observed in UM 420 using both the $\text{H}\alpha$ and $\text{H}\beta$ profiles. W is up.

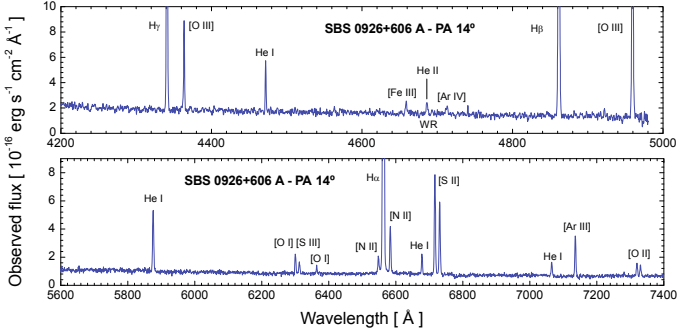


Fig. 16. ISIS 4.2 m WHT spectrum for SBS 0926+606 A. Fluxes are not corrected for reddening. The most important emission lines have been labeled. See Fig. 15 in Paper I for the identification of this region.

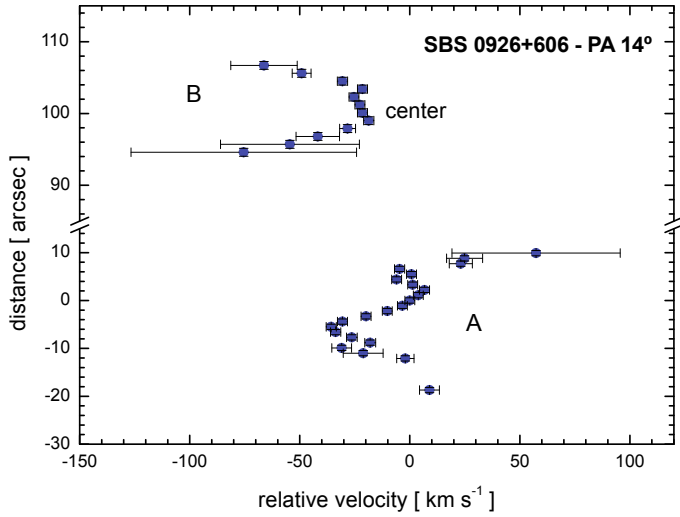


Fig. 17. Position-velocity diagram for the slit position with PA 14° observed in SBS 0926+606 using the H α profile. Notice that the y-axis is broken. NE is up. See Fig. 15 in Paper I for the identification of the regions.

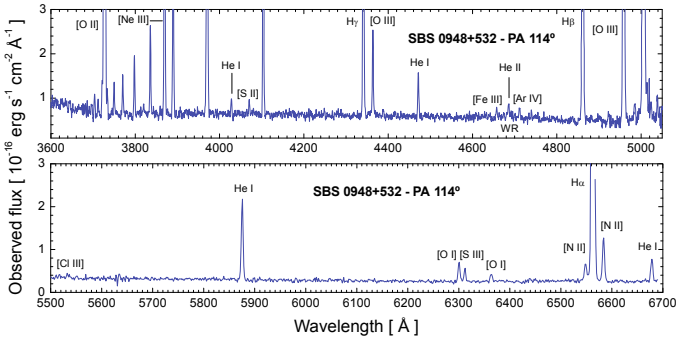


Fig. 18. ISIS 4.2 m WHT spectrum for SBS 0948+532 using a slit with PA 114°. Fluxes are not corrected for reddening. The most important emission lines have been labeled.

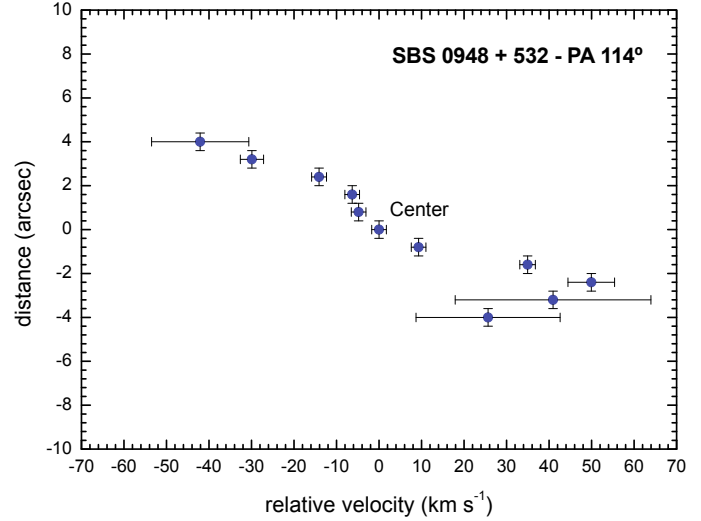


Fig. 19. Position-velocity diagram for the slit position with PA 114° observed in SBS 0948+532 using the [O III] λ 5007 profile. NW is up (see Fig. 17 in Paper I).

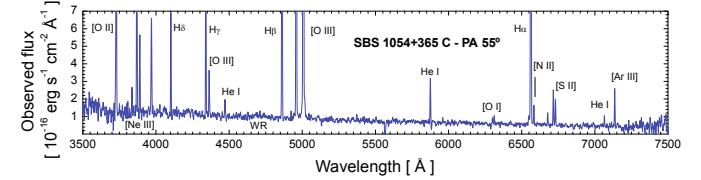


Fig. 20. IDS 2.5 m INT spectrum for SBS 1054+364 using a slit with PA 55°. Fluxes are not corrected for reddening. The most important emission lines have been labeled. See Fig. 19 in Paper I for identification of the region.

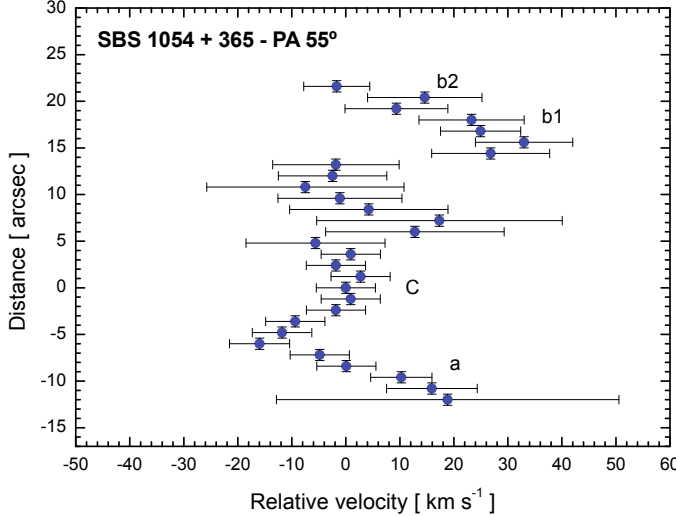


Fig. 21. Position-velocity diagram for the slit position observed in SBS 1054+365 using the H α profile. NE is up. See Fig. 19 in Paper I for identification of the regions.

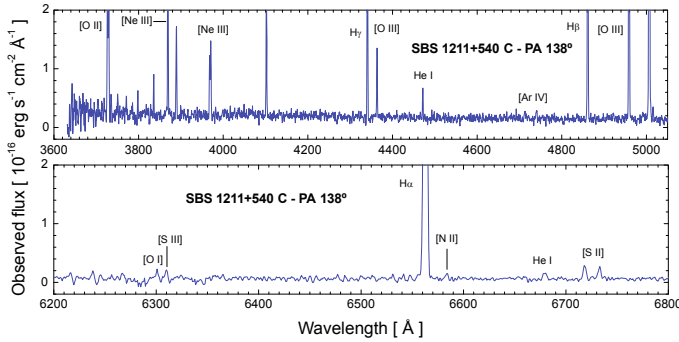


Fig. 22. ISIS 4.2 m WHT spectrum for SBS 1211+540 using a slit with PA 138°. Fluxes are not corrected for reddening. The most important emission lines have been labeled. See Fig. 21 in Paper I for identification of the region.

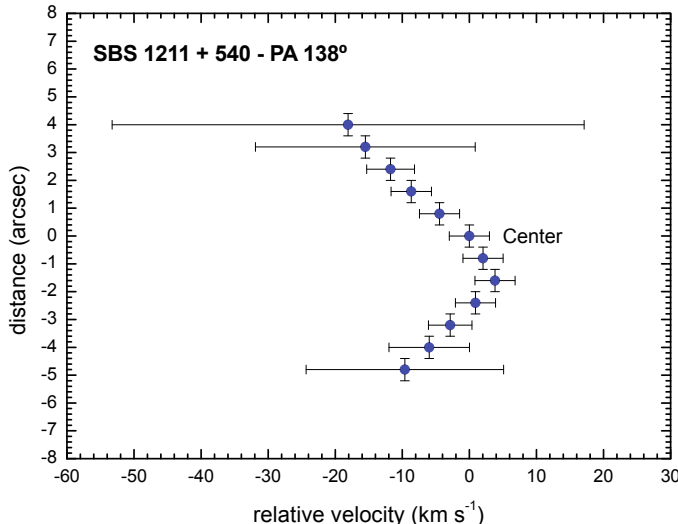


Fig. 23. Position-velocity diagram for the slit position with PA 138° observed in SBS 1211+532 using the [O III] $\lambda 5007$ profile. NW is up. See Fig. 21 in Paper I for identification of the regions.

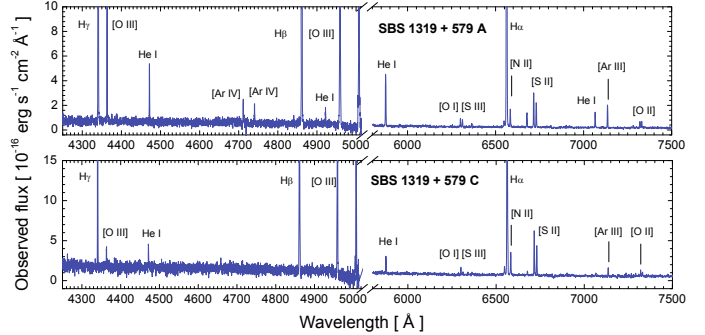


Fig. 24. ISIS 4.2 m WHT spectrum for regions A (top) and C (bottom) of SBS 1319+579 obtained with a slit with PA 49°. Fluxes are not corrected for reddening. The most important emission lines have been labeled. See Fig. 23 in Paper I for identification of the regions.

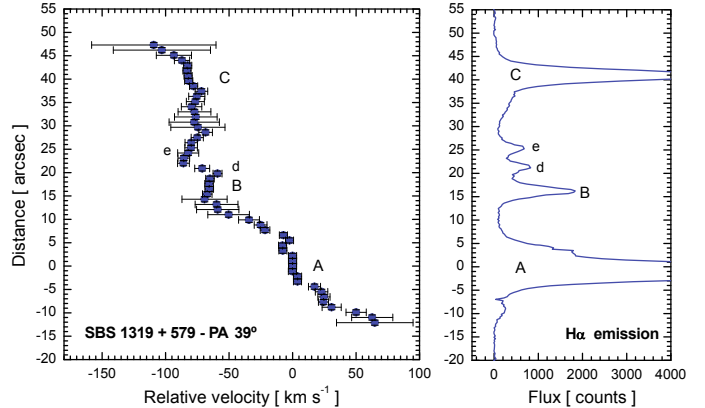


Fig. 25. Position-velocity diagram for the slit position observed in SBS 1319+579 using the H α profile. The relative intensity of the H α emission along the spatial direction is also shown, identifying all observed regions. NE is up. See Fig. 23 in Paper I for identification of the regions.

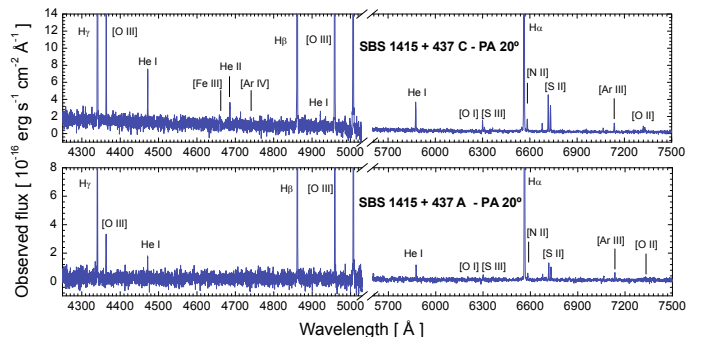


Fig. 26. ISIS 4.2 m WHT spectrum for regions C (top) and A (bottom) of SBS 1415+437 using a slit with PA 20°. Fluxes are not corrected for reddening. The most important emission lines have been labeled. See Fig. 25 in Paper I for identification of the regions.

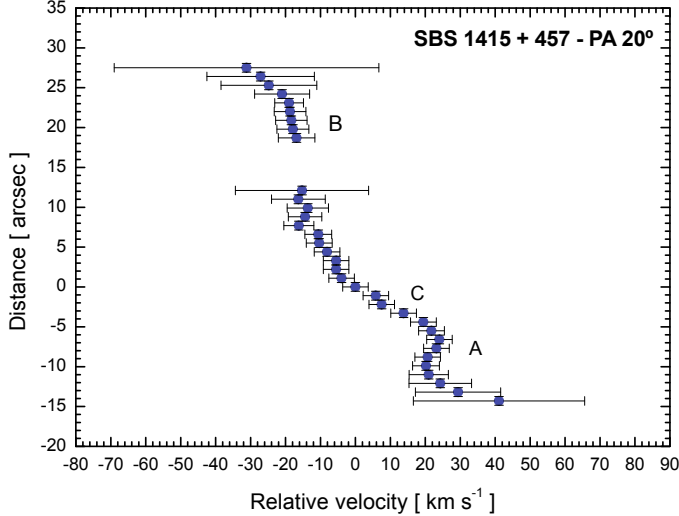


Fig. 27. Position-velocity diagram for the slit position with PA 20° observed in SBS 1415+437 using the $H\alpha$ profile. NE is up. See Fig. 25 in Paper I for identification of the regions.

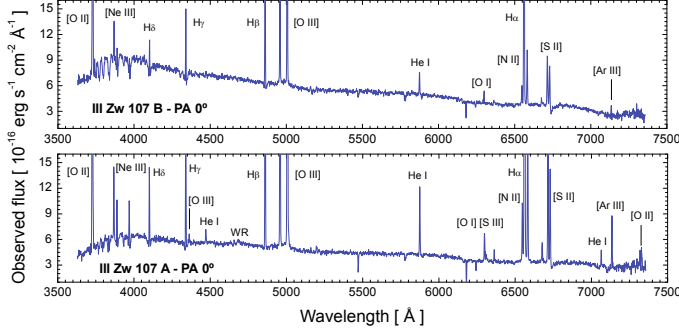


Fig. 28. IDS INT spectra for the regions A (bottom) and B (top) of IRAS III Zw 107. Fluxes are not corrected for reddening. The most important emission lines have been labeled. See Fig. 27 in Paper I for identification of the regions.

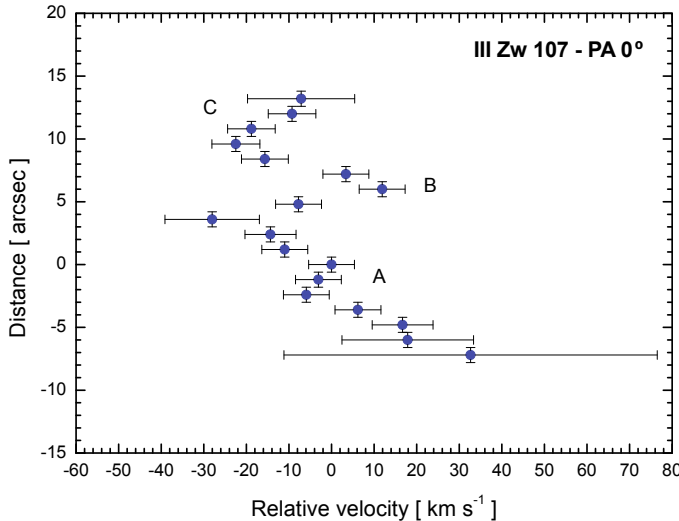


Fig. 29. Position-velocity diagram for the slit position with PA 0° observed in III Zw 107 using the $H\alpha$ profile. N is up. See Fig. 27 in Paper I for identification of the regions.

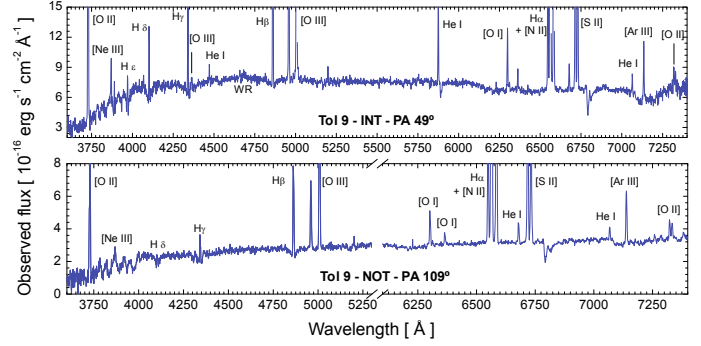


Fig. 30. IDS INT spectrum (bottom) using a slit with PA 49° and ALFOSC 2.56 m NOT spectrum (top) using a slit of PA 109° of Tol 9. Fluxes are not been corrected for reddening. The most important emission lines have been labeled. See Figs. 29 and 30 in Paper I for identification of the regions.

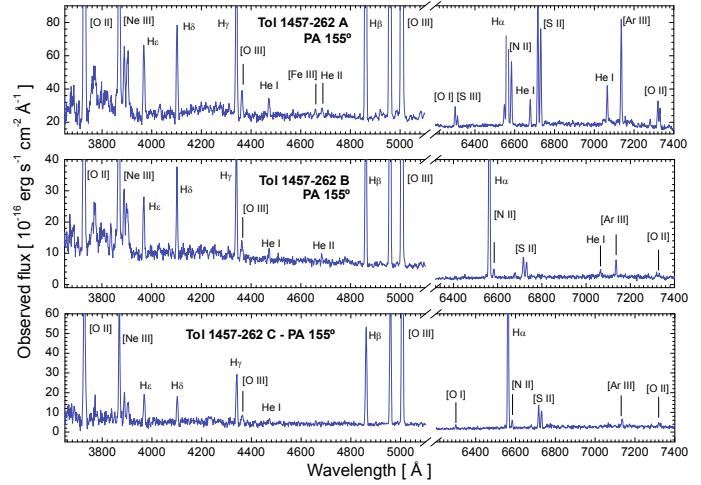


Fig. 32. ALFOSC 2.56 m NOT spectra of the regions analyzed in Tol 1457-262. Fluxes are not corrected for reddening. The most important emission lines have been labeled. See Fig. 31 in Paper I for identification of the regions.

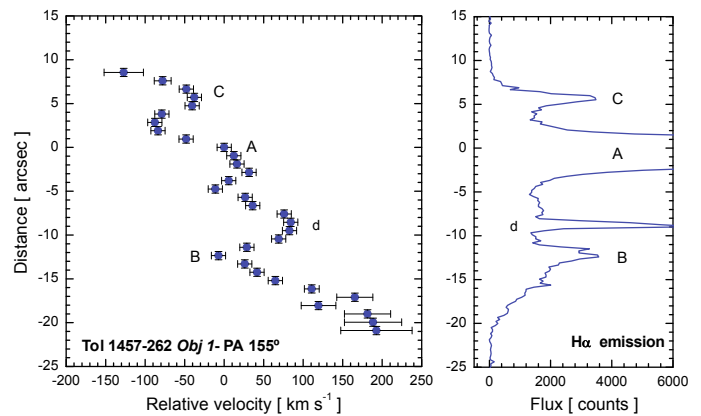


Fig. 33. Position-velocity diagram for the slit position observed in Object 1 of Tol 1457-262 using the $H\alpha$ profile. The relative intensity of the $H\alpha$ emission along the spatial direction is also shown, identifying all observed regions. NW is up. See Fig. 31 in Paper I for identification of the regions.

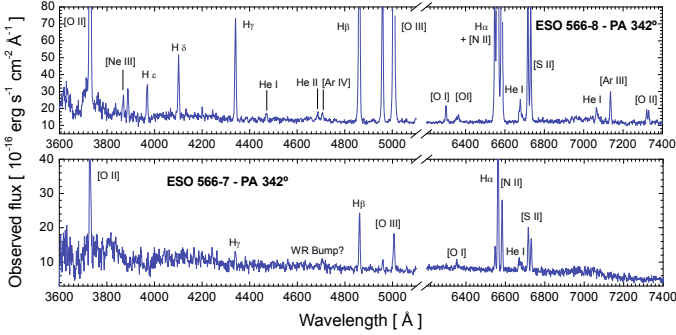


Fig. 34. ALFOSC 2.56 m NOT spectra for the galaxy pair ESO 566-8 (top) and ESO 566-7 (bottom) that constitute Arp 256. Fluxes are not been corrected for reddening. The most important emission lines have been labeled. See Fig. 34 in Paper I for identification of the galaxies.

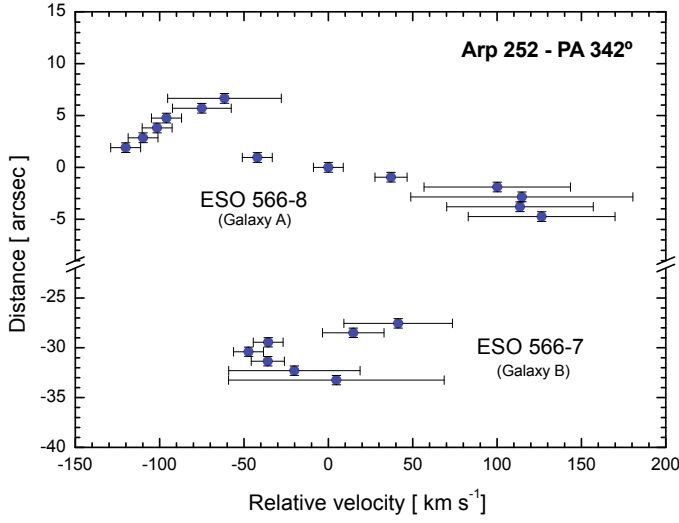


Fig. 35. Position-velocity diagram for the slit position observed in Arp 252 using the H α profile. Notice that the y -axis is broken in two parts. N is up. See Fig. 34 in Paper I for identification of the galaxies.

Appendix A: Tables

Table A.1. Dereddened line intensity ratios with respect to $I(\text{H}\beta) = 100$ for knots analyzed in Haro 15.

Line	$f(\lambda)$	C	A	B	D
3705.04 He I	0.260	1.05:
3728.00 [O II]	0.256	294 ± 19	113 ± 21	402 ± 106	336 ± 46
3770.63 H I	0.249	0.68:	1.69 ± 0.52
3797.90 H I	0.244	0.33:	3.10 ± 1.00
3835.39 H I	0.237	1.69:	4.59 ± 0.99
3868.75 [Ne III]	0.230	14.2 ± 2.8	48.6 ± 8.4	...	39.4:
3889.05 H I	0.226	7.6 ± 3.0	15.5 ± 2.8
3967.46 [Ne III]	0.210	...	29.6 ± 4.8
3970.07 H I	0.210	19.6 ± 1.7
4026.21 He I	0.198	...	1.05:
4068.60 [S II]	0.189	2.69:
4101.74 H I	0.182	28.1 ± 2.7	26.1 ± 3.5	...	26.1 ± 7.0
4340.47 H I	0.127	46.2 ± 3.5	47.0 ± 4.8	...	46.7 ± 9.9
4363.21 [O III]	0.121	1.22:	8.59 ± 0.87	...	3.9:
4471.48 He I	0.095	3.56:	4.17 ± 0.68
4658.10 [Fe III]	0.050	1.75:	0.90:
4686.00 He II	0.043	0.49:	1.65 ± 0.42
4711.37 [Ar IV]	0.037	...	1.10:
4740.16 [Ar IV]	0.030	...	0.73:
4754.83 [Fe III]	0.026	...	0.25:
4861.33 H I	0.000	100.0 ± 6.7	100.0 ± 5.9	100 ± 39	100 ± 19
4921.93 He I	-0.015	...	0.55:
4958.91 [O III]	-0.024	67.2 ± 5.0	212 ± 11	81 ± 30	132 ± 19
5006.84 [O III]	-0.036	210 ± 13	648 ± 36	232 ± 63	383 ± 44
5015.68 He I	-0.038	1.02:
5158.81 [Fe II]	-0.073	1.95:
5197.90 [N I]	-0.082	2.76:
5517.71 [Cl III]	-0.154	...	0.33:
5537.88 [Cl III]	-0.158	...	0.26:
5875.64 He I	-0.215	12.8 ± 1.6	9.95 ± 1.70	46.1:	10.5 ± 2.8
6300.30 [O I]	-0.282	7.5 ± 1.1	2.21 ± 0.76	...	7.7 ± 3.1
6312.10 [S III]	-0.283	1.10:	1.16 ± 0.31
6363.78 [O I]	-0.291	2.18:	0.65:
6548.03 [N II]	-0.318	20.1 ± 1.8	2.82 ± 0.71	...	6.0:
6562.82 H I	-0.320	288 ± 19	202 ± 46	284 ± 75	288 ± 35
6583.41 [N II]	-0.323	64.8 ± 4.6	7.76 ± 1.84	23.4:	23.2 ± 6.1
6678.15 He I	-0.336	2.81:	2.55 ± 0.74	...	3.9:
6730.85 [S II]	-0.344	18.0 ± 2.0	5.09 ± 1.32	28.5:	17.6 ± 8.3
Aperture size (arcsec)		6×1	8.4×1	8×1	4.4×1
Distance ^b (arcsec)		0	13	23	12
$F(\text{H}\beta)^a$		23.25 ± 1.08	23.42 ± 0.89	0.52 ± 0.10	1.32 ± 0.12
$C(\text{H}\beta)$		0.11 ± 0.03	0.33 ± 0.03	0.06 ± 0.03	0.37 ± 0.02
W_{abs} (Å)		2.4 ± 0.4	1.3 ± 0.3	0.5	2.2 ± 0.2
$-W(\text{H}\alpha)$ (Å)		75.2 ± 5.0	423.6 ± 22.5	43.9 ± 10.0	48.8 ± 2.7
$-W(\text{H}\beta)$ (Å)		16.4 ± 1.1	75.7 ± 4.2	8.4 ± 3.2	20.8 ± 1.3
$-W(\text{H}\gamma)$ (Å)		5.5 ± 0.4	26.9 ± 1.5	...	7.5 ± 0.9
$-W([\text{O III}])$ 5007 (Å)		29.4 ± 1.8	462.7 ± 23.1	20.2 ± 5.1	77.9 ± 3.9

^a In units of 10^{-15} erg s⁻¹ cm⁻² and not corrected for extinction; ^b relative distance with respect to the center of Haro 15.

Table A.2. Physical conditions and chemical abundances of the ionized gas of the regions analyzed in Haro 15.

Region	C	A	B	D
T_e (O III) (K)	9500 ± 800^a	$12\,900 \pm 700$	$11\,500 \pm 1000^a$	$11\,800 \pm 800^a$
T_e (O II) (K)	9600 ± 600	$12\,000 \pm 500$	$11\,000 \pm 700$	$11\,260 \pm 600$
n_e (cm $^{-3}$)	100	100	100	100
12+log(O $^{+}$ /H $^{+}$)	8.16 ± 0.11	7.35 ± 0.08	8.04 ± 0.14	7.93 ± 0.13
12+log(O $^{++}$ /H $^{+}$)	7.94 ± 0.10	8.01 ± 0.06	7.72 ± 0.13	7.90 ± 0.10
12+log(O/H)	8.37 ± 0.10	8.10 ± 0.06	8.21 ± 0.14	8.22 ± 0.11
log(O $^{++}$ /O $^{+}$)	-0.23 ± 0.16	0.66 ± 0.10	-0.32 ± 0.18	-0.03 ± 0.15
12+log(N $^{+}$ /H $^{+}$)	7.13 ± 0.07	6.00 ± 0.06	6.55 ± 0.19	6.47 ± 0.14
12+log(N/H)	7.34 ± 0.10	6.75 ± 0.10	6.72 ± 0.21	6.76 ± 0.15
log(N/O)	-1.03 ± 0.15	-1.35 ± 0.11	-1.49 ± 0.20	-1.46 ± 0.16
12+log(S $^{+}$ /H $^{+}$)	6.05 ± 0.10	5.26 ± 0.08	6.08 ± 0.22	5.85 ± 0.21
12+log(S $^{++}$ /H $^{+}$)	6.52 ± 0.25	6.02 ± 0.13
12+log(S/H)	6.65 ± 0.20	6.20 ± 0.11
log(S/O)	-1.71 ± 0.18	-1.89 ± 0.15
12+log(Ne $^{++}$ /H $^{+}$)	7.29 ± 0.15	7.33 ± 0.10	...	7.14 ± 0.20
12+log(Ne/H)	7.72 ± 0.15	7.42 ± 0.10	...	7.46 ± 0.20
log(Ne/O)	-0.65 ± 0.18	-0.68 ± 0.12	...	-0.76 ± 0.18
12+log(Ar $^{+3}$ /H $^{+}$)	...	4.92 ± 0.17
12+log(Cl $^{+2}$ /H $^{+}$)	...	4.26 ± 0.28
12+log(Fe $^{++}$ /H $^{+}$)	5.2:	5.5:
12+log(Fe/H)	6.2:	6.5:
log(Fe/O)	-2.2:	-1.6:
12+log(He $^{+}$ /H $^{+}$)	10.97 ± 0.05	10.88 ± 0.06	10.96:	10.96 ± 0.12
[O/H]	-0.29	-0.56 ± 0.11	-0.45	-0.44

^aEstimated using empirical relations; ^b [O/H] = log(O/H)-log(O/H) $_{\odot}$, using 12+log(O/H) $_{\odot}$ = 8.66 ± 0.05 ([Asplund et al. 2005](#)).

Table A.3. Dereddened line intensity ratios with respect to $I(\text{H}\beta)=100$ for knots analyzed in Mkn 1199.

Line	$f(\lambda)$	C	NE	A	B	D
3728.00 [O II]	0.256	124.6 ± 7.8	254 ± 20	204:	145:	192 ± 45
3835.39 H I	0.237	1.23:
3868.75 [Ne III]	0.230	1.39 ± 0.46	6.64:
3889.05 H I	0.226	9.2 ± 1.9	9.40:
3967.46 [Ne III]	0.210	...	6.22:
3970.07 H I	0.210	18.0 ± 1.2
4101.74 H I	0.182	27.0 ± 1.9	26.0 ± 5.9	30.5 ± 7.6
4340.47 H I	0.127	45.9 ± 3.4	46.7 ± 6.2	31:	...	47 ± 18
4471.48 He I	0.095	2.48:	5.46:
4658.10 [Fe III]	0.050	3.44 ± 0.68
4686.00 He II	0.043	0.24:
4861.33 H I	0.000	100.0 ± 6.0	100 ± 11	100:	100:	100 ± 27
4958.91 [O III]	-0.024	10.7 ± 1.4	60.0 ± 8.4	23:	...	$23.5:$
5006.84 [O III]	-0.036	30.6 ± 2.4	167 ± 15	62:	85:	60 ± 20
5055.98 Si II	-0.048	0.81:	2.37:
5197.90 [N I]	-0.082	2.49 ± 0.60
5754.64 [N II]	-0.194	0.61:
5875.64 He I	-0.215	9.46 ± 0.93	12.7 ± 3.1	$11.6:$
6300.30 [O I]	-0.282	3.57 ± 0.80	6.6 ± 2.4	$16.8:$
6312.10 [S III]	-0.283	0.14:	1.19:
6363.78 [O I]	-0.291	0.85:
6548.03 [N II]	-0.318	48.2 ± 3.1	13.9 ± 3.5	51:	51:	57 ± 14
6562.82 H I	-0.320	293 ± 17	290 ± 25	294:	296:	298 ± 65
6583.41 [N II]	-0.323	149.8 ± 8.9	41.2 ± 5.6	142:	141:	172 ± 35
6678.15 He I	-0.336	1.90 ± 0.49	3.88:
6716.47 [S II]	-0.342	35.8 ± 2.3	35.4 ± 5.2	66:	74:	74 ± 19
6730.85 [S II]	-0.344	32.1 ± 6.4	25.5 ± 4.4	40:	44:	49 ± 14
7065.28 He I	-0.387	1.30 ± 0.42
7135.78 [Ar III]	-0.396	1.91 ± 0.56	6.29:
7318.39 [O II]	-0.418	0.87 ± 0.32
7329.66 [O II]	-0.420	0.39:
Aperture size (arcsec)		10×1	6×1	8×1	8×1	5.6×1
Distance ^b (arcsec)		0	26	18	14	8.4
$F(\text{H}\beta)^a$		74.2 ± 3.1	3.17 ± 0.21	0.33 ± 0.08	0.42 ± 0.10	0.98 ± 0.14
$C(\text{H}\beta)$		0.30 ± 0.03	0.16 ± 0.03	0.17 ± 0.04	0.44 ± 0.06	0.27 ± 0.04
W_{abs} (Å)		1.8 ± 0.4	0.6 ± 0.3	1.7 ± 0.3	2	2.5 ± 0.3
$-W(\text{H}\alpha)$ (Å)		129.1 ± 7.9	110 ± 10	21 ± 7	22 ± 8	34.7 ± 7.6
$-W(\text{H}\beta)$ (Å)		21.4 ± 1.3	20.2 ± 2.3	5.0 ± 2.6	5.2 ± 2.4	8.3 ± 2.3
$-W(\text{H}\gamma)$ (Å)		6.7 ± 0.5	8.4 ± 1.1	1.5 ± 1.7	...	2.1 ± 0.8
$-W([\text{O III}])$ 5007 (Å)		6.8 ± 0.5	35.5 ± 3.4	2.8 ± 1.6	4.2 ± 1.8	5.1 ± 1.7

^a In units of 10^{-15} erg s⁻¹ cm⁻² and not corrected for extinction; ^b relative distance with respect to the center of Mkn 1199.

Table A.4. Physical conditions and chemical abundances of the ionized gas of the regions analyzed in Mkn 1199.

Region	Center	NE ^a	A ^a	B ^a	D ^a
T_e (O III) (K)	5400 ± 700	8450 ± 800	6950 ± 800	6300 ± 800	6750 ± 800
T_e (O II) (K)	6800 ± 600^b	8900 ± 600	7850 ± 600	7400 ± 600	7700 ± 600
n_e (cm $^{-3}$)	300 ± 100	100	100	100	100
$12+\log(O^+/H^+)$	8.59 ± 0.11	8.25 ± 0.12	8.43 ± 0.20	8.43 ± 0.21	8.44 ± 0.16
$12+\log(O^{++}/H^+)$	8.24 ± 0.12	8.05 ± 0.11	7.99 ± 0.23	8.32 ± 0.26	8.05 ± 0.19
$12+\log(O/H)$	8.75 ± 0.12	8.46 ± 0.13	8.57 ± 0.21	8.68 ± 0.23	8.59 ± 0.17
$\log(O^{++}/O^+)$	-0.36 ± 0.16	-0.19 ± 0.09	-0.44 ± 0.18	-0.10 ± 0.32	-0.37 ± 0.22
$12+\log(N^+/H^+)$	7.98 ± 0.09	7.05 ± 0.10	7.76 ± 0.14	7.85 ± 0.18	7.86 ± 0.11
$12+\log(N/H)$	8.14 ± 0.11	7.26 ± 0.13	7.90 ± 0.18	8.10 ± 0.28	8.00 ± 0.15
$\log(N/O)$	-0.62 ± 0.10	-1.20 ± 0.11	-0.67 ± 0.20	-0.58 ± 0.30	-0.59 ± 0.17
$12+\log(S^+/H^+)$	6.70 ± 0.09	6.28 ± 0.09	6.67 ± 0.16	6.80 ± 0.16	6.76 ± 0.13
$12+\log(S^{++}/H^+)$	7.05 ± 0.17	6.80 ± 0.22
$12+\log(S/H)$	7.22 ± 0.15	6.92 ± 0.18
$\log(S/O)$	-1.54 ± 0.14	-1.54 ± 0.17
$12+\log(Ne^{++}/H^+)$	7.65 ± 0.17	7.40 ± 0.20
$12+\log(Ne/H)$	8.17 ± 0.19	7.81 ± 0.20
$\log(Ne/O)$	-0.58 ± 0.17	-0.65 ± 0.18
$12+\log(Ar^{+3}/H^+)$	6.07 ± 0.16	5.95 ± 0.22
$12+\log(Fe^{++}/H^+)$	6.75 ± 0.13
$12+\log(Fe/H)$	6.89 ± 0.13
$\log(Fe/O)$	-1.86 ± 0.26
$12+\log(He^+/H^+)$	10.79 ± 0.07	10.9:	10.9:
[O/H] ^b	$+0.09 \pm 0.17$	-0.20	-0.09	+0.02	-0.07

^a Electron temperatures estimated using empirical relations; ^b derived from [N II] and [O II] ratios, see Sect. 3.4.1; ^c [O/H] = $\log(O/H)-\log(O/H)_\odot$, using $12+\log(O/H)_\odot = 8.66 \pm 0.05$ ([Asplund et al. 2005](#)).

Table A.5. Dereddened line intensity ratios with respect to $I(\text{H}\beta)=100$ for knots analyzed in Mkn 5. Region A was observed using three slit positions with a PA of 0° (INT-1), $349^\circ = -11^\circ$ (INT-2), and $354^\circ = -6^\circ$ (WHT).

Line	$f(\lambda)$	A-INT-1	A-INT-2	A-WHT	B
3666.10 H I	0.267	1.99 ± 0.71
3697.15 H I	0.262	1.16:
3705.04 He I	0.260	1.65:
3711.97 H I	0.259	...	2.03 ± 0.76
3728.00 [O II]	0.256	191 ± 12	213 ± 12	...	252:
3750.15 H I	0.253	1.79 ± 0.68
3770.63 H I	0.249	...	2.47 ± 0.79
3797.90 H I	0.244	...	1.54:
3819.61 He I	0.240	...	0.65:
3835.39 H I	0.237	7.4 ± 1.7	5.6 ± 1.3
3868.75 [Ne III]	0.230	23.1 ± 3.3	31.0 ± 2.4
3889.05 H I	0.226	13.6 ± 2.9	17.7 ± 2.1
3967.46 [Ne III]	0.210	18.7 ± 1.9	21.3 ± 1.8
4026.21 He I	0.198	...	1.55:
4068.60 [S II]	0.189	2.24 ± 0.70	2.29 ± 0.76
4101.74 H I	0.182	26.0 ± 2.8	26.8 ± 2.1
4168.97 He I	0.167	...	1.06:
4340.47 H I	0.127	47.0 ± 3.2	47.0 ± 3.1	47.0 ± 2.8	...
4363.21 [O III]	0.121	5.14 ± 0.91	5.29 ± 0.93	4.93 ± 0.74	...
4387.93 He I	0.115	...	0.56:	1.32 ± 0.40	...
4416.27 [Fe II]	0.109	0.38:	...
4471.48 He I	0.095	4.43 ± 0.85	3.96 ± 0.84	4.16 ± 0.60	...
4658.10 [Fe III]	0.050	...	1.10:	0.72:	...
4686.00 He II	0.043	0.92 ± 0.19	1.01:	0.82:	...
4711.37 [Ar IV]	0.037	...	0.59:
4713.14 He I	0.037	0.28:	...
4740.16 [Ar IV]	0.030	0.31:	...
4861.33 H I	0.000	100.0 ± 6.3	100.0 ± 5.7	100.0 ± 5.2	100:
4921.93 He I	-0.015	...	1.70:	0.95 ± 0.36	...
4958.91 [O III]	-0.024	144.1 ± 8.5	144.7 ± 7.8	133.8 ± 7.2	70.43:
4985.90 [Fe III]	-0.031	2.33 ± 0.65	2.02:	2.20:	...
5006.84 [O III]	-0.036	423 ± 22	430 ± 21	374 ± 19	214 ± 69
5015.68 He I	-0.038	2.13 ± 0.62	...
5197.90 [N I]	-0.082	...	0.46:
5875.64 He I	-0.215	8.46 ± 0.83	8.41 ± 0.88	11.0 ± 1.0	...
6300.30 [O I]	-0.282	5.12 ± 0.68	4.57 ± 0.66	4.05 ± 0.58	...
6312.10 [S III]	-0.283	2.31 ± 0.55	1.92 ± 0.43	1.79 ± 0.47	...
6363.78 [O I]	-0.291	1.90 ± 0.51	1.52:	1.19 ± 0.38	...
6548.03 [N II]	-0.318	4.56 ± 0.56	5.25 ± 0.69	5.49 ± 0.63	...
6562.82 H I	-0.320	283 ± 16	284 ± 15	284 ± 14	284 ± 85
6583.41 [N II]	-0.323	14.7 ± 1.2	14.0 ± 1.1	14.9 ± 1.1	10.13:
6678.15 He I	-0.336	3.43 ± 0.63	3.49 ± 0.66	3.05 ± 0.51	...
6716.47 [S II]	-0.342	21.5 ± 1.5	22.2 ± 1.7	24.3 ± 1.5	67.4:
6730.85 [S II]	-0.344	15.6 ± 1.2	16.0 ± 1.4	18.1 ± 1.2	51.6:
7065.28 He I	-0.387	2.13 ± 0.50	2.40 ± 0.64	2.17 ± 0.45	...
7135.78 [Ar III]	-0.396	8.49 ± 0.61	8.56 ± 0.97	7.70 ± 0.52	...
7281.35 He I	-0.414	0.41:	...
7318.39 [O II]	-0.418	...	2.87:	3.62 ± 0.54	...
7329.66 [O II]	-0.420	...	2.57:	2.74 ± 0.44	...
7751.10 [Ar III]	-0.467	1.64 ± 0.38	...
Aperture size (arcsec)		14.4×1	16×1	3.6×1	6×1
Distance ^b (arcsec)		0	0	0	16
$F(\text{H}\beta)^a$		17.66 ± 0.73	18.13 ± 0.69	10.83 ± 0.40	0.35 ± 0.08
$C(\text{H}\beta)$		0.36 ± 0.02	0.17 ± 0.02	0.03 ± 0.02	0.30 ± 0.06
W_{abs} (Å)		1.1 ± 0.2	0.8 ± 0.2	0	1.5 ± 0.5
$-W(\text{H}\alpha)$ (Å)		449 ± 26	435 ± 23	678 ± 35	43 ± 12
$-W(\text{H}\beta)$ (Å)		75 ± 5	80 ± 5	135 ± 7	10:
$-W(\text{H}\gamma)$ (Å)		43 ± 3	34 ± 2	44 ± 3	...
$-W([\text{O III}])$ 5007 (Å)		320 ± 17	360 ± 18	530 ± 28	33 ± 11

^a In units of 10^{-15} erg s⁻¹ cm⁻² and not corrected for extinction; ^b relative distance with respect to the center of Mkn 5.

Table A.6. Physical conditions and chemical abundances of the ionized gas of the regions analyzed in Mkn 5.

Region	A-INT-1	A-INT-2	A-WHT	B ^a
T_e (O III) (K)	$12\,400 \pm 700$	$12\,450 \pm 650$	$12\,700 \pm 600$	$13\,250 \pm 900$
T_e (O II) (K)	$11\,700 \pm 500$	$11\,700 \pm 450$	$11\,900 \pm 400$	$12\,300 \pm 700$
n_e (cm ⁻³)	≤ 100	≤ 100	≤ 100	≤ 110
$12+\log(O^+/H^+)$	7.62 ± 0.09	7.67 ± 0.08	7.71 ± 0.11	7.66 ± 0.19
$12+\log(O^{++}/H^+)$	7.88 ± 0.06	7.87 ± 0.06	7.80 ± 0.06	7.49 ± 0.13
$12+\log(O/H)$	8.07 ± 0.07	8.08 ± 0.07	8.06 ± 0.08	7.89 ± 0.17
$\log(O^{++}/O^+)$	0.25 ± 0.10	0.21 ± 0.09	0.09 ± 0.11	-0.17 ± 0.18
$12+\log(N^+/H^+)$	6.27 ± 0.06	6.29 ± 0.05	6.30 ± 0.05	6.08 ± 0.22
$12+\log(N/H)$	6.72 ± 0.09	6.71 ± 0.08	6.65 ± 0.08	6.30 ± 0.22
$\log(N/O)$	-1.35 ± 0.10	-1.38 ± 0.10	-1.41 ± 0.10	-1.58 ± 0.20
$12+\log(S^+/H^+)$	5.78 ± 0.04	5.79 ± 0.04	5.82 ± 0.04	6.24 ± 0.11
$12+\log(S^{++}/H^+)$	6.37 ± 0.13	6.28 ± 0.13	6.23 ± 0.12	...
$12+\log(S/H)$	6.51 ± 0.12	6.44 ± 0.12	6.40 ± 0.12	...
$\log(S/O)$	-1.56 ± 0.13	-1.64 ± 0.12	-1.67 ± 0.13	...
$12+\log(Ne^{++}/H^+)$	7.02 ± 0.12	7.14 ± 0.10
$12+\log(Ne/H)$	7.22 ± 0.12	7.35 ± 0.11
$\log(Ne/O)$	-0.85 ± 0.14	-0.74 ± 0.13
$12+\log(Ar^{++}/H^+)$	5.69 ± 0.07	5.69 ± 0.09	5.60 ± 0.09	...
$12+\log(Ar^{+3}/H^+)$...	4.69 ± 0.25	4.54 ± 0.21	...
$12+\log(Ar/H)$...	5.79 ± 0.12	5.73 ± 0.10	...
$\log(Ar/O)$...	-2.29 ± 0.15	-2.33 ± 0.12	...
$12+\log(Fe^{++}/H^+)$	5.73 ± 0.13	$5.66:$	$5.68:$...
$12+\log(Fe/H)$	6.11 ± 0.16	$6.00:$	$5.98:$...
$\log(Fe/O)$	-1.96 ± 0.18	$-2.08:$	$-2.08:$...
$12+\log(He^+/H^+)$	10.96 ± 0.06	10.91 ± 0.06	10.92 ± 0.05	...
[O/H] ^b	-0.59 ± 0.12	-0.58 ± 0.12	-0.60 ± 0.13	-0.77

^a Electron temperatures estimated using empirical relations; ^b[O/H] = log(O/H)–log(O/H)_⊙, using $12+\log(O/H)_\odot = 8.66 \pm 0.05$ ([Asplund et al. 2005](#)).

Table A.7. Dereddened line intensity ratios with respect to $I(\text{H}\beta) = 100$ for regions analyzed in IRAS 08208+2816. The slit positions that we used for each knot are: PA 345° for C, PA 355° for #8 and #10, and PA 10° for #3 y #5.

Line	$f(\lambda)$	C	#3	#5	#8	#10
3728.00 [O II]	0.256	146.8 ± 9.8	279 ± 20	251 ± 24	164 ± 22	324 ± 64
3750.15 H I	0.253	1.74 ± 0.51
3770.63 H I	0.249	1.55 ± 0.49
3797.90 H I	0.244	2.86 ± 0.60	3.17:
3835.39 H I	0.237	5.53 ± 0.79
3868.75 [Ne III]	0.230	32.8 ± 2.2	15.1 ± 3.4	26.3 ± 7.0	5.27:	...
3889.05 H I	0.226	15.1 ± 1.7	13.5 ± 3.2	12.9 ± 5.0	6.36:	...
3967.46 [NeIII]H7	0.210	22.1 ± 1.9	15.9 ± 2.9	17.0 ± 5.3	22.0 ± 5.7	26.23:
4026.21 He I	0.198	0.92:
4068.60 [S II]	0.189	1.14 ± 0.45
4101.74 H I	0.182	26.1 ± 2.1	26.1 ± 2.9	24.1 ± 5.1	26.1 ± 5.7	26.23:
4340.47 H I	0.127	46.7 ± 2.7	46.8 ± 4.6	43.8 ± 6.8	43.5 ± 7.4	46 ± 15
4363.21 [O III]	0.121	3.12 ± 0.48	1.66:	2.26:
4471.48 He I	0.095	4.00 ± 0.67	3.7 ± 1.3
4658.10 [Fe III]	0.050	1.68 ± 0.58	1.72:
4861.33 H I	0.000	100.0 ± 5.7	100.0 ± 8.4	100 ± 11	100 ± 12	100 ± 22
4958.91 [O III]	-0.024	152.6 ± 8.3	76.6 ± 5.8	104 ± 10	44.7 ± 8.9	54 ± 15
5006.84 [O III]	-0.036	470 ± 24	228 ± 14	305 ± 24	89 ± 13	151 ± 30
5197.90 [N I]	-0.082	1.09 ± 0.42	...	2.46:
5875.64 He I	-0.215	12.8 ± 1.2	12.4 ± 1.9	14.6 ± 2.9	12.3 ± 3.4	11.28:
6300.30 [O I]	-0.282	4.74 ± 0.62	5.6 ± 1.1	9.8 ± 2.3	10.1 ± 3.1	9.00:
6312.10 [S III]	-0.283	1.46 ± 0.42	1.13:
6363.78 [O I]	-0.291	1.70 ± 0.46	...	3.21:	2.24:	...
6548.03 [N II]	-0.318	14.2 ± 1.1	16.0 ± 2.4	16.2 ± 3.9	30.2 ± 5.3	14.95:
6562.82 H I	-0.320	285 ± 15	283 ± 20	281 ± 25	288 ± 33	286 ± 51
6583.41 [N II]	-0.323	36.9 ± 2.6	39.2 ± 4.2	37.8 ± 5.3	75.3 ± 9.3	42 ± 11
6678.15 He I	-0.336	3.26 ± 0.63	3.04 ± 0.93	...	2.93:	3.65:
6716.47 [S II]	-0.342	22.0 ± 1.5	40.2 ± 4.2	52.9 ± 6.8	66.4 ± 9.6	50 ± 13
6730.85 [S II]	-0.344	16.6 ± 1.3	28.5 ± 3.3	34.5 ± 5.2	46.7 ± 7.5	36 ± 10
7065.28 He I	-0.387	2.42 ± 0.57
7135.78 [Ar III]	-0.396	6.37 ± 0.78	11.8 ± 3.0
Aperture size (arcsec)		1.4 × 1	2.8 × 1	4.0 × 1	6.4 × 1	4.0 × 1
Distance (arcsec) ^b		—	12.6	6.8	8.8	16
$F(\text{H}\beta)^a$		12.9 ± 0.5	5.97 ± 0.28	2.98 ± 0.19	4.05 ± 0.34	1.36 ± 0.18
$C(\text{H}\beta)$		0.11 ± 0.02	0.47 ± 0.04	0.41 ± 0.04	0.17 ± 0.03	0.12 ± 0.02
W_{abs} (Å)		3.2 ± 0.1	1.6 ± 0.2	1.4 ± 0.2	4.9 ± 0.1	1.9 ± 0.1
$-W(\text{H}\alpha)$ (Å)		331 ± 18	202 ± 15	346 ± 32	89 ± 10	98 ± 18
$-W(\text{H}\beta)$ (Å)		80 ± 5	56 ± 5	62 ± 7	24 ± 3	17 ± 4
$-W(\text{H}\gamma)$ (Å)		30 ± 2	20 ± 2	27 ± 4	10 ± 2	9 ± 3
$-W([\text{O III}])$ (Å)		370 ± 19	130 ± 8	200 ± 16	18 ± 3	19 ± 4

^a In units of 10^{-15} erg s⁻¹ cm⁻² and not corrected for extinction; ^b relative distance with respect to the center of IRAS 08208+2816.

Table A.8. Physical conditions and chemical abundances of the ionized gas of the regions analyzed in IRAS 08208+2816.

Region	<i>C</i>	#3 ^a	#5 ^a	#8 ^a	#10 ^a
T_e (O III) (K)	$10\,100 \pm 700$	9400 ± 900	9600 ± 1000	6750 ± 1000	9500 ± 1000
T_e (O II) (K)	$10\,100 \pm 500$	9600 ± 700	9700 ± 800	7700 ± 800	9650 ± 800
n_e (cm $^{-3}$)	<100	<100	<100	<100	<100
$12+\log(O^+/H^+)$	7.77 ± 0.09	8.15 ± 0.13	8.08 ± 0.15	8.39 ± 0.15	8.20 ± 0.18
$12+\log(O^{++}/H^+)$	8.20 ± 0.07	8.01 ± 0.11	8.10 ± 0.12	8.28 ± 0.14	7.82 ± 0.17
$12+\log(O/H)^c$	8.33 ± 0.08	8.24:	8.27:
$12+\log(O/H)^d$	8.41 ± 0.10	8.39 ± 0.11	8.39 ± 0.13	8.64 ± 0.15	8.35 ± 0.17
$\log(O^{++}/O^+)$	0.43 ± 0.12	0.15 ± 0.17	0.02 ± 0.19	-0.10 ± 0.20	-0.38 ± 0.22
$12+\log(N^+/H^+)$	6.88 ± 0.05	6.98 ± 0.08	6.96 ± 0.10	7.54 ± 0.10	6.97 ± 0.14
$12+\log(N/H)$	7.44 ± 0.10	7.22 ± 0.11	7.27 ± 0.13	7.80 ± 0.16	7.12 ± 0.17
$\log(N/O)$	-0.89 ± 0.11	-1.17 ± 0.13	-1.12 ± 0.14	-0.84 ± 0.15	-1.22 ± 0.18
$12+\log(S^+/H^+)$	5.94 ± 0.05	6.25 ± 0.08	6.33 ± 0.09	6.73 ± 0.12	6.34 ± 0.13
$12+\log(S^{++}/H^+)$	6.52 ± 0.16	6.56 ± 0.28
$12+\log(S/H)$	6.69 ± 0.13	6.75 ± 0.23
$\log(S/O)$	-1.64 ± 0.16	-1.64 ± 0.25
$12+\log(Ne^{++}/H^+)$	7.52 ± 0.11	7.37 ± 0.19	7.53 ± 0.22	7.60 ± 0.25	...
$12+\log(Ne/H)$	7.66 ± 0.11	7.75 ± 0.18	7.82 ± 0.22	7.96 ± 0.25	...
$\log(Ne/O)$	-0.67 ± 0.13	-0.64 ± 0.21	-0.57 ± 0.25	-0.68 ± 0.26	...
$12+\log(Ar^{+2}/H^+)$	5.78 ± 0.08	6.11 ± 0.15
$12+\log(Ar/H)$	5.86 ± 0.11	5.92 ± 0.15
$\log(Ar/O)$	-2.51 ± 0.15	-2.47 ± 0.18
$12+\log(Fe^{++}/H^+)$	5.90 ± 0.15
$12+\log(Fe/H)$	6.47 ± 0.15
$\log(Fe/O)$	-1.95 ± 0.17
$12+\log(He^+/H^+)$	10.97 ± 0.04	10.95 ± 0.07	11.03 ± 0.09	10.90 ± 0.12	10.94:
[O/H] ^b	-0.33 ± 0.13	-0.27	-0.27	-0.02	-0.31

^a Electron temperatures estimated using empirical relations; ^b [O/H] = log(O/H)-log(O/H)₀, using $12+\log(O/H)_0 = 8.66 \pm 0.05$ ([Asplund et al. 2005](#)); ^c oxygen abundance computed using the direct method; ^d oxygen abundance computed using the empirical calibrations given by [Pilyugin \(2001a,b\)](#).

Table A.9. Dereddened line intensity ratios with respect to $I(\text{H}\beta)=100$ for regions analyzed in POX 4, UM 420, and SBS 0926+606.

Line	$f(\lambda)$	POX 4	POX 4 Comp	UM 420	SBS 0926+606A	SBS 0926+606B
3679.36 H I	0.265	0.30 ± 0.07
3682.81 H I	0.264	0.40 ± 0.08
3686.83 H I	0.263	0.74 ± 0.10
3691.56 H I	0.263	0.92 ± 0.11
3697.15 H I	0.262	1.08 ± 0.12	...	0.53:
3703.86 H I	0.260	2.02 ± 0.17	...	0.93 ± 0.36
3711.97 H I	0.259	1.86 ± 0.16	...	1.14 ± 0.38
3721.83 [S III]	0.257	3.68 ± 0.24	...	1.30 ± 0.39
3726.03 [O II]	0.257	42.8 ± 2.0	142 ± 35	85.9 ± 4.7
3728.82 [O II]	0.256	57.1 ± 2.7	165 ± 40	140.2 ± 7.5
3734.17 H I	0.255	2.58 ± 0.19	...	2.19 ± 0.45
3750.15 H I	0.253	2.88 ± 0.21	...	2.32 ± 0.46
3770.63 H I	0.249	3.77 ± 0.25	...	2.41 ± 0.47
3797.90 H I	0.244	5.30 ± 0.37	...	3.36 ± 0.75
3819.61 He I	0.240	0.91 ± 0.11	...	0.87:
3835.39 H I	0.237	7.18 ± 0.40	...	5.96 ± 0.70
3868.75 [Ne III]	0.230	51.7 ± 2.3	35.6:	29.7 ± 2.0
3889.05 H I	0.226	17.75 ± 0.95	...	16.8 ± 1.5
3967.46 [Ne III]	0.210	16.17 ± 0.78	...	6.45 ± 0.72
3970.07 H I	0.210	15.36 ± 0.71	...	16.1 ± 1.2
4009.22 He I	0.202	0.15 ± 0.06
4026.21 He I	0.198	1.57 ± 0.14	...	1.55 ± 0.40
4068.60 [S II]	0.189	0.92 ± 0.11	...	2.40 ± 0.46
4076.35 [S II]	0.187	0.28 ± 0.07	...	0.71:
4101.74 H I	0.182	26.0 ± 1.2	...	26.1 ± 2.1
4143.76 He I	0.172	0.13:
4168.97 He I	0.167	0.77 ± 0.25	...
4276.83 [Fe II]	0.142	0.08:
4287.40 [Fe II]	0.139	0.11:	...	0.42:
4340.47 H I	0.127	51.2 ± 2.3	49 ± 16	47.0 ± 3.0	47.5 ± 2.8	47.4 ± 9.1
4363.21 [O III]	0.121	11.89 ± 0.61	...	4.48 ± 0.82	7.00 ± 0.66	...
4387.93 He I	0.115	0.42 ± 0.08	...	0.21:
4413.78 [Fe III]	0.109	0.07:
4471.48 He I	0.095	4.12 ± 0.26	...	3.07 ± 0.50	3.69 ± 0.41	...
4562.60 Mg I	0.073	0.19 ± 0.06	0.44:	...
4571.20 Mg I	0.071	0.13:
4658.10 [Fe III]	0.050	0.64 ± 0.09	...	1.31 ± 0.46	1.20 ± 0.40	...
4686.00 He II	0.043	1.21 ± 0.16	...	1.04 ± 0.28	0.72 ± 0.21	...
4701.53 [Fe III]	0.039	0.14:
4711.37 [Ar IV]	0.037	1.86 ± 0.15	0.49:	...
4713.14 He I	0.037	0.45:	0.72 ± 0.24	...
4740.16 [Ar IV]	0.030	1.34 ± 0.12	0.49:	...
4754.83 [Fe III]	0.026	0.29:	...
4861.33 H I	0.000	100.0 ± 4.3	100 ± 19	100.0 ± 5.5	100.0 ± 4.9	100 ± 14
4881.00 [Fe III]	-0.005	0.15 ± 0.06	0.29:	...
4921.93 He I	-0.015	0.49 ± 0.10	...	0.22:	0.38:	...
4958.91 [O III]	-0.024	237 ± 10	93 ± 19	106.8 ± 6.0	157.8 ± 7.7	134 ± 18
4985.90 [Fe III]	-0.031	0.57 ± 0.09	...	0.57:
5006.84 [O III]	-0.036	731 ± 32	255 ± 55	312 ± 17
5015.68 He I	-0.038	2.57 ± 0.21
5041.03 Si II	-0.044	0.14:
5047.74 He I	-0.046	0.16 ± 0.06
5197.90 [N I]	-0.082	0.23 ± 0.06
5200.26 [N I]	-0.083	0.30 ± 0.07
5270.40 [Fe III]	-0.100	0.48:
5517.71 [C III]	-0.154	0.31 ± 0.07	...	0.25:
5537.88 [Cl III]	-0.158	0.23 ± 0.08	...	0.26:
5754.64 [N II]	-0.194	0.08:	...	0.59:
5875.64 He I	-0.215	10.93 ± 0.56	...	10.51 ± 0.79	10.77 ± 0.85	12.4 ± 4.0
6300.30 [O I]	-0.282	1.81 ± 0.12	...	7.49 ± 0.49	3.13 ± 0.30	5.32:
6312.10 [S III]	-0.283	1.60 ± 0.12	...	1.75 ± 0.18	1.98 ± 0.24	...
6363.78 [O I]	-0.291	0.61 ± 0.09	...	2.06 ± 0.41	0.92 ± 0.23	2.24:
6371.36 Si II	-0.292	0.05:
6548.03 [N II]	-0.318	1.58 ± 0.11	...	9.14 ± 0.71	2.47 ± 0.30	4.51:
6562.82 H I	-0.320	285 ± 12	282 ± 50	281 ± 14	286 ± 15	286 ± 34
6583.41 [N II]	-0.323	4.20 ± 0.23	11.7:	28.4 ± 1.7	7.50 ± 0.64	18.2 ± 4.6
6678.15 He I	-0.336	2.93 ± 0.20	2.72 ± 0.34	2.63:
6716.47 [S II]	-0.342	7.80 ± 0.38	15.9:	...	16.8 ± 1.0	42.8 ± 7.0
6730.85 [S II]	-0.344	6.03 ± 0.30	10.2:	...	12.12 ± 0.77	29.5 ± 5.6
7065.28 He I	-0.387	2.45 ± 0.32	...
7135.78 [Ar III]	-0.396	6.54 ± 0.45	5.09:
7281.35 He I	-0.414	0.61 ± 0.20	...
7318.39 [O II]	-0.418	2.11 ± 0.23	2.22:
7329.66 [O II]	-0.420	1.71 ± 0.22	2.05:
7751.10 [Ar III]	-0.467	1.75 ± 0.25	...
Aperture size ('')		7.2 × 1	3.6 × 1	3.6 × 1	4.0 × 1	5.6 × 1
Distance ('') ^a	-	20.4	-	-	74.4	
$F(\text{H}\beta)^b$	56.0 ± 1.8	0.11 ± 0.02	6.88 ± 0.27	16.20 ± 0.58	1.58 ± 0.15	
$C(\text{H}\beta)$	0.08 ± 0.01	0.06 ± 0.03	0.09 ± 0.01	0.12 ± 0.03	0.18 ± 0.04	
W_{abs} (Å)	2.0 ± 0.1	1.4 ± 0.2	2.0 ± 0.1	0.7 ± 0.1	1.0 ± 0.3	
$-W(\text{H}\alpha)$ (Å)	1075 ± 48	380 ± 65	1076 ± 55	613 ± 33	92 ± 11	
$-W(\text{H}\beta)$ (Å)	200 ± 9	12 ± 4	169 ± 10	125 ± 6	18 ± 3	
$-W(\text{H}\gamma)$ (Å)	71 ± 3	4 ± 1	69 ± 4	41 ± 2	9 ± 2	
$-W(\text{[O III] } 5007)$ (Å)	1366 ± 60	19 ± 3	581 ± 32	

^a Relative distance of the knot with respect to the main region in the galaxy; ^b in units of $10^{-15} \text{ erg s}^{-1} \text{ cm}^{-2}$ and not corrected for extinction.

Table A.10. Physical conditions and chemical abundances of the ionized gas in POX 4, UM 420, and SBS 0926+606.

Object	POX 4	POX 4 Comp ^a	UM 420	SBS 0926+606A	SBS 0926+606B ^a
T_e (O III) (K)	$14\,000 \pm 500$	$12\,400 \pm 1\,000$	$13\,200 \pm 600$	$13\,600 \pm 700$	$11\,500 \pm 1\,000$
T_e (O II) (K)	$12\,800 \pm 400$	$11\,800 \pm 600$	$12\,200 \pm 500$	$12\,500 \pm 500$	$11\,000 \pm 800$
n_e (cm $^{-3}$)	250 ± 80	<100	140 ± 80	<100	<100
$12+\log(O^+/H^+)$	7.21 ± 0.04	7.85 ± 0.14	7.63 ± 0.05	7.38 ± 0.10	7.73 ± 0.16
$12+\log(O^{++}/H^+)$	7.96 ± 0.04	7.55 ± 0.11	7.67 ± 0.05	7.80 ± 0.08	7.04 ± 0.15
$12+\log(O/H)$	8.03 ± 0.04^c	8.03 ± 0.13	7.95 ± 0.05^c	7.94 ± 0.08^c	8.15 ± 0.16
$\log(O^{++}/O^+)$	0.74 ± 0.06	-0.30 ± 0.22	0.00 ± 0.08	0.42 ± 0.12	0.21 ± 0.14
$12+\log(N^+/H^+)$	5.68 ± 0.04	6.25 ± 0.18	6.52 ± 0.05	5.93 ± 0.05	6.39 ± 0.09
$12+\log(N/H)$	6.50 ± 0.06	6.43 ± 0.22	6.84 ± 0.06	6.48 ± 0.10	6.80 ± 0.13
$\log(N/O)$	-1.54 ± 0.06	-1.60 ± 0.20	-1.11 ± 0.07	-1.45 ± 0.09	-1.35 ± 0.12
$12+\log(S^+/H^+)$	5.28 ± 0.03	5.62 ± 0.20	5.61 ± 0.11	5.61 ± 0.04	6.12 ± 0.11
$12+\log(S^{++}/H^+)$	6.03 ± 0.08	...	6.16 ± 0.09	6.17 ± 0.11	...
$12+\log(S/H)$	6.24 ± 0.07	...	6.29 ± 0.10	6.34 ± 0.10	...
$\log(S/O)$	-1.80 ± 0.10	...	-1.66 ± 0.13	-1.60 ± 0.13	...
$12+\log(Ne^{++}/H^+)$	7.18 ± 0.06	6.97:	6.96 ± 0.09
$12+\log(Ne/H)$	7.26 ± 0.06	7.40:	7.24 ± 0.09
$\log(Ne/O)$	-0.78 ± 0.10	-0.60:	-0.71 ± 0.13
$12+\log(Ar^{+2}/H^+)$	5.52 ± 0.07	5.54 ± 0.15
$12+\log(Ar^{+3}/H^+)$	5.03 ± 0.07	4.61 ± 0.18	...
$12+\log(Ar/H)$	5.60 ± 0.11	...
$\log(Ar/O)$	-2.34 ± 0.13	...
$12+\log(Cl^{++}/H^+)$	3.83 ± 0.14	...	4.18 ± 0.26
$12+\log(Fe^{++}/H^+)$	5.14 ± 0.10	...	5.52 ± 0.12	5.47 ± 0.14	...
$12+\log(Fe/H)$	5.86 ± 0.10	...	5.79 ± 0.13	5.95 ± 0.15	...
$\log(Fe/O)$	-2.17 ± 0.11	...	-2.16 ± 0.13	-1.99 ± 0.16	...
$12+\log(He^+/H^+)$	10.91 ± 0.03	...	10.88 ± 0.04	10.94 ± 0.04	11.0:
[O/H] ^b	-0.63 ± 0.09	-0.63	-0.71 ± 0.10	-0.72 ± 0.13	-0.51

^a Electron temperatures estimated using empirical relations; ^b [O/H] = log(O/H)-log(O/H)_⊙, using $12+\log(O/H)_\odot = 8.66 \pm 0.05$ ([Asplund et al. 2005](#)); ^c considering the existence of O⁺³ because of the detection of He II $\lambda 4686$, this value should be ~ 0.01 – 0.02 dex higher.

Table A.11. Dereddened line intensity ratios with respect to $I(\text{H}\beta) = 100$ for regions analyzed in SBS 0948+532, SBS 1054+365, and SBS 1211+540.

Line	$f(\lambda)$	SBS 0948+532	SBS 1054+365	SBS 1054+365 b	SBS 1211+540
3697.15 H I	0.262	0.48:
3703.86 H I	0.260	1.96 ± 0.38
3711.97 H I	0.259	1.25 ± 0.32
3721.83 [S III]	0.257	1.57 ± 0.35
3726.03 [O II]	0.257	45.4 ± 2.7	33.0 ± 3.8
3728.00 [O II]	0.256	...	100.2 ± 7.5	350 ± 95	...
3728.82 [O II]	0.256	65.7 ± 3.8	44.8 ± 4.6
3734.17 H I	0.255	2.52 ± 0.43	$2.61:$
3750.15 H I	0.253	2.56 ± 0.43	3.7 ± 1.3
3770.63 H I	0.249	2.88 ± 0.45	$1.53:$...	3.2 ± 1.2
3797.90 H I	0.244	5.11 ± 0.71	$2.85:$...	$3.99:$
3819.61 He I	0.240	0.65 ± 0.25
3835.39 H I	0.237	7.74 ± 0.77	6.8 ± 1.3	...	5.9 ± 1.5
3868.75 [Ne III]	0.230	41.6 ± 2.6	49.6 ± 4.8	...	37.6 ± 4.0
3889.05 H I	0.226	19.7 ± 1.5	19.8 ± 2.8	...	19.9 ± 3.0
3967.46 [Ne III]	0.210	15.0 ± 1.2	27.4 ± 2.8	...	13.3 ± 2.1
3970.07 H I	0.210	16.2 ± 1.2	16.1 ± 2.2
4026.21 He I	0.198	1.45 ± 0.32
4068.60 [S II]	0.189	1.53 ± 0.33	$2.05:$
4101.74 H I	0.182	26.2 ± 1.7	26.4 ± 3.0	...	26.2 ± 3.0
4340.47 H I	0.127	47.2 ± 2.9	47.2 ± 4.1	$28.51:$	47.3 ± 4.1
4363.21 [O III]	0.121	8.13 ± 0.82	9.7 ± 1.5	...	12.2 ± 1.8
4471.48 He I	0.095	3.81 ± 0.49	3.31 ± 0.81	...	4.6 ± 1.3
4658.10 [Fe III]	0.050	$1.13:$
4686.00 He II	0.043	1.3 ± 0.3	0.61 ± 0.23
4711.37 [Ar IV]	0.037	0.85 ± 0.25	$1.18:$
4713.14 He I	0.037	$0.75:$
4733.93 [Fe III]	0.031	$0.18:$
4740.16 [Ar IV]	0.030	0.61 ± 0.24	$0.98:$
4754.83 [Fe III]	0.026	$0.34:$
4861.33 H I	0.000	100.0 ± 5.2	100.0 ± 7.4	100 ± 39	100.0 ± 7.5
4958.91 [O III]	-0.024	189.5 ± 9.2	210 ± 13	75 ± 23	163 ± 10
4985.90 [Fe III]	-0.031	1.49 ± 0.30
5006.84 [O III]	-0.036	584 ± 28	623 ± 37	183 ± 53	481 ± 29
5015.68 He I	-0.038	$2.24:$
5197.90 [N I]	-0.082	...	$1.03:$
5517.71 [Cl III]	-0.154	$0.39:$
5537.88 [Cl III]	-0.158	$0.24:$
5875.64 He I	-0.215	10.76 ± 0.81	8.7 ± 1.6
6300.30 [O I]	-0.282	3.00 ± 0.31	$1.12:$...	$2.36:$
6312.10 [S III]	-0.283	1.74 ± 0.24	$1.36:$...	2.8 ± 1.1
6363.78 [O I]	-0.291	1.07 ± 0.23	$0.65:$...	$0.57:$
6548.03 [N II]	-0.318	2.45 ± 0.30	2.02 ± 0.74	$7.66:$	$0.82:$
6562.82 H I	-0.320	278 ± 14	277 ± 17	279 ± 74	280 ± 17
6583.41 [N II]	-0.323	6.21 ± 0.60	5.6 ± 1.0	$20.2:$	2.24 ± 0.89
6678.15 He I	-0.336	2.81 ± 0.36	2.94 ± 0.96	$7.40:$	3.6 ± 1.1
6716.47 [S II]	-0.342	...	10.1 ± 1.2	$22.4:$	5.65 ± 0.88
6730.85 [S II]	-0.344	...	7.03 ± 0.97	$19.6:$	4.91 ± 0.82
7065.28 He I	-0.387	...	2.08 ± 0.83
7135.78 [Ar III]	-0.396	...	8.8 ± 1.5
Aperture size (arcsec)		3.6	6.4	5.8	3.6
Distance ^a (arcsec)		0	0	17.8	0
$F(\text{H}\beta)^b$		8.44 ± 0.32	14.57 ± 0.68	0.66 ± 0.13	1.84 ± 0.09
$C(\text{H}\beta)$		0.35 ± 0.03	0.02 ± 0.02	0.6 ± 0.1	0.12 ± 0.01
W_{abs} (Å)		0.3 ± 0.1	0.8 ± 0.1	0.3 ± 0.1	1.3 ± 0.1
$-W(\text{H}\alpha)$ (Å)		788 ± 43	422 ± 27	32 ± 8	705 ± 45
$-W(\text{H}\beta)$ (Å)		213 ± 11	89 ± 7	8 ± 3	135 ± 10
$-W(\text{H}\gamma)$ (Å)		57 ± 4	43 ± 4	2 ± 1	74 ± 7
$-W(\text{[O III]})$ 5007 (Å)		689 ± 34	567 ± 35	12 ± 3	618 ± 38

^a Relative distance of the knot with respect to the main region in the galaxy; ^b in units of 10^{-15} erg s⁻¹ cm⁻² and not corrected for extinction.

Table A.12. Physical conditions and chemical abundances of the ionized gas in SBS 0948+532, SBS 1054+365, and SBS 1211+540.

Object	SBS 0948+532	SBS 1054+365	SBS 1054+365 ^a	SBS 1211+540
T_e (O III) (K)	$13\,100 \pm 600$	$13\,700 \pm 900$	$11\,800 \pm 1100$	$17\,100 \pm 600$
T_e (O II) (K)	$12\,200 \pm 400$	$12\,600 \pm 700$	$11\,300 \pm 900$	$15\,000 \pm 400$
N_e (cm $^{-3}$)	250 ± 80	<100	300 ± 200	320 ± 50
$12+\log(O^+/H^+)$	7.33 ± 0.05	7.22 ± 0.10	7.97 ± 0.18	6.88 ± 0.05
$12+\log(O^{++}/H^+)$	7.94 ± 0.05	7.92 ± 0.07	7.62 ± 0.12	7.57 ± 0.04
$12+\log(O/H)$	8.03 ± 0.05	8.00 ± 0.07	8.13 ± 0.16	7.65 ± 0.04
$\log(O^{++}/O^+)$	0.61 ± 0.08	0.70 ± 0.11	-0.35 ± 0.20	0.69 ± 0.07
$12+\log(N^+/H^+)$	5.91 ± 0.05	5.81 ± 0.08	6.49 ± 0.20	5.26 ± 0.12
$12+\log(N/H)$	6.61 ± 0.07	6.59 ± 0.09	6.65 ± 0.21	6.03 ± 0.13
$\log(N/O)$	-1.42 ± 0.08	-1.41 ± 0.08	-1.47 ± 0.20	-1.62 ± 0.10
$12+\log(S^+/H^+)$	5.43 ± 0.12	5.37 ± 0.07	5.89 ± 0.16	5.04 ± 0.06
$12+\log(S^{++}/H^+)$	6.16 ± 0.11	5.99 ± 0.22	...	6.02 ± 0.14
$12+\log(S/H)$	6.34 ± 0.11	6.21 ± 0.18	...	6.18 ± 0.12
$\log(S/O)$	-1.69 ± 0.14	-1.79 ± 0.15	...	-1.47 ± 0.14
$12+\log(Ne^{++}/H^+)$	7.21 ± 0.09	7.25 ± 0.09	...	6.82 ± 0.08
$12+\log(Ne/H)$	7.30 ± 0.09	7.33 ± 0.12	...	6.90 ± 0.08
$\log(Ne/O)$	-0.73 ± 0.12	-0.67 ± 0.11	...	-0.75 ± 0.10
$12+\log(Ar^{+2}/H^+)$...	5.62 ± 0.10
$12+\log(Ar^{+3}/H^+)$	4.79 ± 0.15	4.90 ± 0.20	...	4.77 ± 0.22
$12+\log(Ar/H)$...	5.71 ± 0.17
$\log(Ar/O)$...	-2.29 ± 0.14
$12+\log(Cl^{++}/H^+)$	3.97 ± 0.18
$12+\log(Fe^{++}/H^+)$	5.64 ± 0.09
$12+\log(Fe/H)$	6.25 ± 0.09
$\log(Fe/O)$	-1.78 ± 0.10
$12+\log(He^+/H^+)$	10.88 ± 0.04	10.88 ± 0.07	11.30:	10.90 ± 0.15
[O/H] ^b	-0.63 ± 0.10	-0.66 ± 0.12	-0.53	-1.01 ± 0.09

^a Electron temperatures estimated using empirical relations; ^b [O/H]=log(O/H)-log(O/H)_○, using $12+\log(O/H)_\odot = 8.66 \pm 0.05$ ([Asplund et al. 2005](#)).

Table A.13. Dereddened line intensity ratios with respect to $I(\text{H}\beta) = 100$ for knots analyzed in SBS 1319+579 (regions A, B, and C) and SBS 1415+437 (regions C and A).

Line	$f(\lambda)$	SBS 1319+579			SBS 1415+437	
		A	B	C	C	A
4340.47 H I	0.127	47.2 ± 2.6	47.4 ± 4.6	47.4 ± 3.1	47.5 ± 2.8	47.4 ± 3.8
4363.21 [O III]	0.121	9.98 ± 0.62	4.2 ± 1.0	3.73 ± 0.64	7.11 ± 0.61	6.1 ± 1.2
4387.93 He I	0.115	0.43 ± 0.17	...	1.12:
4437.55 He I	0.104	0.20:
4471.48 He I	0.095	3.85 ± 0.36	4.4 ± 1.6	3.88 ± 0.68	3.86 ± 0.49	2.80 ± 0.66
4658.10 [Fe III]	0.050	0.72:	1.05 ± 0.32	0.99:
4686.00 He II	0.043	0.8:	2.35 ± 0.23	...
4711.37 [Ar IV]	0.037	2.14 ± 0.35
4713.14 He I	0.037	0.30:	...
4740.16 [Ar IV]	0.030	1.61 ± 0.26	0.56:	...
4861.33 H I	0.000	100.0 ± 4.9	100.0 ± 8.5	100.0 ± 6.2	100.0 ± 4.9	100.0 ± 6.3
4881.00 [Fe III]	-0.005	0.21:	...
4921.93 He I	-0.015	0.96 ± 0.23	...	0.75:	1.41 ± 0.33	...
4958.91 [O III]	-0.024	232 ± 12	132 ± 10	129.9 ± 7.4	107.5 ± 5.5	107.3 ± 6.5
4985.90 [Fe III]	-0.031	1.35 ± 0.33	1.19:
5006.84 [O III]	-0.036	301 ± 14	286 ± 16
5015.68 He I	-0.038	1.52 ± 0.34	...
5875.64 He I	-0.215	11.90 ± 0.86	11.7 ± 3.2	11.2 ± 1.2	9.61 ± 0.92	7.7 ± 1.1
6300.30 [O I]	-0.282	1.74 ± 0.26	3.08:	4.77 ± 0.72	3.44 ± 0.43	2.41 ± 0.56
6312.10 [S III]	-0.283	1.56 ± 0.29	1.14:	1.80 ± 0.52	1.34 ± 0.31	0.98:
6363.78 [O I]	-0.291	0.60 ± 0.18	1.28:	1.48 ± 0.52	0.96 ± 0.31	0.86:
6548.03 [N II]	-0.318	1.44 ± 0.27	3.8 ± 1.5	5.50 ± 0.72	1.13 ± 0.35	1.07:
6562.82 H I	-0.320	280 ± 13	279 ± 19	281 ± 15	274 ± 13	278 ± 17
6583.41 [N II]	-0.323	4.08 ± 0.42	13.1 ± 2.4	14.8 ± 1.3	4.30 ± 0.45	3.49 ± 0.98
6678.15 He I	-0.336	2.97 ± 0.34	2.7 ± 1.1	2.87 ± 0.66	2.31 ± 0.41	2.28 ± 0.66
6716.47 [S II]	-0.342	7.79 ± 0.56	26.0 ± 3.2	27.9 ± 1.9	13.15 ± 0.83	9.2 ± 1.1
6730.85 [S II]	-0.344	5.76 ± 0.44	17.8 ± 2.9	18.9 ± 1.3	9.60 ± 0.63	6.71 ± 0.94
7065.28 He I	-0.387	2.69 ± 0.36	...	2.09 ± 0.54	1.49 ± 0.34	2.09 ± 0.66
7135.78 [Ar III]	-0.396	4.76 ± 0.47	6.6 ± 1.6	6.06 ± 0.72	3.77 ± 0.38	3.28 ± 0.61
7281.35 He I	-0.414	0.62:
7318.39 [O II]	-0.418	1.30 ± 0.23	3.1 ± 1.0	2.69 ± 0.33	2.05 ± 0.33	1.56 ± 0.62
7329.66 [O II]	-0.420	1.17 ± 0.24	2.01:	1.94 ± 0.27	1.73 ± 0.35	1.35:
7751.10 [Ar III]	-0.467	1.55 ± 0.25	0.96 ± 0.31	0.94:
Aperture size (arcsec)		6×1	2.8×1	5.6×1	6×1	3.4×1
Distance (arcsec) ^a	-		10	29	-	6
$F(\text{H}\beta)^b$		14.57 ± 0.53	1.97 ± 0.10	8.18 ± 0.32	18.51 ± 0.66	4.07 ± 0.17
$C(\text{H}\beta)$		0.03 ± 0.01	0.11 ± 0.03	0.02 ± 0.02	0.01 ± 0.02	0.16 ± 0.03
W_{abs} (Å)		0.0 ± 0.1	0.4 ± 0.1	0.2 ± 0.1	0.8 ± 0.1	1.0 ± 0.2
$-W(\text{H}\alpha)$ (Å)		1530 ± 75	162 ± 11	295 ± 23	1300 ± 65	1187 ± 75
$-W(\text{H}\beta)$ (Å)		285 ± 14	42 ± 4	94 ± 6	222 ± 11	130 ± 8
$-W(\text{H}\gamma)$ (Å)		84 ± 5	15 ± 1	23 ± 1	73 ± 4	58 ± 5
$-W([\text{O III}])$ 5007 (Å)		542 ± 26	574 ± 32

^a Relative distance of the knot with respect to the main region in the galaxy; ^b in units of 10^{-15} erg s⁻¹ cm⁻² and not corrected for extinction.

Table A.14. Physical conditions and chemical abundances of the ionized gas for the regions analyzed in SBS 1319+579 and SBS 1415+437.

Object	SBS 1319+579A	SBS 1319+579B	SBS 1319+ 579C	SBS 1415+ 437C	SBS 1415+ 437A
T_e (O III) (K)	$13\,400 \pm 500$	$11\,900 \pm 800$	$11\,500 \pm 600$	$16\,400 \pm 600$	$15\,500 \pm 700$
T_e (O II) (K)	$12\,400 \pm 400$	$11\,300 \pm 600$	$11\,050 \pm 400$	$14\,500 \pm 400$	$13\,850 \pm 500$
N_e (cm $^{-3}$)	<100	<100	<100	<100	<100
$12+\log(O^+/H^+)$	7.22 ± 0.07	7.73 ± 0.12	7.75 ± 0.07	7.07 ± 0.07	7.05 ± 0.10
$12+\log(O^{++}/H^+)$	7.98 ± 0.06	7.89 ± 0.10	7.93 ± 0.08	7.42 ± 0.04	7.47 ± 0.05
$12+\log(O/H)$	8.05 ± 0.06	8.12 ± 0.10	8.15 ± 0.07	7.58 ± 0.05^b	7.61 ± 0.06
$\log(O^{++}/O^+)$	0.77 ± 0.12	0.16 ± 0.19	0.18 ± 0.13	0.35 ± 0.08	0.42 ± 0.14
$12+\log(N^+/H^+)$	5.69 ± 0.05	6.24 ± 0.08	6.37 ± 0.05	5.50 ± 0.05	5.48 ± 0.10
$12+\log(N/H)$	6.52 ± 0.09	6.63 ± 0.12	6.77 ± 0.07	6.01 ± 0.07	6.04 ± 0.11
$\log(N/O)$	-1.53 ± 0.10	-1.49 ± 0.12	-1.38 ± 0.10	-1.57 ± 0.08	-1.57 ± 0.09
$12+\log(S^+/H^+)$	5.29 ± 0.03	5.88 ± 0.05	5.93 ± 0.04	5.38 ± 0.03	5.26 ± 0.05
$12+\log(S^{++}/H^+)$	6.09 ± 0.12	6.13 ± 0.18	6.39 ± 0.15	5.75 ± 0.11	5.68 ± 0.15
$12+\log(S/H)$	6.29 ± 0.11	6.36 ± 0.15	6.55 ± 0.12	5.96 ± 0.08	5.89 ± 0.13
$\log(S/O)$	-1.76 ± 0.10	-1.76 ± 0.14	-1.60 ± 0.11	-1.62 ± 0.12	-1.72 ± 0.14
$12+\log(Ar^{+2}/H^+)$	5.44 ± 0.07	5.61 ± 0.12	5.61 ± 0.09	5.13 ± 0.10	5.14 ± 0.14
$12+\log(Ar^{+3}/H^+)$	5.19 ± 0.09	4.56 ± 0.16	...
$12+\log(Ar/H)$	5.65 ± 0.08	5.27 ± 0.12	...
$\log(Ar/O)$	-2.41 ± 0.11	-2.31 ± 0.13	...
$12+\log(Fe^{++}/H^+)$	$5.46:$	5.23 ± 0.12	$5.24:$
$12+\log(Fe/H)$	$5.80:$	5.67 ± 0.12	$5.72:$
$\log(Fe/O)$	$-2.35:$	-1.91 ± 0.13	$-1.89:$
$12+\log(He^+/H^+)$	10.94 ± 0.04	10.94 ± 0.11	10.92 ± 0.05	10.75 ± 0.06	10.77 ± 0.07
[O/H] ^a	-0.61 ± 0.11	-0.54 ± 0.15	-0.51 ± 0.13	-1.08 ± 0.10	-1.05 ± 0.12

^a [O/H] = log(O/H)-log(O/H)_○, using $12+\log(O/H)_\odot = 8.66 \pm 0.05$ (Asplund et al. 2005); ^b considering the existence of O⁺³ because of the detection of He II $\lambda 4686$, this value should be ~ 0.01 – 0.02 dex higher.

Table A.15. Dereddened line intensity ratios with respect to $I(\text{H}\beta) = 100$ for knots analyzed in III Zw 107 (regions A, B, and C) and Tol 9 (spectra obtained with 2.5 m INT and 2.56 m NOT).

Line	$f(\lambda)$	III Zw 107 A	III Zw 107 B	III Zw 107 C	Tol 9 INT	Tol 9 NOT
3554.42 He I	0.283	3.8 ± 1.4	...
3728.00 [O II]	0.256	213 ± 12	306 ± 23	20.32:	142 ± 10	177 ± 27
3770.63 H I	0.249	1.00:	0.54:	...	0.56:	...
3797.90 H I	0.244	2.37:	0.83:	...
3835.39 H I	0.237	3.60 ± 0.95	1.69:	5.02:	1.94:	...
3868.75 [Ne III]	0.230	23.3 ± 2.1	21.1 ± 4.0	20.64:	10.9 ± 2.0	12.08:
3889.05 H I	0.226	12.6 ± 1.7	11.1 ± 4.2	8.84:	6.9 ± 2.1	...
3967.46 [NeIII]H7	0.210	17.1 ± 1.7	22.4 ± 2.9	...	21.6 ± 1.9	...
4068.60 [S II]	0.189	2.26 ± 0.82	4.69:	...	3.3 ± 1.1	...
4101.74 H I	0.182	26.2 ± 1.8	26.1 ± 4.2	27.5 ± 6.5	25.3 ± 2.5	26.3 ± 4.0
4340.47 H I	0.127	46.7 ± 2.8	46.9 ± 4.8	47.5 ± 7.9	45.8 ± 3.2	46.9 ± 5.8
4363.21 [O III]	0.121	3.14 ± 0.67	1.97:	...	0.55:	...
4471.48 He I	0.095	4.08 ± 0.75	3.40:	...	3.94 ± 0.65	3.96:
4658.10 [Fe III]	0.050	1.06:	1.09:	...
4686.00 He II	0.043	0.33:	...
4814.55 [Fe II]	0.012	0.85:	...
4861.33 H I	0.000	100.0 ± 5.3	100.0 ± 8.2	100 ± 15	100.0 ± 6.0	100 ± 10
4921.93 He I	-0.015	0.42:
4958.91 [O III]	-0.024	123.7 ± 6.5	99.5 ± 8.1	93 ± 14	78.3 ± 5.2	75.5 ± 9.1
5006.84 [O III]	-0.036	375 ± 18	293 ± 19	257 ± 32	236 ± 13	225 ± 21
5197.90 [N I]	-0.082	1.08:	2.07:
5200.26 [N I]	-0.083	0.36:	2.63 ± 0.78	...
5517.71 [Cl III]	-0.154	0.22:	0.57:	...
5537.88 [Cl III]	-0.158	0.20:	0.64:	...
5754.64 [N II]	-0.198	0.41:	...
5875.64 He I	-0.215	12.5 ± 1.1	13.1 ± 2.3	12.94:	12.6 ± 1.4	16.3 ± 3.8
6300.30 [O I]	-0.282	4.56 ± 0.61	6.1 ± 2.0	7.57:	7.78 ± 0.71	7.32 ± 0.96
6312.10 [S III]	-0.283	1.02 ± 0.23	0.66:	0.66:
6363.78 [O I]	-0.291	1.55 ± 0.42	2.01:	3.58:	2.14 ± 0.59	2.30 ± 0.91
6548.03 [N II]	-0.318	9.98 ± 0.75	12.1 ± 1.4	13.6 ± 4.5	23.8 ± 1.8	24.3 ± 2.3
6562.82 H I	-0.320	282 ± 16	273 ± 18	280 ± 35	267 ± 18	284 ± 30
6583.41 [N II]	-0.323	28.7 ± 1.8	37.0 ± 3.2	41.4 ± 8.3	72.2 ± 4.9	82.1 ± 7.3
6678.15 He I	-0.336	3.17 ± 0.50	4.01:	...	3.16 ± 0.64	4.1 ± 1.3
6716.47 [S II]	-0.342	19.6 ± 1.3	36.4 ± 4.3	52.2 ± 8.7	37.0 ± 2.6	42.1 ± 3.9
6730.85 [S II]	-0.344	15.9 ± 1.1	27.5 ± 3.6	35.6 ± 6.9	29.8 ± 2.2	35.7 ± 3.4
7065.28 He I	-0.387	2.27 ± 0.40	1.93 ± 0.51	2.41 ± 0.94
7135.78 [Ar III]	-0.396	11.4 ± 0.9	9.4 ± 1.7	...	10.5 ± 1.0	10.8 ± 1.5
7318.39 [O II]	-0.418	2.12 ± 0.58	1.96:	1.57 ± 0.43
7329.66 [O II]	-0.420	2.48 ± 0.66	1.08:	1.30 ± 0.34
7751.10 [Ar III]	-0.467	2.68 ± 0.68
Aperture size (arcsec)		7.2×1	5.6×1	5.2×1	6.4×1	3.8×1
Distance (arcsec) ^a		—	7.2	12.4	—	—
$F(\text{H}\beta)^b$		22.3 ± 0.8	8.6 ± 0.4	1.56 ± 0.14	23.4 ± 0.9	3.8×0.3
$C(\text{H}\beta)$		0.68 ± 0.04	0.15 ± 0.02	0.22 ± 0.03	0.50 ± 0.05	0.40 ± 0.05
W_{abs} (Å)		2.0 ± 0.3	1.30 ± 0.10	0.50 ± 0.10	7.5 ± 0.8	6.2 ± 0.6
$-W(\text{H}\alpha)$ (Å)		306 ± 18	76 ± 5	30 ± 4	178 ± 12	186 ± 15
$-W(\text{H}\beta)$ (Å)		44 ± 3	15 ± 2	4.7 ± 0.7	33 ± 2	17 ± 3
$-W(\text{H}\gamma)$ (Å)		16.4 ± 1.0	5.5 ± 0.6	1.8 ± 0.3	12.3 ± 0.8	
$-W([\text{O III}]) 5007$ (Å)		172 ± 8	41 ± 3	11.6 ± 1.5	77 ± 4	32 ± 4

^a Relative distance of the knot with respect to the main region in the galaxy; ^b in units of 10^{-15} erg s⁻¹ cm⁻² and not corrected for extinction.

Table A.16. Physical conditions and chemical abundances of the ionized gas for the regions analyzed in III Zw 107 and Tol 9.

Object	III Zw 107 A	III Zw 107 B ^a	III Zw 107 C ^a	Tol 9 INT	Tol 9 NOT
T_e (O III) (K)	10900 ± 900	10400 ± 1000	10350 ± 1000	7600 ± 1000	7850 ± 1000
T_e (O II) (K)	10500 ± 800	10300 ± 800	10250 ± 800	8300 ± 700	8500 ± 800
N_e (cm $^{-3}$)	200 ± 60	<100	<100	180 ± 60	260 ± 80
$12+\log(O^+/H^+)$	7.87 ± 0.11	8.05 ± 0.14	8.08 ± 0.15	8.15 ± 0.18	8.21 ± 0.19
$12+\log(O^{++}/H^+)$	7.99 ± 0.08	7.96 ± 0.10	7.92 ± 0.11	8.38 ± 0.14	8.29 ± 0.14
$12+\log(O/H)$	8.23 ± 0.09	8.31 ± 0.12	8.31 ± 0.13	8.58 ± 0.15	8.55 ± 0.16
$\log(O^{++}/O^+)$	0.12 ± 0.14	-0.09 ± 0.18	-0.15 ± 0.21	0.22 ± 0.18	0.09 ± 0.20
$12+\log(N^+/H^+)$	6.70 ± 0.06	6.82 ± 0.08	6.88 ± 0.11	7.37 ± 0.08	7.37 ± 0.09
$12+\log(N/H)$	7.07 ± 0.08	7.08 ± 0.10	7.11 ± 0.12	7.80 ± 0.14	7.72 ± 0.14
$\log(N/O)$	-1.16 ± 0.10	-1.23 ± 0.15	-1.20 ± 0.16	-0.78 ± 0.15	-0.84 ± 0.17
$12+\log(S^+/H^+)$	5.87 ± 0.06	6.14 ± 0.08	6.28 ± 0.09	6.41 ± 0.08	6.46 ± 0.08
$12+\log(S^{++}/H^+)$	6.23 ± 0.16	6.78 ± 0.24	6.70 ± 0.25
$12+\log(S/H)$	6.42 ± 0.13	6.97 ± 0.20	6.92 ± 0.21
$\log(S/O)$	-1.82 ± 0.15	-1.61 ± 0.17	-1.63 ± 0.18
$12+\log(Ne^{++}/H^+)$	7.26 ± 0.13	7.30 ± 0.16	7.30 ± 0.19	7.64 ± 0.18	7.60 ± 0.23
$12+\log(Ne/H)$	7.51 ± 0.13	7.65 ± 0.16	7.68 ± 0.20	7.84 ± 0.18	7.86 ± 0.23
$\log(Ne/O)$	-0.73 ± 0.15	-0.66 ± 0.20	-0.62 ± 0.20	-0.74 ± 0.18	-0.69 ± 0.22
$12+\log(Ar^{+2}/H^+)$	5.94 ± 0.08	5.87 ± 0.14	...	6.30 ± 0.13	6.28 ± 0.15
$12+\log(Ar/H)$	5.77 ± 0.09	5.69 ± 0.14	...	6.13 ± 0.13	6.12 ± 0.15
$\log(Ar/O)$	-2.46 ± 0.13	-2.52 ± 0.18	...	-2.45 ± 0.20	-2.44 ± 0.22
$12+\log(Cl^{++}/H^+)$	4.32:	5.31:	...
$12+\log(Fe^{++}/H^+)$	5.61:	6.14:	...
$12+\log(Fe/H)$	5.92:	6.51:	...
$\log(Fe/O)$	-2.31:	-2.07:	...
$12+\log(He^+/H^+)$	10.94 ± 0.05	10.99 ± 0.08	10.99:	10.93 ± 0.06	11.04 ± 0.12
[O/H] ^b	-0.43 ± 0.14	-0.35	-0.35	-0.08 ± 0.20	-0.11 ± 0.21

^a Electron temperatures estimated using empirical relations; ^b [O/H] = $\log(O/H) - \log(O/H)_\odot$, using $12+\log(O/H)_\odot = 8.66 \pm 0.05$ ([Asplund et al. 2005](#)).

Table A.17. Dereddened line intensity ratios with respect to $I(\text{H}\beta) = 100$ for knots analyzed in Tol 1457-262 (regions A, B, and C) and Arp 252 (galaxy A, ESO 566-8, and galaxy B, ESO 566-7).

Line	$f(\lambda)$	Tol 1457-262A	Tol 1457-262B	Tol 1457-262C	ESO 566-8	ESO 566-7
3728.00 [O II]	0.256	224 ± 17	187 ± 16	270 ± 25	256 ± 18	280 ± 51
3797.90 H I	0.244	4.46 ± 0.81
3835.39 H I	0.237	4.29 ± 0.79	11.8 ± 2.1	...	6.0 ± 1.3	...
3868.75 [Ne III]	0.230	30.4 ± 8.9	27.1 ± 9.1	23 ± 11	4.77:	...
3889.05 H I	0.226	12.0 ± 3.0	27.3 ± 5.6	23.1 ± 5.5	10.2 ± 2.9	...
3967.46 [NeIII]H7	0.210	21.9 ± 1.8	25.3 ± 3.5	23.3 ± 4.5	14.8 ± 2.1	...
4068.60 [S II]	0.189	1.38:	...
4101.74 H I	0.182	26.0 ± 2.3	31.0 ± 4.6	27.0 ± 5.0	25.9 ± 3.0	...
4243.97 [Fe II]	0.149	1.12:	...
4340.47 H I	0.127	46.7 ± 2.8	50.8 ± 5.6	48.7 ± 6.7	46.7 ± 4.2	46 ± 10
4363.21 [O III]	0.121	8.68 ± 0.77	10.6 ± 3.1	6.8 ± 2.3
4471.48 He I	0.095	4.10 ± 0.66	4.3 ± 1.0	4.9 ± 1.5	5.0 ± 1.4	...
4658.10 [Fe III]	0.050	0.85:	1.12 ± 0.43	...	1.09:	...
4686.00 He II	0.043	1.9 ± 0.4	2.9 ± 0.3	...	0.74 ± 0.25	...
4711.37 [Ar IV]	0.037	1.25:	...
4861.33 H I	0.000	100.0 ± 5.5	100.0 ± 9.0	100 ± 10	100.0 ± 7.1	100 ± 16
4958.91 [O III]	-0.024	203 ± 10	190 ± 12	163 ± 11	56.9 ± 4.3	25.9 ± 5.4
5006.84 [O III]	-0.036	560 ± 27	522 ± 29	455 ± 28	204 ± 12	75 ± 11
5041.03 Si II	-0.044	0.48:	...
5055.98 Si II	-0.048	0.33:	...
5197.90 [N I]	-0.082	2.96 ± 0.79	...
5270.40 [Fe III]	-0.100	0.50:	...
5754.64 [N II]	-0.194	1.23 ± 0.32	...
5875.64 He I	-0.215	12.6 ± 2.8	11.3 ± 2.5	13.4 ± 2.4	14.8 ± 4.4	16.25:
6300.30 [O I]	-0.282	2.88 ± 0.33	2.23 ± 0.61	4.0 ± 1.1	4.45 ± 0.54	4.42:
6312.10 [S III]	-0.283	1.34 ± 0.24	1.76 ± 0.56	...	0.23:	...
6363.78 [O I]	-0.291	0.95 ± 0.23	0.96:	1.00:	1.64 ± 0.32	3.15:
6548.03 [N II]	-0.318	3.13 ± 0.35	2.00 ± 0.61	3.8 ± 1.3	42.4 ± 3.2	40.3 ± 7.2
6562.82 H I	-0.320	285 ± 15	286 ± 17	279 ± 18	286 ± 17	287 ± 35
6583.41 [N II]	-0.323	9.32 ± 0.70	5.7 ± 1.2	10.4 ± 2.2	118.3 ± 7.7	121 ± 15
6678.15 He I	-0.336	3.51 ± 0.42	3.26 ± 0.94	3.6 ± 1.3	5.03 ± 0.90	...
6716.47 [S II]	-0.342	17.1 ± 1.0	17.6 ± 2.3	26.3 ± 3.3	36.7 ± 2.7	89 ± 12
6730.85 [S II]	-0.344	13.81 ± 0.87	13.3 ± 1.9	21.2 ± 2.7	32.0 ± 2.4	66 ± 10
7065.28 He I	-0.387	3.61 ± 0.47	3.1 ± 1.1	3.12:	3.47 ± 0.82	...
7135.78 [Ar III]	-0.396	12.39 ± 0.86	11.6 ± 1.7	12.0 ± 2.5	7.7 ± 1.6	14.9:
7155.14 [Fe II]	-0.399	0.38:
7281.35 He I	-0.414	0.83 ± 0.21
7318.39 [O II]	-0.418	3.79 ± 0.32	3.46 ± 0.75	4.7 ± 1.3	2.98 ± 0.67	...
7329.66 [O II]	-0.420	3.02 ± 0.26	2.98 ± 0.70	3.4 ± 1.3	2.25 ± 0.60	...
7751.10 [Ar III]	-0.467	2.64 ± 0.33	2.80:	...	1.93 ± 0.52	...
Aperture size (arcsec)		3.8×1	1.5×1	2.25×1	3.2×1	3.0×1
Distance (arcsec) ^a		—	9.7	5.5	—	49.7
$F(\text{H}\beta)^b$		222 ± 8	47.7 ± 2.3	33.6 ± 1.7	111 ± 5	10.2 ± 0.8
$C(\text{H}\beta)$		0.57 ± 0.03	0.00 ± 0.05	0.15 ± 0.02	0.49 ± 0.03	0.23 ± 0.05
W_{abs} (Å)		1.4 ± 0.2	0.0 ± 0.1	0.7 ± 0.1	1.3 ± 0.1	2.7 ± 0.2
$-W(\text{H}\alpha)$ (Å)		603 ± 32	390 ± 28	342 ± 23	472 ± 29	79 ± 10
$-W(\text{H}\beta)$ (Å)		101 ± 6	82 ± 7	92 ± 9	95 ± 7	13 ± 2
$-W(\text{H}\gamma)$ (Å)		31 ± 2	24 ± 3	30 ± 4	38 ± 3	4 ± 2
$-W([\text{O III}])$ 5007 (Å)		560 ± 27	430 ± 25	411 ± 26	197 ± 12	10 ± 3

^a Relative distance of the knot with respect to the main region in the galaxy; ^b in units of 10^{-15} erg s⁻¹ cm⁻² and not corrected for extinction.

Table A.18. Physical conditions and chemical abundances of the ionized gas for the regions analyzed in Tol 1457-262 and Arp 252 (galaxy A, ESO 566-8, and galaxy B, ESO 566-7).

Object	Tol 1457-262A	Tol 1457-262B	Tol 1457-262C	ESO 566-8	ESO 566-7 ^a
T_e (O III) (K)	$14\,000 \pm 700$	$15\,200 \pm 900$	$13\,400 \pm 1100$	8700 ± 900	7900 ± 1000
T_e (O II) (K)	$12\,500 \pm 600$	$14\,200 \pm 700$	$12\,400 \pm 1000$	9100 ± 800	8500 ± 900
N_e (cm ⁻³)	200 ± 80	<100	200 ± 100	300 ± 100	100 ± 150
$12+\log(O^+/H^+)$	7.59 ± 0.10	7.32 ± 0.10	7.69 ± 0.15	8.23 ± 0.13	8.39 ± 0.18
$12+\log(O^{++}/H^+)$	7.87 ± 0.05	7.74 ± 0.06	7.82 ± 0.09	8.04 ± 0.10	7.82 ± 0.15
$12+\log(O/H)$	8.05 ± 0.07^c	7.88 ± 0.07	8.06 ± 0.11	8.46 ± 0.11^c	8.50 ± 0.16
$\log(O^{++}/O^+)$	0.27 ± 0.11	0.43 ± 0.11	0.14 ± 0.16	-0.19 ± 0.17	-0.57 ± 0.22
$12+\log(N^+/H^+)$	6.02 ± 0.06	5.70 ± 0.09	6.10 ± 0.10	7.49 ± 0.06	7.57 ± 0.10
$12+\log(N/H)$	6.48 ± 0.09	6.27 ± 0.12	6.47 ± 0.15	7.71 ± 0.08	7.67 ± 0.11
$\log(N/O)$	-1.57 ± 0.11	-1.61 ± 0.12	-1.59 ± 0.16	-0.76 ± 0.12	-0.82 ± 0.16
$12+\log(S^+/H^+)$	5.65 ± 0.05	5.53 ± 0.06	5.84 ± 0.09	6.32 ± 0.07	6.74 ± 0.12
$12+\log(S^{++}/H^+)$	5.95 ± 0.14	5.95 ± 0.16
$12+\log(S/H)$	6.18 ± 0.10	6.16 ± 0.15
$\log(S/O)$	-1.88 ± 0.13	-1.72 ± 0.18
$12+\log(Ne^{++}/H^+)$	6.99 ± 0.15	6.87 ± 0.18	6.98 ± 0.20	7.48 ± 0.16	...
$12+\log(Ne/H)$	7.17 ± 0.15	7.00 ± 0.18	7.22 ± 0.20	7.90 ± 0.16	...
$\log(Ne/O)$	-0.88 ± 0.18	-0.88 ± 0.20	-0.84 ± 0.22	-0.56 ± 0.19	...
$12+\log(Ar^{+2}/H^+)$	5.73 ± 0.08	5.66 ± 0.14	5.77 ± 0.17	6.01 ± 0.14	6.41 ± 0.18
$12+\log(Ar^{+3}/H^+)$	5.48 ± 0.20	...
$12+\log(Ar/H)$	5.55 ± 0.08	5.44 ± 0.14	5.61 ± 0.17	6.30 ± 0.17	6.00 ± 0.20
$\log(Ar/O)$	-2.50 ± 0.13	-2.44 ± 0.18	-2.45 ± 0.20	-2.17 ± 0.19	-2.49 ± 0.25
$12+\log(Fe^{++}/H^+)$	5.43:	5.62 ± 0.19	...	5.80:	...
$12+\log(Fe/H)$	5.81:	5.98 ± 0.19	...	6.00:	...
$\log(Fe/O)$	-2.24:	-1.90 ± 0.22	...	-2.46:	...
$12+\log(He^+/H^+)$	10.99 ± 0.06	10.95 ± 0.10	10.99 ± 0.08	11.09 ± 0.07	11.06:
[O/H] ^b	-0.61 ± 0.12	-0.78 ± 0.12	-0.60 ± 0.16	-0.20 ± 0.16	-0.16

^a Electron temperatures estimated using empirical relations; ^b [O/H]=log(O/H)-log(O/H)_○, using $12+\log(O/H)_\odot = 8.66 \pm 0.05$ ([Asplund et al. 2005](#)); ^c considering the existence of O⁺³ because of the detection of He II $\lambda 4686$, this value should be ~ 0.01 dex higher.